Measuring cosmic structure. Minkowski valuations and mark correlations for cosmological morphometry

Claus Beisbart

München 2000

Measuring cosmic structure. Minkowski valuations and mark correlations for cosmological morphometry

Claus Beisbart

Dissertation an der Fakultät für Physik
der Ludwig–Maximilians–Universität München
vorgelegt von Claus Beisbart aus Bayreuth
München, den 10.11.2000

Betreuung und Erstgutachten
Priv.-Doz. Dr. T. Buchert

Zweitgutachten
Prof. Dr. R. Bender

Tag der mündlichen Prüfung : 12.2.2001

In bunten Bildern wenig Klarheit,
Viel Irrtum und ein Fünkchen Wahrheit,
So wird der beste Trank gebraut,
Der alle Welt erquickt und auferbaut.

Johann Wolfgang von Goethe, Faust I, Lustige Person im Vorspiel auf dem Theater.

Die Vernunft muß mit ihren Prinzipien...in der einen Hand und mit dem Experiment...in der anderen, an die Natur gehen, zwar um von ihr belehrt zu werden, aber nicht in der Qualität eines Schülers, der sich alles vorsagen läßt, was der Lehrer will, sondern eines bestallten Richters, der die Zeugen nötigt, auf die Fragen zu antworten, die er ihnen vorlegt.

Immanuel Kant, Kritik der reinen Vernunft.

Können wir das Universum wirklich "kennen" ? Mein Gott, es ist doch schwierig genug, sich in Chinatown zurechtzufinden. Der springende Punkt ist doch : Gibt es da draußen irgend etwas ? Und warum ?

Woody Allen, Wie du dir, so ich mir.

Zusammenfassung

In der heutigen Kosmologie werden Inhomogenitäten und Unregelmäßigkeiten in den relevanten Datensätzen wie etwa die Substruktur in Galaxienhaufen und die Tatsache, daß verschiedene Galaxientypen unterschiedlich im Raum verteilt sind, nicht mehr nur als zufällige Fluktuationen interpretiert, sondern für ein Verständnis der kosmischen Materieverteilung positiv nutzbar gemacht. Die vorliegende Arbeit entwickelt in diesem Sinne Maße, welche eine quantitative Beschreibung von solchen Inhomogenitäten liefern, wendet sie sowohl auf Realdaten als auch auf numerische Simulationen an und stellt den Zusammenhang zu physikalischen Modellen her.

Die Integralgeometrie stellt Maße zur Verfügung, die sich unter geometrischen Transformationen und Mengenoperationen in einfacher Weise verhalten. Während bislang in der Kosmologie vor allem die skalaren Minkowski–Funktionale angewandt wurden, um die kosmische Materieverteilung zu charakterisieren, stehen im ersten Teil dieser Arbeit höherrangige Minkowski–Valuationen wie die Quermaßvektoren und –tensoren im Vordergrund. Diese spiegeln die Lage, Symmetrie, Gestalt und Konnektivität von Mustern wider.
Zunächst werden diese Maße für physikalische Anwendungsbereiche erschlossen. Die Anwendungen gelten dann Galaxienhaufen ("Clustern"), deren innere Eigenschaften auch dazu geeignet sind, die Werte der kosmologischen Parameter einzuschränken. Mit Hilfe der Minkowski–Valuationen definieren wir eine Reihe von Strukturfunktionen, die sich speziell dazu eignen, Galaxienhaufen morphologisch zu charakterisieren. Eine Analyse von Clustern, die kosmologischen Dunkle–Materie–Simulationen entstammen (dem sogenannten GIF–Projekt der "German–Israelic Foundation"), zeigt, daß der morphologische Zustand von Galaxienhaufen zwischen verschiedenen kosmologischen Hintergrundmodellen unterscheiden kann. Eine weitere Analyse gilt komplexeren Simulationen, die auch das heiße Cluster–Röntgengas berücksichtigen. Dabei vergleichen wir nicht nur die Gas– und die Dunkle–Materie–Morphologie, sondern untersuchen auch den Zusammenhang mit der inneren Dynamik. In geeigneten Räumen von globalen Clusterparametern entstehen fundamentale Abhängigkeiten wie etwa die Fundamentalebenenrelation. Dabei können wir zeigen, daß der Abstand von der Fundamentalebene, der die Entfernung von einem Gleichgewichtszustand angibt, mit der Substruktur der Galaxienhaufen positiv korreliert ist; mithin spiegelt die Substruktur den inneren dynamischen Zustand eines Clusters. Weiterhin wird gezeigt, daß die Morphologie von Galaxienhaufen auch im Optischen (d.h. in der Verteilung der Clustergalaxien) die Hintergrundkosmologie widerspiegelt. Dazu analysieren wir die Verteilung von Cluster–Galaxien, welche semianalytischen Modelle für die GIF–Simulationen vorhersagen, und Realdaten.

Eine Grundfrage der modernen Kosmologie gilt der Art und Weise, wie die Dunkle

Materie hinter dem Vordergrund der sichtbaren Galaxien im Universum verteilt ist ("Bias"–Problem). Wegen der Schwierigkeiten, die Dunkle Materie zu lokalisieren, sind dabei schon Unterschiede von Interesse, die sich etwa in der räumlichen Verteilung unterschiedlicher Galaxientypen finden. Der zweite Teil der Arbeit beschäftigt sich mit einem neuen Ansatz, solche Unterschiede zu quantifizieren. Dabei versteht man die Galaxienverteilung als Realisation eines markierten Punktprozesses, der neben den Positionen im Raum auch innere Eigenschaften der Galaxien wie Leuchtkräfte oder morphologische Typen erzeugt. Diese Beschreibung ermöglicht es, eine Reihe von Größen einzuführen, mit denen man testen kann, ob eine Markensegregation vorliegt, das heißt, ob das räumliche Clustern der Galaxien von deren inneren Eigenschaften abhängt. Solche Testgrößen – wir beziehen uns dabei hauptsächlich auf Statistik zweiter Ordnung – zeigen, angewandt auf den Southern Sky Redshift Survey II, signifikante Leuchtkraft– und Morphologie–Segregation an. Ein Vergleich mit Modellen zeigt die komplexe Natur dieser Leuchtkraft–Segregation, die insbesondere nicht auf die Morphologie–Dichte–Relation zurückzuführen ist.

Bemerkung: Im Vergleich zu der von der Fakultät für Physik akzeptierten Version meiner Dissertation enthält diese Version ein paar wenige kleine Änderungen, die jedoch in keiner Weise die Methoden und die Hauptergebnisse der Arbeit betreffen.

Remark: This version of my thesis contains a few slight changes with respect to the version accepted by the faculty of physics, which, however, do not refer to the methods and main results of my thesis.

Contents

Part I

The hierarchy of Minkowski valuations and the morphology of cosmic structure

Chapter 1

The hierarchy of Minkowski valuations

The shape of a thing frequently is its first property to be recognized. In astrophysics objects like quasars or galaxy clusters are both defined and described using their morphology. Since progress in physics often was based on a quantification of relevant properties, one may ask how to perform a quantitative morphometry. In the field of cosmology we have to characterize, e.g., the distribution of galaxies in large–scale structure surveys, or X–ray images of galaxy clusters quantitatively. Only a quantitative description of such data sets allows the comparison to analytical models. The geometry of cosmological structures is one of the basic tests for theories modeling structure formation in the Universe. Most theories of cosmological structure formation assume a homogeneous and isotropic Friedmann–Lemaître model as background and follow perturbations of this background (Peebles 1980; Goenner 1994). Since the collapse of overdensity regions depends on the values of the cosmological parameters characterizing the Friedmann–Lemaître models, a comparison between theories of structure formation and real observations is not only able to test the theories, but also to constrain the values of the cosmological parameters governing our Universe. Moreover, a number of astrophysical observations tell us, that we need matter not (yet?) visible (Dark Matter) in order to explain, e.g., the rotation curves of spiral galaxies, or why galaxy clusters are bound systems (Peebles 1993). Different types of Dark Matter (Ellis 2000) have a different influence on the formation of cosmic structure. In this line of thought the geometry of large–scale structure as well as the morphology of overdense regions such as galaxy clusters are of large interest in order to test common theories of structure formation, to constrain the values of the cosmological parameters, and to illuminate the nature of the Dark Matter.

This work deals with the morphological and statistical description and analysis of cosmic structure. In the first part only spatial information is investigated. We characterize the morphology of point patterns and images using the hierarchy of Minkowski valuations known from integral geometry.

The *Minkowski valuations* describe the shape of a pattern embedded into Euclidean

space by mapping patterns to scalar, vector–, and tensor–valued quantities. They are distinguished by a few simple properties which set reasonable standards for a morphological description. All these properties state that the Minkowski valuations transform in a well–defined way if we apply topological or geometrical operations. Within the framework of integral geometry one can show that for each tensor rank only a finite number of linear independent Minkowski valuations exist.
The *scalar Minkowski functionals*, also known as Quermaß integrals, have been investigated for a long time. They are distinguished by a strict motion invariance and were in part analyzed, e.g., by Minkowski (1903). A milestone in their development is marked by the characterization theorem due to Hadwiger (1957). This theorem characterizes the space of all motion–invariant, continuous and additive functionals. The generalization to *vector–valued or motion–equivariant measures* was given by Hadwiger & Schneider (1971), followed by Schneider (1972a); Schneider (1972b) and Hadwiger & Meier (1974). In these works, a strict one–to–one correspondence between the scalars and the vectors was found.
Tensor–valued measures were – apart from a work by Müller (1953) – not discussed until the late nineties when McMullen (1997) raised the question of how to characterize tensor–valued measures in general. Recently, this question could be answered by Alesker (1999b) based upon an analysis of a wider class of scalar descriptors (Alesker 1999a). Remarkably, there is no strict isomorphism with the scalar and vector–valued Minkowski valuations any more. Thus, a new picture is being established, where the well–known Quermaß integrals mark only the bottom of a hierarchy of motion–covariant measures.
In this chapter, the hierarchy of Minkowski valuations is introduced and described in detail. The main attention is focused on the tensors, which so far have been analyzed only coarsely. In particular, we need methods to compute the higher–order Minkowski valuations effectively. Within our general approach of covariant measures the scalar and vector–valued Minkowski valuations naturally arise as a byproduct.
Whereas the sections 1.1–1.6 comprise a lot of technical details, some simple examples of how the Minkowski valuations work in characterizing patterns are given in Section 1.7. The geometrical meanings of the Minkowski valuations are summarized in Table 1.1.

1.1 Basic elements of a covariant integral geometry

In this section, we formally introduce the basic concepts and notions of integral geometry.
Within the d–dimensional Euclidian space $\mathbb{E}^d$, which is identified with $\mathbb{R}^d$, the convex ring $\mathcal{K}^d$ comprises all convex and compact point sets; a member of $\mathcal{K}^d$ often is called a *body*. The convex ring is closed with respect to intersections: if $K_1, K_2 \in \mathcal{K}^d$, then

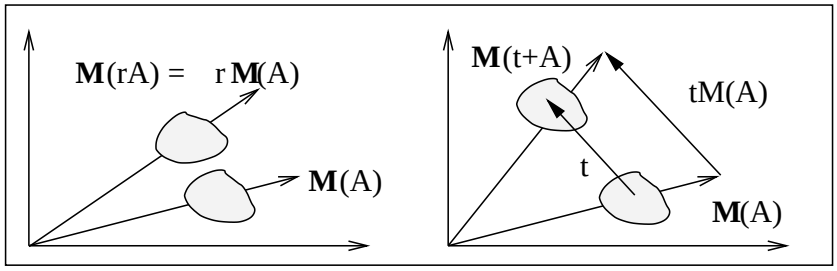

Figure 1.1: An illustration of motion equivariance for vector–valued functions.

also $K_1 \cap K_2 \in \mathcal{K}^d$. However, the union set $K_1 \cup K_2$ is in general not contained in $\mathcal{K}^d$. To close $\mathcal{K}^d$ with respect to set unions we move to $\mathcal{P}^d$, the polyconvex ring, which covers all *patterns* P, which can be represented by a finite union of bodies $P = \bigcup_{i=1}^{N} K_i$ with $K_i \in \mathcal{K}^d$.
Other operations of interest are the scaling of a body K with a real positive number λ: $\lambda K = \{\lambda \mathbf{x} | \mathbf{x} \in K\}$, and the Minkowski sum, which is defined as $K_1 \uplus K_2 \equiv \{\mathbf{x} | \mathbf{x} = \mathbf{x}_1 + \mathbf{x}_2 \text{ for } \mathbf{x}_i \in K_i\}$. Both $\mathcal{K}^d$ and $\mathcal{P}^d$ are closed with respect to the Minkowski sum. This sum allows us also to introduce the parallel body K_ϵ of $K \in \mathcal{P}^d$:

$$K_\epsilon = K \uplus \epsilon B_1(\mathbf{0}) \quad , \tag{1.1.1}$$

where $B_r(\mathbf{x})$ denotes a sphere of radius r centered on $\mathbf{x}$.
We are interested in functions describing patterns in $\mathcal{P}^d$. We do not want to constrain the values of these functions at this point, thus we choose a rather general approach and consider tensors. Let $\mathbb{T}_d^r$ denote the space of all symmetric tensors on $\mathbb{R}^d$ with rank r. Of course, $\mathbb{T}_d^0$ can be identified with $\mathbb{R}$, whereas $\mathbb{T}_d^1$ is isomorphic to $\mathbb{R}^d$. For $W_1 \in \mathbb{T}_d^r$ and $W_2 \in \mathbb{T}_d^s$ the symmetric tensor product is signified by $W_1 \otimes W_2 \in \mathbb{T}_d^{s+r}$, often we suppress the "$\otimes$". We also need the "Fock space", $\mathbb{T}_d \equiv \bigoplus_{r=0}^{\infty} \mathbb{T}_d^r$. Now we consider tensor–valued functions,

$$\phi : \mathcal{P}^d \to \mathbb{T}_d : K \mapsto \phi(K) \in \mathbb{T}_d \tag{1.1.2}$$

We constrain the space of functions of this sort by three types of requirements which set reasonable standards for a morphological description.

1. We demand *continuity* on $\mathcal{K}^d$. Since $\mathbb{T}_d^r$ is isomorphic to $\mathbb{R}^{\alpha_d}$, where $\alpha_d = \binom{d-1+r}{r}$, $\mathbb{T}_d^r$ has a natural topology. $\mathcal{K}^d$ also can be equipped with a metric, the Blaschke–Hausdorff metric[1]. However, it is not useful to demand the continuity on the whole $\mathcal{P}^d$. As obvious from, e.g., two merging convex cubes, the continuity on $\mathcal{P}^d$ is restrictive to a degree that even the Euler characteristic is not continuous any more. Thus, on $\mathcal{K}^d$ we demand a strict continuity, whereas on $\mathcal{P}^d$ we postulate conditional continuity, which refers only to convex bodies.

[1]The Blaschke–Hausdorff distance $d_B()$ between $K_1, K_2 \in \mathcal{K}^d$ is defined by $d_B(K_1, K_2) = \inf\{\epsilon | K_1 \subset K_2 \uplus \epsilon B_1(\mathbf{0}) \text{ and } K_2 \subset K_1 \uplus \epsilon B_1(\mathbf{0}))\}$.

2. We only consider *valuations*. Valuations add up like a volume, i.e. if $K_1, K_2 \in \mathcal{P}^d$:

$$\phi(K_1 \cup K_2) = \phi(K_1) + \phi(K_2) - \phi(K_1 \cap K_2) \quad . \tag{1.1.3}$$

   This requirement is not only a practical standard for morphological measures, but also useful for the mathematical theory: one can extend measures defined on $\mathcal{K}^d$ to $\mathcal{P}^d$ by taking the r.–h.–s. of Equation (1.1.3) as a definition of the l.–h.–s.. From a mathematical point of view, it is important to guarantee that this extension is unique. In our case, a theorem by Groemer (1978) states that every additive, continuous mapping f from $\mathcal{K}^d$ to an arbitrary $\mathbb{R}$–vector space has a unique extension to $\mathcal{P}^d$. Since $\mathbb{T}_d^r$ can be thought of as a vector space, and since we only consider continuous functions, the uniqueness of an extension is ensured[2]. Note that each integral over the volume or the surface of $P \in \mathcal{P}^d$ naturally fulfills the additivity.

3. Moreover, we ask for *motion–covariant* measures (we also speak of isometry–covariant measures). The Euclidian motion group consists of rotations (and inversions) and translations, we consider each class of motions separately. Each rotation $R \in SO(d)$ has a natural representation in $\mathbb{T}_d^r$ and $\mathbb{T}_d$. We demand that

$$\phi(RK) = R\phi(K) \quad . \tag{1.1.4}$$

   In this work we consider mainly $O(d)$–invariant measures. For dimensions $d > 2$ there is no difference between $SO(d)$– and $O(d)$–covariant continuous valuations. However, in two dimensions, the class of $SO(2)$–covariant continuous valuations is slightly larger than the class of $O(2)$–covariant continuous valuations (Alesker 1999b).
   For translations represented by a translation vector $\mathbf{t}$, we require that there is a number $r \in \mathbb{N}$ such that for all $K \in \mathcal{K}^d$

$$\phi(K + \mathbf{t}) = \sum_{i=0}^{r} \phi_{r-i}\, \mathbf{t}^i \tag{1.1.5}$$

   with some tensor–valued valuations ϕ_{r-i}. Note, that all expressions like $\mathbf{t}^i$ have to be understood as tensor products. We assume, that the degree of this polynomial expansion is uniquely bound. In the following we focus on valuations which map $\mathcal{P}^d$ into a subspace $\mathbb{T}_d^r \in \mathbb{T}_d$, in this case the polynomial arising in the translation formula (1.1.5) is of degree at most r. The mathematicians speak of "polynomial valuations of degree at most r."

The Minkowski valuations (MVs, for short) are the continuous and isometry–covariant valuations. For the following, let $\mathcal{F}_d$ denote the vector space comprising all scalar

[2]For the scalar Minkowski functionals, Hadwiger (1957) follows an alternative way by constructing the Euler characteristic directly on $\mathcal{P}^d$ and introducing the other functionals via the Euler characteristic.

Minkowski valuations, and $\mathcal{F}_d^r$ the space of all Minkowski valuations with values in $\mathbb{T}_d^r$. In particular, ${\mathcal{F}_d}^0$ is the space of all Minkowski functionals (MFs for the sequel). But how many Minkowski valuations do exist and what is their geometrical meaning? We start to answer this question in the next section using the formula of Steiner.

1.2 Mixed measures and the formula of Steiner

For an explicit construction of the Minkowski valuations we start with convex bodies K and K_i, and the volume, the mass vector

$$M(K) \equiv \int_K \mathrm{d}V\mathbf{x} \quad , \tag{1.2.6}$$

and higher–order mass tensors:

$$M^r(K) \equiv \int_K \mathrm{d}V\mathbf{x}^r \quad . \tag{1.2.7}$$

Surely, these quantities fulfill the requirements listed above and are thus part of the family of the Minkowski valuations. Note, that these quantities contain the simplest description of a body in terms of its size and position.
Now image, the body K is growing. One possibility to model its growth is to construct the parallel body K_ϵ which again can be characterized using the hierarchy of mass moments in Equation 1.2.7. Now it is possible to expand the mass moments of K_ϵ in a power series in ϵ:

$$M^r(K_\epsilon) = \sum_{i=0}^{d+r} \epsilon^i M_i^r(K) \quad . \tag{1.2.8}$$

This can be proven in analogy to Schneider (1972a). In this expansion, tensor–valued coefficients arise which depend only on the original body K. For $r = 0$ this is the formula of Steiner[3]. The coefficients M_i^r can be calculated from the above expansion (1.2.8) by applying the differential operator

$$D_i = \frac{1}{i!}\frac{\mathrm{d}^i}{\mathrm{d}\epsilon^i}\bigg|_{\epsilon=0} \tag{1.2.9}$$

to $M^r(K_\epsilon)$. A simple calculation yields that the M_i^r are additive, continuous and motion–covariant. Thus, we have found a couple of new Minkowski valuations. Of course, $M_0^r = M^r$. But what are the geometrical meanings of the other coefficients M_i^r?

[3]In this context the case of $r = 1$ is special, since M_{d+1}^1 vanishes for any dimension. The reason basically is the system of the so–called "Hüllensätze" (Hadwiger & Meier 1974).

The growth of a body under parallel construction depends on the shape of the surface of K, especially its curvature. For a smooth surface ∂K it is possible to get explicit expressions for the coefficients M_i^r. From now on till the end of the present section, ∂K is assumed to be smooth.
For an infinitesimal $\mathrm{d}\epsilon$ the first order contribution to $M^r(K_\epsilon)$ is $\int_{\partial K} \mathrm{d}A\ \mathbf{x}^r \mathrm{d}\epsilon$ (Schneider 1999). Thus,

$$M_1^r = \int_{\partial K} \mathrm{d}A\ \mathbf{x}^r \quad . \tag{1.2.10}$$

Now we iterate equation (1.2.8) and expand $M^r(K \uplus \epsilon B_1(\mathbf{0}) \uplus \kappa B_1(\mathbf{0})) = M^r(K \uplus (\epsilon+\kappa)B_1(\mathbf{0}))$. In this way, we obtain the M_i^r of a parallel body. They again can be represented as a polynomial in κ; we get (compare Schneider 1999):

$$M_i^r(K + \kappa B_1(\mathbf{0})) = \sum_{j=0}^{d+r-i} \binom{i+j}{j} M_{i+j}^r \kappa^j \quad . \tag{1.2.11}$$

Therefore, the M_j^r for $j = 2, .., (d+r)$ arise in the expansion of $M_1^r(K + \kappa B_1(\mathbf{0}))$. On the other hand, we can represent the surface of K_ϵ by the Gaussian map relating the surface ∂K of the convex body K to the surface of the unit sphere $\mathcal{S}^{d-1}$:

$$\Omega : \mathcal{S}^{d-1} \to \partial K, \quad \omega \mapsto \mathbf{x}_K(\omega) \quad . \tag{1.2.12}$$

Furthermore, we need the unique normal vector $\mathbf{n}(\omega)$ at each point on the boundary of K, $\mathbf{x}(\omega) \in \partial K$, labelled by ω. Since in general $\mathrm{d}A = \mathrm{d}\omega\ s_{d-1}(R_1, .., R_{d-1})$, where $s_\nu(R_1, .., R_{d-1})$ is the νth elementary symmetric function[4] of the principal curvature radii R_i $(i = 0, .., d-1)$, we get (Schneider 1999)

$$\begin{aligned} M_1^r(K_\epsilon) &= \int_{\partial K_\epsilon} \mathrm{d}A\ x^r = \int_{\mathcal{S}^{d-1}} \mathrm{d}\omega s_{d-1}(R_1^{K_\epsilon}, .., R_{d-1}^{K_\epsilon})(\mathbf{x}_{K_\epsilon}(\omega))^r \\ &= \int_{\mathcal{S}^{d-1}} \mathrm{d}\omega\ s_{d-1}(R_1^K + \epsilon, .., R_{d-1}^K + \epsilon)(\mathbf{x}_K(\omega) + \epsilon \mathbf{n}_K(\omega))^r \\ &= \sum_{j=0}^{r} \sum_{i=0}^{d-1} \int_{\mathcal{S}^{d-1}} \mathrm{d}\omega\ \epsilon^i s_{d-i}(R_1^K, .., R_{d-1}^K) \binom{d-1}{i} \binom{r}{j} \mathbf{x}_K(\omega)^j \mathbf{n}_K(\omega)^{r-j} \epsilon^{r-j} \quad . \end{aligned}$$

It is thus possible to write all of the coefficients M_i^r for $i = 2, .., d+r$ as an integral over the surface of K. Suppressing the indices K and the ω–dependence, we get for $i = 2, .., (d+r)$:

$$M_i^r = \sum_{j=r+1-i}^{r} \binom{r}{j} \binom{d-1}{i+j-r-1} \int_{\mathcal{S}^{d-1}} \mathrm{d}\omega \mathbf{x}^j \mathbf{n}^{r-j} s_{d+r-i-j} \quad . \tag{1.2.13}$$

[4] In d dimensions, the elementary symmetric functions are functions of $(d-1)$ arguments and defined via the expansion $\Pi_{i=1}^{d-1}(R_i + \epsilon) = \sum_{j=0}^{d-1} \binom{d-1}{j} \epsilon^j s_{d-1-j}(R_1, ..., R_{d-1})$.

Here, $\binom{i}{j} = 0$ for $j > i$ or $j < 0$. –Thus, the M_i^r are integrals over the surface of K, weighted with the curvatures, the positions, and the local normal vectors. Under a homogeneous scaling, they transform like

$$M_i^r(\epsilon K) = \epsilon^{d-i} M_i^r(K). \tag{1.2.14}$$

Thus, we have constructed a number of valuations $M_i^r \in \mathcal{F}_d^r$; for smooth $K \in \mathcal{K}^d$ these valuations can be represented as integrals over K or its surface ∂K. Therefore, these measures have simple geometrical meanings: In two dimensions, the scalar Minkowski functionals are the surface content of the pattern, its perimeter and its mean curvature, which is connected to the Euler characteristic via the Gauß–Bonnet theorem. In three dimensions, we have the volume, the surface content, the integrated mean curvature, and the integrated Gaussian curvature, which again yields the Euler characteristic. The higher–order Minkowski valuations are moments of the scalar ones. They weight the local curvatures with powers of the position and normal vectors.
The scalar Minkowski functionals are important for the development of the further theory: They allow us to generalize the curvature integrals we were dealing with to non–smooth surfaces. This is possible by a move to local measures. For the following it is useful to remind that the volume of the parallel body K_ϵ can be expressed as a polynomial in ϵ.

1.3 Local measures

So far, our discussion referred to regular surfaces only, where the surface element, the curvature and the normal vector are uniquely defined. Now we extend our approach to non–regular surfaces. In view of the tensors, we have to choose a slightly different approach from (Schmalzing 1996), rather we follow (Schneider 1993). The reason is basically, that we need a generalization of normals for non–regular surfaces.
Consider an arbitrary convex body $K \in \mathcal{K}^d$. For each point $\mathbf{x} \in \mathbb{R}^d$, therefore, the projection on K, $\mathbf{p}_K(\mathbf{x})$, that is the closest point of K from $\mathbf{x}$, and the unit vector $\mathbf{n}_K(\mathbf{x})$ pointing from $\mathbf{p}_K(\mathbf{x})$ to $\mathbf{x}$ are uniquely determined. Of course, $\mathbf{p}_K(\mathbf{x}) \in \partial K$. The mapping

$$f_K^\rho : K_\rho \setminus K \to \mathbb{R}^d \times \mathcal{S}^{d-1}, \quad \mathbf{x} \mapsto (\mathbf{p}_K(\mathbf{x}), \mathbf{n}_K(\mathbf{x})) \tag{1.3.15}$$

is called the support mapping[5].
Now turn around this line of argumentation and consider for a given Borel set $\mathcal{B} \subset \mathbb{R}^d \times \mathcal{S}^{d-1}$ the inverse image of f_K^ρ, $(f_K^\rho(\mathcal{B}))^{-1}$. For $\mathcal{B} = \{\mathbf{x}\} \times \mathcal{S}^{d-1}$ we simply get the normal bundle of $\mathbf{x}$; as illustrated in Figure 1.2, a smaller $\gamma \subset \mathcal{S}^{d-1}$ cuts out a piece of the normal bundle, we speak of a generalized normal bundle: $\mathrm{nor}_K(\mathcal{B}, \rho)$.
The dimension of the normal bundle allows us to classify different pieces of the

[5]In the sequel, we identify $\mathcal{S}^{d-1}$ and the set of all normals.

surface of K. If the surface ∂K is regular around a point $\mathbf{x}$, then the generalized normal bundle reduces to

$$\{\mathbf{x} + \lambda\mathbf{n} | \lambda \in [0, \rho]\} \quad , \tag{1.3.16}$$

where $\mathbf{n}$ denotes the unique normal vector at $\mathbf{x}$. In the case of edges, corners or other irregularities, the generalized normal bundle degenerates. The higher the dimension of $(f_K^\rho)^{-1}(\mathbf{x})$ is, the more irregular is the surface around $\mathbf{x}$. This enables us to introduce the generalized surfaces $\partial^\nu K$ by

Definition 1.1 *Generalized surfaces. For a convex body $K \in \mathcal{K}^d$ and $\nu = 1, .., d$, the νth generalized surface is given by*

$$\partial^\nu K = \{\mathbf{x} \in \partial K | \dim((f_K^\rho)^{-1}(\{\mathbf{x}\} \times \mathcal{S}^{d-1})) \geq \nu\} \quad . \tag{1.3.17}$$

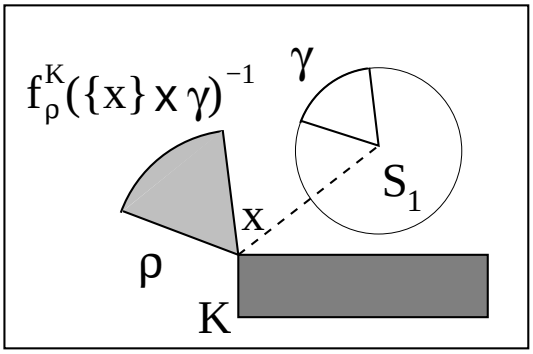

Figure 1.2: A sketch illustrating the construction of generalized normal bundles.

It can be shown that the dimension $\dim(\partial^\nu K) \leq d - \nu$. Obviously, $\partial^1 K = \partial K$.

Now we can define local curvature measures even for non–regular surfaces: the volume of $\mathrm{nor}_K(\mathcal{B}, \rho)$ can be expanded in powers of ρ (Schneider 1993):

$$V(\mathrm{nor}_K(\mathcal{B}, \rho)) = \sum_{\nu=0}^{d} V_\nu(\mathcal{B}, K) \binom{d}{\nu} \rho^\nu \tag{1.3.18}$$

with coefficients V_ν. This is a local version of Steiner's formula, for details and a proof see (Schneider 1993, p. 201).

It is useful to express this result in terms of local measures. If $\mu_d(\mathcal{B})$ denotes the Lebesgue measure of $\mathrm{nor}_K(\mathcal{B}, \rho)$, then we have:

$$\mu_d(\mathrm{nor}_K(\mathcal{B}, \rho)) = \frac{1}{d} \sum_{\nu=0}^{d-1} \Theta_\nu(\mathcal{B}, K) \binom{d}{\nu} \rho^{d-\nu} \tag{1.3.19}$$

with the generalized curvature measures Θ_ν on the set of all Borel sets $\mathcal{B} \subset \mathbb{R}^d \times \mathcal{S}^{d-1}$. They allow us to introduce "curvatures" even for non–regular surfaces, and to introduce normals on non–regular surfaces, too. So we can define normal–weighted integrals over non–regular surfaces. Of course, these measures vanish, if the spatial part of $\mathcal{B}$, $P_1(\mathcal{B}) \not\subseteq \partial K$. The Θ_ν can be calculated using

$$\Theta_\nu(\mathcal{B}, K) = \frac{d}{\binom{d}{\nu}} D_{d-\nu} \mu_d(\mathrm{nor}_K(\mathcal{B}, \rho)) \quad , \tag{1.3.20}$$

where D_ν is the differential operator given by (1.2.9). In other words, what we are doing with corners and the other non–regular pieces of ∂K, is to sum up all contributions arising from those normals which "span" the normal bundle.
For our applications it is useful to cast these results into a simpler form. Within the Boolean grain model described in Chapter 2.1 typically corners and edges arise, where two or more spheres intersect. It seems useful to combine the contributions of each generalized surface. We can proceed analogously to Schmalzing (1996) and Mecke (1994), but have to carry along the unit sphere $\mathcal{S}^{d-1}$.
Let $\mathbf{x} \in \partial^\nu K$ denote a point on the νth generalized surface of K and $\mathbf{n}(\omega)$ be an arbitrary unit vector in $\mathcal{S}^{d-1}$ with direction ω. We approximate $\{\mathbf{x}\}\times\{\omega\}$ by a series of Borel sets $\mathcal{B}_n \subset \mathbb{R}^d \times \mathcal{S}^{d-1}$ of the form $\beta_n \times \sigma_n$, where $\beta_n \to \{\mathbf{x}\}$ and $\sigma_n \to \{\omega\}$. Then

$$V_\kappa^\nu(\mathbf{x},\mathbf{n}) = \lim_{n\to\infty} \frac{D_\kappa \mu_d(\mathrm{nor}_K(\mathcal{B}_n,\rho))}{\mu_{d-\nu}(\beta_n)\omega(\sigma_n)} \tag{1.3.21}$$

is a generalized density such that the generalization of an integral of the type

$$\int \mathrm{d}\omega s_\nu \mathbf{x}^q \mathbf{n}^p \tag{1.3.22}$$

equals

$$\sum_{\nu=1}^{d} \int_{\partial^\nu K} \int_{\mathcal{S}^{d-1}} \mathrm{d}\mu_{d-\nu} \mathrm{d}\omega^{d-1} V_\kappa^\nu(\mathbf{x},\mathbf{n}) \mathbf{x}^q \mathbf{n}^p \quad . \tag{1.3.23}$$

We can cast this result into a more convenient form if we resume all integrals over the $\partial^\nu K$ into a formal density which finds the right Lebesgue measures automatically (Mecke 1994; Schmalzing 1996).

1.4 The Characterization theorem

Using these generalized local curvature measures we can define further tensor–valued valuations on the whole $\mathcal{K}^d$. Let E_d denote the second–rank unit tensor in d dimensions, and ${E_d}^i$ its powers for $i \in \mathbb{N}$. We introduce Minkowski valuations via

$$M_{i,j,k,l}(K) \equiv {E_d}^i \int_{\partial K} \int_{\mathcal{S}^{d-1}} \mathrm{d}\Theta_j(\omega) \mathbf{x}^k \mathbf{n}^l \tag{1.4.24}$$

for $j = 0, .., (d-1)$, and

$$M^{i,r}(K) \equiv {E_d}^i \int_K \mathrm{d}V \mathbf{x}^r \quad . \tag{1.4.25}$$

Obviously, these tensors are motion–covariant, continuous and additive. The $M_{i,j,k,l}$ are of rank $(2i+k+l)$ and are homogeneous functions of K of degree $(j+k)$, whereas the $M^{q,r}$ have rank $(2q+r)$ and scale like $M^{q,r}(\lambda K) = \lambda^r M^{q,r}(K)$.
Now the question arises, whether these valuations are the only ones in $\mathcal{F}_d$. Recently, Alesker (1999b) proved a general characterization theorem:

Theorem 1.1 *Generalized Characterization theorem. If ϕ is a motion–covariant and continuous valuation on $\mathcal{K}^d$ for $d > 2$, then it is a linear combination of the $M_{i,j,k,l}$ and the $M^{q,r}$.*

The proof of this important result relies on the characterization of strictly translation–invariant and $O(d)$–covariant functionals given by Alesker (1999a). As mentioned above, for $d > 2$, it does not make any difference whether we require an $O(d)$– or a $SO(d)$–covariance. However, in two dimensions, there are valuations, which are $SO(d)$–, but not $O(d)$–covariant (Alesker 1999b). They are defined using $\tilde{\mathbf{n}} = D(\pi/2)\mathbf{n}$, where $D(\pi/2)$ rotates $\mathbf{n}$ counterclockwise with $\pi/2$:

$$M'_{i,j,k,l}(K) = \int_{\partial K} \int_{\mathcal{S}}^{1} \mathrm{d}\Theta_i(\omega)\mathbf{x}^j\mathbf{n}^k\tilde{\mathbf{n}}^k \tag{1.4.26}$$

In the following, however, we focus on $O(d)$–covariant measures[6].
Theorem 1.1 contains the well–known Hadwiger theorem as a subcase; it states that in d dimensions only (d+1) linear independent scalar (i.e. strictly motion–invariant) measures exist[7]. Equally, the characterization theorem (first proven by Hadwiger & Schneider 1971 on the basis of Schneider 1971) for vector–valued valuations according to which the vector space of motion–equivariant continuous valuations also is $(d+1)$–dimensional, is a corollary from this theorem. It is remarkable, however, that, in general, more than $(d+1)$ linear independent tensor valuations of rank $r \geq 2$ exist. The isomorphism between ${\mathcal{F}_d}^1$ and ${\mathcal{F}_d}^0$ therefore cannot be extended to higher–order tensors. Note, however, that Theorem 1.1 only shrinks the space of continuous tensor valuations from above; a closer analysis yields that a number of the functions $M^{i,r}$ and $M_{i,j,k,l}$ are dependent.
But at first it is useful to generalize Alesker's theorem onto $\mathcal{P}^d$.

Theorem 1.2 *Generalized Characterization theorem on $\mathcal{P}^d$. If ϕ is a motion–covariant and conditional continuous valuation on $\mathcal{P}^d$, then it is a linear combination of the additive extensions of the $M_{i,j,k,l}$ and the $M^{q,r}$.*

The proof is clear, since Groemer's theorem ensures the unique existence of the extensions.
As mentioned above, there are linear relations between the $M_{i,j,k,l}$ and the $M^{q,r}$. Using the integral theorem of Gauß, Schneider (1999) showed that

$$E_d M_i^{r-2} = \frac{1}{r-1} \sum_{j=r-1-i}^{r-1} \binom{r-1}{j} \binom{d-1}{i+j+1-r} M_{0,d+r+2-i-j,j,r-j} \tag{1.4.27}$$

[6]For completeness we mention the case of one dimension. Alesker (1999a) proved, that every continuous valuation $\phi : \mathcal{K}^1 \to \mathbb{R}$ is of the form $\phi([a,b]) = P(a) + Q(b)$, where P and Q denote continuous functions on $\mathbb{R}$. If ϕ is a polynomial valuation of degree at most l, then P and Q can be chosen as polynomials of degree at most $l+1$.

[7]Only the $M_{0,j,0,0}$ for $j = 0, .., (d-1)$ and $M^{0,0}$ are scalar.

for $r \geq 2$ and $i = 0, .., d + r - 2$.
Alesker's theorem ensures the uniqueness of additive, continuous, and motion–covariant descriptors. In this sense, the morphological description of a patterns in terms of the MVs is complete. – So far, we showed how to calculate them for a convex body. For patterns one has to apply additivity, or, more effectively to proceed in a similar manner as Mecke 1994; Beisbart 1997.

1.5 Second–rank Minkowski valuations

For the following applications, we concentrate on the scalar Minkowski functionals, their vector–valued counterparts, and on second–rank tensor valuations. In this section the relevant second–rank tensors in two and three dimensions are listed together with their basic relationships.
For the following it is useful to revise our conventions slightly: So far the elementary symmetric functions were always thought of as functions of the curvature radii. Since $s_{d-1-\nu}(R_1, .., R_{d-1}) = R_1 \cdots R_{d-1} s_\nu(\kappa_1, .., \kappa_{d-1})$, where the $\kappa_i = 1/R_i$ denote the principal curvatures, we replace $\mathrm{d}\omega s_\nu(R_1, .., R_{d-1})$ by $\mathrm{d}A s_{d-1-\nu}(\kappa_1, .., \kappa_{d-1})$. This yields representations as surface integrals which is more useful since it allows us to deal with patterns where negative curvatures arise, or where the Gaussian map is not well–defined any more. Thus, in the following, the elementary symmetric functions are always thought of as functions of the principal curvatures. Using this convention, the $M_{i,j,k,l}$ are written as ${E_d}^i \int_{\partial K} \mathrm{d}A s_{d-1-j} \mathbf{x}^k \mathbf{n}^l$. Note, that their meanings remain unchanged.
In two dimensions, we get the following second–rank tensors[8]

[8]The formula below are valid only for a convex body K with a smooth surface. For non–regular surfaces, the elementary symmetric functions have to be replaced by the generalized curvature measures. For patterns which are not convex one has to use additivity (1.1.3), see Mecke 1994.

Tensors in 2 dimensions: $\mathcal{F}_2^2$
The mass tensor $M^2 = M^{0,2}$:

$$M^2 = \int_K \mathrm{d}\mathbf{x}\ \mathbf{x}^2 \quad . \tag{1.5.28}$$

Tensors only containing scalar Minkowski valuations

$$M^{1,0} = E_2 M^0(K), \quad M_{1,1,0,0} = E_2 M^1(K), \quad M_{1,0,0,0} = E_2 M^2(K) \quad . \tag{1.5.29}$$

Tensors, which are surface integrals:

$$M_{0,1,2,0} = \int_{\partial K} \mathrm{d}A\mathbf{x}^2 \quad , \quad M_{0,0,2,0} = \int_{\partial K} \mathrm{d}A\kappa\mathbf{x}^2 \quad , \tag{1.5.30a}$$

$$M_{0,1,1,1} = \int_{\partial K} \mathrm{d}A\mathbf{x}\mathbf{n} \quad , \quad M_{0,0,1,1} = \int_{\partial K} \mathrm{d}A\kappa\mathbf{x}\mathbf{n} \quad , \tag{1.5.30b}$$

$$M_{0,1,0,2} = \int_{\partial K} \mathrm{d}A\mathbf{n}^2 \quad , \quad M_{0,0,0,2} = \int_{\partial K} \mathrm{d}A\kappa\mathbf{n}^2 \quad . \tag{1.5.30c}$$

Linear dependencies:

$$M_{0,1,1,1} = E_2 M^0 \quad , \quad \text{i.e.} \int_{\partial K} \mathrm{d}A x_i n_j = \delta_{ij} \int_K \mathrm{d}V \tag{1.5.31a}$$

$$M_{0,1,0,2} + M_{0,0,1,1} = E_2 M_1^0 \tag{1.5.31b}$$

$$M_{0,0,0,2} = E_2 M_2^0 \quad , \quad \text{i.e.} \int_{\mathcal{S}^{d-1}} \mathrm{d}\omega n_i n_j = \frac{1}{2}\delta_{ij} \int_{\partial K} \mathrm{d}A s_1 \tag{1.5.31c}$$

Here, we used, that in two dimensions, $s_0 = 1$ and $s_1 = \kappa_1 \equiv: \kappa$. It turns out that $\mathcal{F}_d^r$ is seven–dimensional. If the surface of K is not regular, one has to use the generalized local curvature measures such as in (1.4.24). In three dimensions, we have

Tensors in 3 dimensions: $\mathcal{F}_3^2$
The mass tensor $M^2 = M^{0,2}$:

$$M^2 = \int_K \mathrm{d}\mathbf{x}\, \mathbf{x}^2 \quad . \tag{1.5.32}$$

Tensors only containing scalar Minkowski functionals

$$M^{1,0} = E_3 M^0(K), \quad M_{1,3-i,0,0} = E_3 M^i(K) \quad \text{for} \quad i = 1,2,3 \quad . \tag{1.5.33}$$

Tensors, which are surface integrals:

$$M_{0,i,2,0} = \int_{\partial K} \mathrm{d}A s_{2-i} \mathbf{x}^2 \quad \text{for} \quad i = 0,1,2 \quad , \tag{1.5.34a}$$

$$M_{0,i,2,0} = \int_{\partial K} \mathrm{d}A s_{2-i} \mathbf{x}\mathbf{n} \quad \text{for} \quad i = 0,1,2 \quad , \tag{1.5.34b}$$

$$M_{0,i,2,0} = \int_{\partial K} \mathrm{d}A s_{2-i} \mathbf{n}^2 \quad \text{for} \quad i = 0,1,2 \quad . \tag{1.5.34c}$$

Linear dependencies:

$$M_{0,2,1,1} = E_3 M^0 \ , \quad \text{i.e.} \int_{\partial K} \mathrm{d}A x_i n_j \qquad = \delta_{ij} \int_K \mathrm{d}V \quad , \tag{1.5.35a}$$

$$M_{0,2,0,2} + 2M_{0,1,1,1} = E_3 M_1^0 \quad , \tag{1.5.35b}$$

$$2M_{0,1,0,2} + M_{0,0,1,1} = E_3 M_2^0 \quad , \tag{1.5.35c}$$

$$M_{0,0,0,2} = E_3 M_3^0 \ , \quad \text{i.e.} \int_{\mathcal{S}^{d-1}} \mathrm{d}\omega n_i n_j = \frac{1}{3}\delta_{ij} \int_{\partial K} \mathrm{d}A s_2 \ . \tag{1.5.35d}$$

rank	abbreviation	in terms of the $M_{..}$	definition	meaning
0	V_0	M^0	$\int_K \mathrm{d}V$	volume
	V_1	$\frac{1}{4}M_{0,1,0,0}$	$\frac{1}{4}\int_{\partial K}\mathrm{d}S$	$\sim$ surface content
	V_2	$\frac{1}{2\pi}M_{0,0,0,0}$	$\frac{1}{2\pi}\int_{\partial K}\mathrm{d}S\kappa$	Euler characteristic
1	$\mathbf{V}_0$	M^1	$\int_K \mathrm{d}V\mathbf{x}$	mass vector
	$\mathbf{V}_1$	$\frac{1}{4}M_{0,1,1,0}$	$\frac{1}{4}\int_{\partial K}\mathrm{d}S\mathbf{x}$	
	$\mathbf{V}_2$	$\frac{1}{2\pi}M_{0,0,1,0}$	$\frac{1}{2\pi}\int_{\partial K}\mathrm{d}S\kappa\mathbf{x}$	Steiner point
2	VV_0	M^2	$\int_K \mathrm{d}V\mathbf{xx}$	mass/volume tensor
	VV_1	$\frac{1}{4}M_{0,1,2,0}$	$\frac{1}{4}\int_{\partial K}\mathrm{d}S\mathbf{xx}$	
	VV_2	$\frac{1}{4}M_{0,1,1,1}$	$\frac{1}{4}\int_{\partial K}\mathrm{d}S\mathbf{xx}$	
	VV_3	$\frac{1}{4}M_{0,1,0,2}$	$\frac{1}{4}\int_{\partial K}\mathrm{d}S\mathbf{xx}$	
	VV_4	$\frac{1}{2\pi}M_{0,1,2,0}$	$\frac{1}{2\pi}\int_{\partial K}\mathrm{d}S\mathbf{xx}$	
	VV_5	$\frac{1}{2}\pi M_{0,1,1,1}$	$\frac{1}{2\pi}\int_{\partial K}\mathrm{d}S\mathbf{xx}$	
	VV_6	$\frac{1}{2\pi}M_{0,1,0,2}$	$\frac{1}{2\pi}\int_{\partial K}\mathrm{d}S\mathbf{xx}$	

Table 1.1: A list of the two–dimensional Minkowski valuations we need.

1.6 Integral geometric results

Within the framework of integral geometry, one can derive a number of important results, which facilitate the computation of the Minkowski valuations both for given data and for analytical models. There is a very simple recipe to generate new integral geometric results: write down an expression, which obeys the basic covariance properties listed above and expand it in the basis of the Minkowski valuations. In such a way, the *principal kinematic Al formulae*, *Crofton's intersection formulae* and the *projection formulae* can be proved. For the scalar Minkowski functionals and their vector–valued counterparts these results are well–known. However, for the higher–order Minkowski valuations, such results were not yet proven. In Appendix A.1 some remarks on this are listed. Details of how the Minkowski functionals are calculated for relevant patterns can be found in the Appendices A.1 and A.1.2.
We conclude this chapter by a series of examples which show how the Minkowski valuations work in describing different patterns and in discriminating between them.

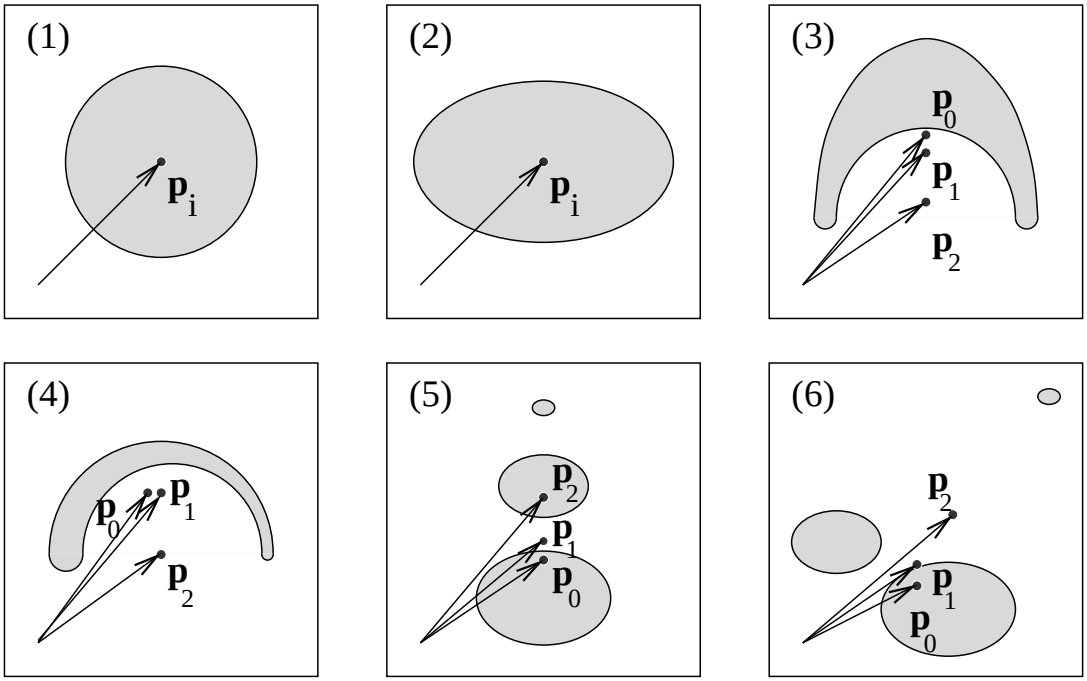

Figure 1.3: A number of simple patterns with their curvature centroids

1.7 The Minkowski valuations of simple patterns

Before turning to a couple of examples we show how to represent the Minkowski valuations in a convenient form. Some of the results derived in integral geometry assume a simpler form, when the Minkowski valuations are renormalized. Here we adopt the V–normalization; in Table 1.1 we list all two–dimensional functionals we need together with their meanings in two dimensions.
For a convenient graphical representation of the higher–order Minkowski valuations, it is useful to move to curvature centroids:

$$\mathbf{p}_i = \frac{\mathbf{V}_i}{V_i} \tag{1.7.36}$$

for $i = 0, .., d$ as far as $M_i > 0$. Usually, they lie within the convex hull of the pattern under consideration.
For a natural representation of the tensors, we transform them into a coordinate system centered on the corresponding curvature centroids. More precisely, the $M_{i,j,2,0}$ are calculated around $M_{0,j,1,0}$, and $M^{r,q}$ around M^1. The other tensors are translation–invariant and shown separately. To get coordinate–independent quantities we consider their eigenvalues.
Figure 1.3 displays a series of patterns showing the effect of symmetry reduction. For a spherically symmetric body, all curvature centroids coincide with the symmetry

center. Even for a point–symmetric geometry, the curvature centroids are identical. Note, however, that most of the tensors discriminate between the patterns (1) and (2). For the axial–symmetric configuration (3) the curvature centroids fan out along the symmetry axis. If no symmetry is present any more such as in panel (4), the curvature centroids span a triangle; the size of the triangle can serve as measure of the asymmetry. For patterns which consist of more than one component the curvature centroids weight the components in accordance with their scalar Minkowski functionals. In the fifth panel of Figure 1.3, $\mathbf{p}_0$ is attracted by the largest component at the bottom, whereas $\mathbf{p}_2$ weights all components equally. Panel (6) shows why we need higher–order Minkowski valuations for a good description of spatial data: the patterns in panel (5) and panel (6) cannot be distinguished by means of the scalar Minkowski functionals. However, the curvature centroids mark a difference between both patterns.

In Figure 1.4 we show a number of cellular patterns together with their tensor Minkowski valuations. They exemplify again the effect of symmetry reduction. The upper right panel shows that in cases of point symmetry the tensors are necessary to distinguish from spherical symmetry: Whereas the curvature centroids still coincide, the tensors reveal the anisotropy of the pattern. The lower right panel illustrates the fact, that sometimes the morphologically relevant directions can differ significantly even for a simple connected pattern. Note, that due to the lattice geometry $M_{0,1,0,2}$ (and thus also $M_{0,0,1,1}$) is always parallel to one of the lattice axes.

In summary: the Minkowski valuations allow a unique description of spatial data. They have simple geometrical meanings and are sensitive to symmetry and local morphology. In the next chapter, we show how to apply them to cosmological data sets.

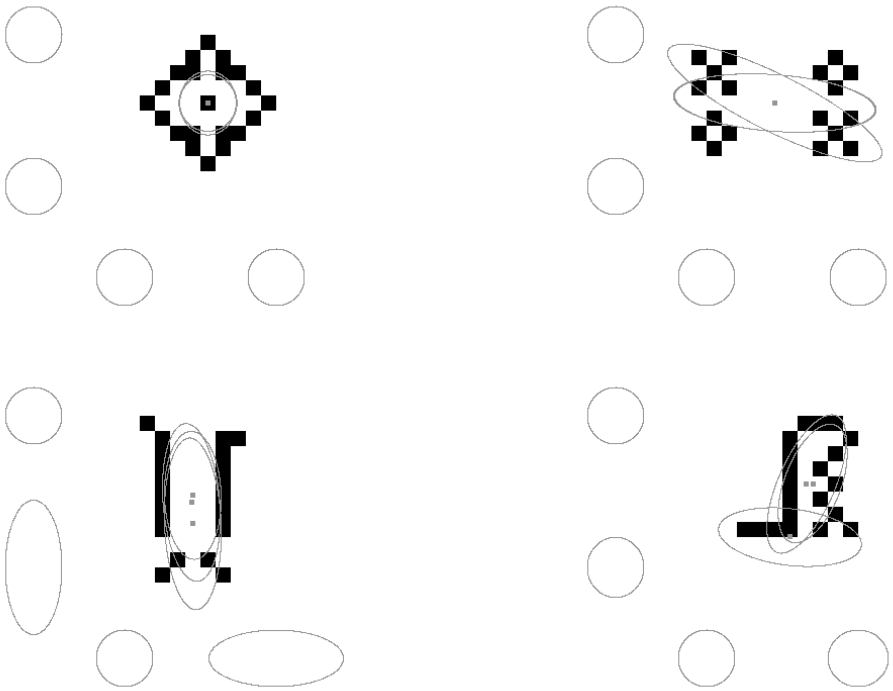

Figure 1.4: A couple of cellular patterns with their curvature centroids and their Minkowski tensors. The tensors M^2 and $M_{0,i,2,0}$ are calculated and shown with their corresponding curvature centroid as origin. The other tensors are translation–invariant, thus we show them separately, the left upper tensor: $M_{0,0,0,2}$, the left lower tensor: $M_{0,0,1,1}$, in the middle: $M_{0,1,1,1}$, on the right: $M_{0,1,0,2}$. The ellipses reflect the ratio of the eigenvalues, only, not their absolute amounts.

Chapter 2

Dealing with data – a step towards physical models

Cosmological data sets comprise the positions of galaxies in large–scale structure surveys as well as pixelized maps of, e.g., X-ray clusters such as shown in Figure 2.1. How is it possible to reveal the geometry of such data quantitatively?
In this chapter we show how to apply Minkowski valuations to such data sets (Beisbart et al. 2001). The first step is to interpret them as realization of a random process. This allows us to compare to models and to assess the significance of certain claims. In a second step, we have to associate patterns from the convex ring with the data to start the analysis with Minkowski valuations.
We combine the overview of the methods used later on with the discussion of a few models. The second part of the chapter is devoted to the morphological description of galaxy clusters. On the base of the Minkowski valuations we define and test a number of robust structure functions suited to feature different aspects of substructure to be found within galaxy clusters.

2.1 The structure of cosmological data sets

There are two basic types of cosmological data sets.

2.1.1 Fields

Cosmologically and astrophysically relevant fields like the density field or a surface brightness can be viewed as realizations of a random function from a more mathematical point of view. For an introduction to random fields see, e.g., Adler 1981. The basic description of a random field f can be given in terms of filters like:

$$\langle f(\mathbf{x})\rangle\,, \quad \langle f(\mathbf{x})f(\mathbf{y})\rangle\,, \quad \left\langle \int_P f(\mathbf{y})\mathrm{d}\mathbf{y}..\right\rangle \quad , \tag{2.1.1}$$

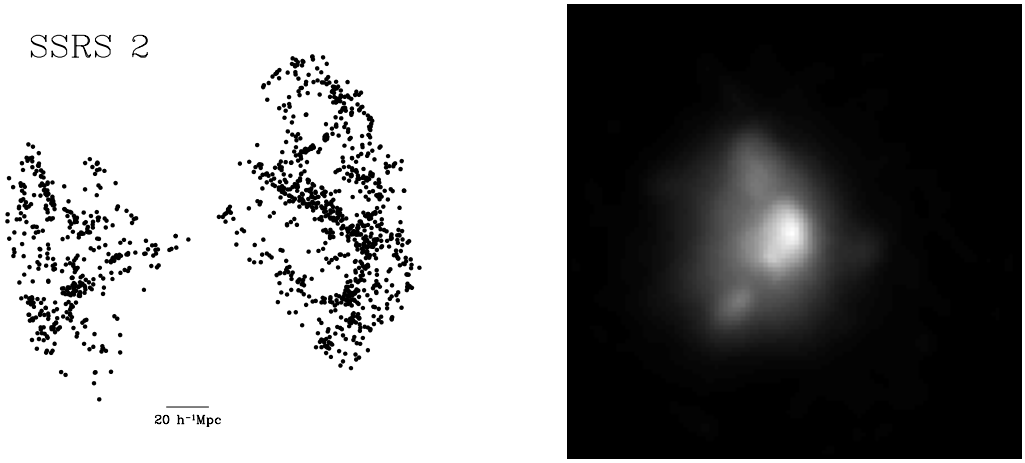

Figure 2.1: Examples of cosmological data sets: the SSRS 2 galaxy catalogue (left panel, for a description of the sample see Chapter 6 and da Costa et al. 1998) and a simulated X–ray cluster (Valdarnini et al. 1999).

where $\langle\rangle$ denotes an ensemble average and P is an arbitrary domain. A special, but simple model is a Gaussian random field, where all linear filters are Gaussian distributed.
Real data sets do not comprise a whole realization of a field, rather they are sampled, e.g., on pixels or voxels. Nevertheless, the picture of the random field is a useful idealization both for the construction of models and for the case where the pixel size is small in comparison to the scales of physical interest. – In principle, two sorts of sampling are possible.

1. Regular sampling. The field under consideration is sampled on a regular grid. Often, one can describe the pixelized maps themselves by a lattice model, which describes the pixelized field in terms of (joint) occupation probabilities. To make this type of data accessible to a MV–analysis one usually constructs *excursion sets* which comprise all pixels where the field exceeds a given threshold value v:
$$\mathcal{L}_v = \bigcup_{u_i \geq v} c_i \quad ; \tag{2.1.2}$$
the pixel cells are denoted by c_i, and u_i is the value of the field in this cell.

2. Irregular sampling. Sometimes the physical fields are sampled in an irregular fashion. There are two basic possibilities of how the proper physical field and the sampled data are related: Either the sampling is independent from the properties of the physical field (unbiased sampling); or it depends on the properties of the physical field itself. The cosmological bias problem of how the

mass of visible objects is related to the mass of the underlying Dark Matter, is an excellent example for the second case. Using the random field model, we can test whether a given sampling is unbiased (see the Chapter 6.3).

2.1.2 Point sets

Large–scale structure surveys comprise the positions of galaxies $\{\mathbf{x}_i\}_{i=1}^N$ found within a sampling window $\mathcal{D}$. We think of them as a realization of a *point process*; a point process randomly throws points into a window. This point of view allows us to apply a statistical description, to compare the data sets to analytical models and to ask for the statistical significance of an observed signal (Daley & Vere-Jones 1988; Stoyan & Stoyan 1994; Kerscher 1998). A complete description of a point process can be given in factorial moments or joint probability densities:

$$\varrho_n(\mathbf{x}_1, .., \mathbf{x}_n)\mathrm{d}\mathbf{x}_1 \cdots \mathrm{d}\mathbf{x}_n \tag{2.1.3}$$

is the probability of finding galaxies at the positions $\mathbf{x}_1, .., \mathbf{x}_n$. An elegant way to resume the whole hierarchy of n–point densities is to move to a generating functional (Balian & Schaeffer 1989; White 1979). To associate patterns accessible to the MVs with point sets, we use the following two methods:

1. We smooth the points using a Gaussian kernel to get a smooth density field and consider as above the *excursion sets*; the smoothing length χ fixes the scale of interest;

2. the *Boolean grain method* is applied: Here we put a ball of radius r around each point and study the union set of all these balls within a window $\mathcal{D}$ using the Minkowski valuations.
   For the Boolean grain method it is in principle possible to calculate expectation values for an arbitrary Minkowski valuation M and any point process. Starting with the additivity and averaging over the ensemble we get for the expectation value $\langle M \rangle$ of the Minkowski valuation M:

$$\begin{aligned}\langle M \rangle (r) = \sum_{n=1}^{\infty} \int_{\mathbb{R}^d} \mathrm{d}\mathbf{x}_1 \cdots \int_{\mathbb{R}^d} \mathrm{d}\mathbf{x}_n \frac{(-1)^{n+1}}{n!} \\ \times M\left(B_r(\mathbf{x}_1) \cap \cdots \cap B_r(\mathbf{x}_n)\right) \varrho_n(\mathbf{x}_1, .., \mathbf{x}_n).\end{aligned} \tag{2.1.4}$$

   The Minkowski valuations thus contain correlation functions of any order. Using the principal kinematic Al formulae, one can derive a generating functional for the scalar Minkowski functionals (Schmalzing et al. 1999b) and the vectors in a similar manner. For higher–order tensors, however, the general question of a principal kinematic Al formulae has not been answered yet.
   The simplest case of a point process is a Poisson process, where all n–point

densities factorize into a product of one–point–densities. The expectation values for the scalar Minkowski functionals were calculated by Mecke & Wagner (1991) for a general window $\mathcal{D}$ and the thermodynamic limit. If one replaces the scalar Minkowski functionals $M_\alpha(\mathcal{D})$ in their formula (14) by the corresponding vectors, one gets the expectation values for the vectors. In many cases, however, a simpler reasoning yields the correct results: if the window $\mathcal{D}$ is either point– or spherically symmetric, and the origin of a coordinate system it chosen to be the symmetry center, all vectors vanish on average. For an arbitrary origin, one gets the averaged vectors applying the transformation rule (A.1) in Appendix A and using the expectation values for the scalar Minkowski functionals.

Both methods employ two diagnostic parameters: The smoothing length or the radius of the Boolean grains (formally α) determines the scale we look at (scale of resolution), whereas the density threshold or the scale of the window (β) fixes the region of interest.

2.2 Structure functions

In the following chapter, we analyze galaxy clusters using Minkowski valuations. We are interested in the substructure to be found within the galaxy distribution, the DM, and the X-ray emitting gas in clusters. The challenge is to uncover substructure in systems which are already of intrinsically inhomogeneous shape. Different from large–scale structure investigations, we do not search for perturbations of a homogeneous background, but rather want to characterize smaller systems without any statistical assumptions.

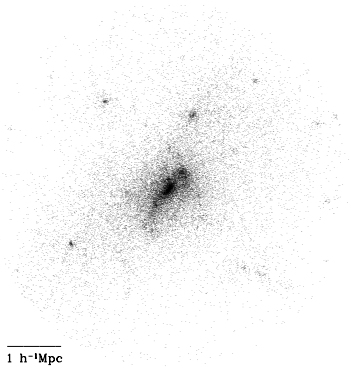

Figure 2.2: The cluster (a GIF cluster) to be investigated as an example. Results are shown in Figure 2.3. Throughout this part we show only 30% of the cluster points in plots of this style.

As an example, we investigate a two–dimensional projection of a realistic cluster using the Minkowski valuations. The cluster is one of the GIF clusters; it is shown in Figure 2.2; in Chapter 3.3 details of the image construction are given. We analyze the two–dimensional DM distribution using the excursion set approach. As a result some of the Minkowski valuations are plotted vs. density threshold in Figure 2.3. One can recognize that the curvature centroids are relatively stable, only

small shifts occur, when small subclumps fall out of the excursion sets. On the other hand, the eigenvalues of the tensors are quite different. This corresponds to the visual impression, that this cluster is elongated. The scalar, vector–, and tensor–valued Minkowski valuations thus contain very detailed information. However, for a statistical comparison between, e.g., large cluster samples it is useful to condense the information further. In this section we construct a number of structure functions (SFs, for short), which feature different aspects of substructure.
We distinguish different aspects of substructure systematically. We propose the following four classes of aspects of substructure. Each aspect ("morphotype") can be quantified using one or more robust structure functions, constructed using the MVs. Note, that substructure can only be defined with respect to a known reference state. This reference state should be the imprint of a dynamical equilibrium. Since a theory of equilibrium states for galaxy clusters has not yet been developed, we define a number of geometrical structure functions here and test afterwards their ability to reflect dynamical properties of clusters using numerical simulations in Chapter 3.4.
Another question arising if we compare different patterns is how to scale the different data. This question has to be answered using the physical interest; we may want to compare the substructure relative to the pattern scale or the substructure at a given physical scale[1].
For the definition of the robust structure functions, we assume that we have the Minkowski valuations v_μ as a function of the pattern $P_{\alpha,\beta}$ constructed from the data with a resolution scale α and the size of the window β: $V_\mu = V_\mu(P_{\alpha,\beta})$. Suppose, furthermore, that we have measures for both the variables α and β: $\mathrm{d}\mu_\alpha$ and $\mathrm{d}\mu_\beta$. The measures are normalized in such a way, that

$$\int \mathrm{d}\mu_i = 1 \tag{2.2.5}$$

for $i \in \{\alpha, \beta\}$. Natural representations of the MVs are

$$V_\mu(\beta) = \int \mathrm{d}\mu_\alpha V_\mu(P_{\alpha,\beta}) \quad . \tag{2.2.6}$$

and

$$V_\mu(\alpha) = \int \mathrm{d}\mu_\beta V_\mu(P_{\alpha,\beta}) \quad . \tag{2.2.7}$$

A natural method to concentrate the morphological information contained in the MVs is to construct an average over a special function of the Minkowski valuations by:

$$\langle f \rangle_{\mathrm{u}} \equiv \int \mathrm{d}\mu_\alpha \mathrm{d}\mu_\beta f(V_\mu(P_{\alpha,\beta})) \quad . \tag{2.2.8}$$

[1]More precisely, there are two separate questions: a. whether to scale the smoothing length according to the scale of the object b. how to scale the results of the MVs, which are in general not dimensionless.

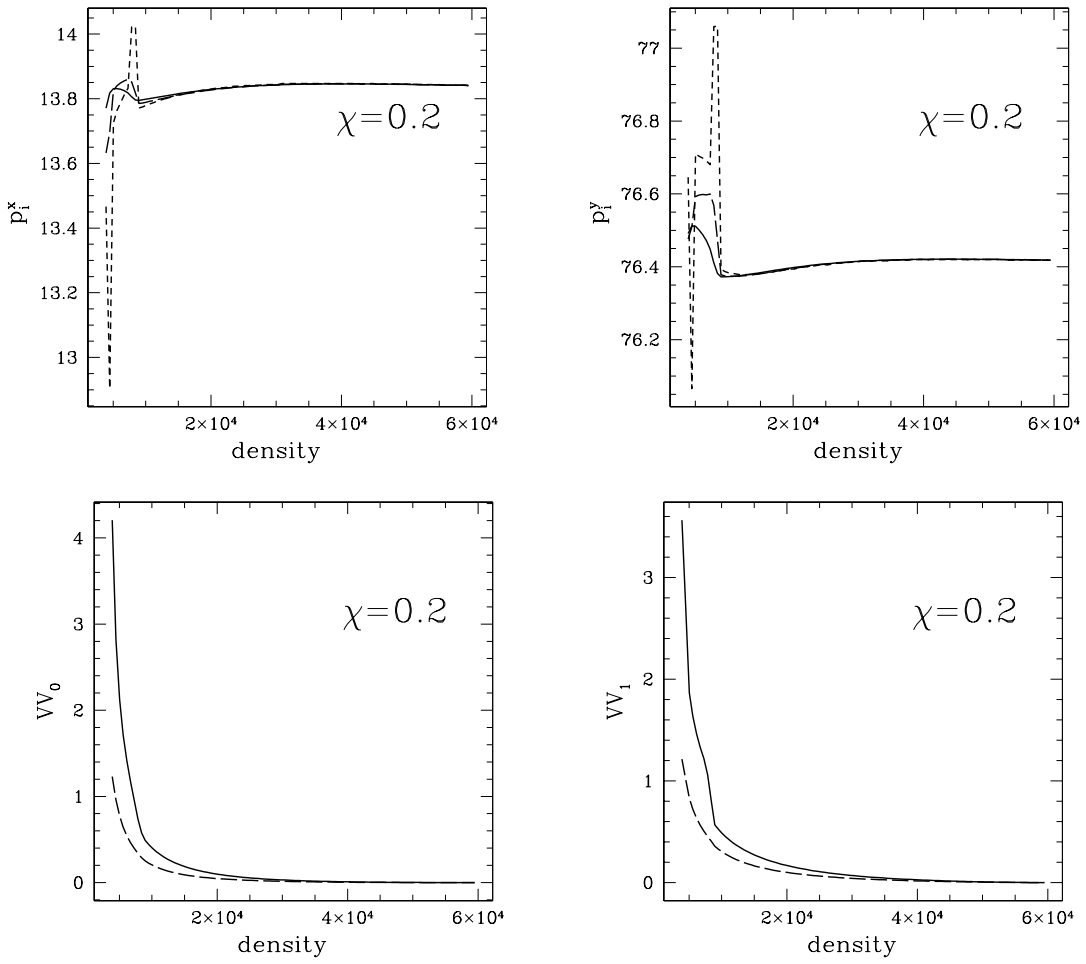

Figure 2.3: A vector– and tensor–valued analysis of the GIF cluster shown in Figure 2.2. In the upper panels, both components of the curvature centroids are plotted vs. density threshold. $\mathbf{p}_0$: solid line; $\mathbf{p}_1$: long dashed line, $\mathbf{p}_2$: short dashed line. The x–direction is the horizontal direction in Figure 2.2. The lower panels show the eigenvalues of two of the tensors. These results were gained using a finer grid resolution than usual, namely 512×512 pixels. The density is given in units of particles per $h^{-1}\mathrm{Mpc}^2$, the results are given in units of powers of $h^{-1}\mathrm{Mpc}$.

For the measures μ_α, μ_β, we have in principle the freedom of choice, but usually we pick up one certain scale of resolution α_0 and average over the window sizes: $\mathrm{d}\mu_\alpha \mathrm{d}\mu_\beta = \delta(\alpha-\alpha_0)\mathrm{d}\alpha\theta(\beta_{max}-\beta)\theta(\beta-\beta_{min})\frac{1}{\beta_{max}-\beta_{min}}\mathrm{d}\beta$ or proceed the other way round[2]. β_{min} and β_{max} are appropriately chosen values of, e.g., the density. This notation covers also the case where one pair of values for α and β is distinguished as a natural choice.
For the analysis of pixelized maps by means of the excursion set approach we use the measure $\delta(\alpha-\alpha_0)\mathrm{d}\alpha\theta(\beta_{max}-\beta)\theta(\beta-\beta_{min})\frac{1}{\beta_{max}-\beta_{min}}\mathrm{d}\beta$ and the following structure functions. They are constructed in such a way, that they become zero for spherically symmetric, substructure–poor patterns. Here we focus on the case of two dimensions; for most of the structure functions a generalization to other dimensions is straightforward.

1. Clumpiness. An inhomogeneous pattern may consist of a number of subclumps. Frequently, a galaxy cluster is generated by a merging of two groups which can still be distinguished within the cluster. A natural measure at this point is the Euler characteristic, which in the simplest case counts the components of a pattern. Thus we define the clumpiness as

$$\mathrm{C} = \sqrt{\langle(\chi-1)^2\rangle_{\mathrm{u}}} \quad . \tag{2.2.9}$$

   If C>0, a number of subclumps are to be expected.

2. Shape and Asymmetry. Another important question is: how does the shape of the pattern look like? Is it roughly spherical, or are there corners, and are the isodensity contours very crooked? – The global appearance of a pattern is reflected by the eigenvalues of the Minkowski tensors. These quantities mirror the symmetry of the pattern (and aspects of the shape: is the cluster elongated?), *cf.* the examples in Chapter 1. We define a number of symmetry parameters:

$$\mathrm{X}_i \equiv \left\langle 2\frac{\lambda_1^i - \lambda_d^i}{\lambda_1^i + \lambda_d^i}\right\rangle_{\mathrm{u}} \tag{2.2.10}$$

   for $i = 0, .., \dim(\mathbb{T}_r^d)$, where λ_1^i and λ_d^i are the largest and the smallest eigenvalue of the ith tensor VV_i, respectively (these are generalizations of the axial ratios discussed by Mohr et al. 1995b). In practice we mainly consider the eigenvalues of the volume tensor M^2 and the surface tensor $M_{0,1,2,0}$, which can be computed using the Crofton formulae (see Chapter A.1)[3].
   As shown in Figure 1.3, curvature centroids which do not coincide indicate the

[2] In our numerical analysis we approximate the integral by a sum over 101 bins.
[3] The isoperimetric ratio

$$I_1 \equiv \frac{4V_1^2}{\pi V_2 V_0} \tag{2.2.11}$$

may be another useful descriptor characterizing the global shape of a pattern. The isoperimetric

asymmetry of a pattern. For a quantitative characterization, we consider the triangle spanned by the curvature centroids and ask for its length of circumference and its surface content[4].

$$\mathrm{A}_0 \equiv \langle V_0(\triangle(\mathbf{p}_i))\rangle_{\mathrm{u}} \quad , \tag{2.2.13}$$

$$\mathrm{A}_1 \equiv \langle 4V_1(\triangle(\mathbf{p}_i))\rangle_{\mathrm{u}} \quad . \tag{2.2.14}$$

If $A_0 > 0$ or $A_1 > 0$, the cluster under investigation is asymmetric. Note, that these substructure measures have a dimension; thus, different clusters should be compared carefully. Sometimes it is useful to scale these parameters to the cluster size R_{cl}:

$$\mathrm{A}'_0 \equiv \langle V_0(\triangle(\mathbf{p}))\rangle_{\mathrm{u}} / R_{cl}^2 \quad , \tag{2.2.15}$$

$$\mathrm{A}'_1 \equiv \langle 4V_1(\triangle(\mathbf{p}))\rangle_{\mathrm{u}} / R_{cl} \quad . \tag{2.2.16}$$

3. Shift of morphological properties. Although the single isodensity contours may be spherically symmetric, the center of mass of the cluster may shift if we vary the density threshold. This was the original idea of the centroid shift (Mohr et al. 1993). More generally, all morphological properties may wander in space if we regard the cluster at different values of the density threshold. Thus we follow the path of the curvature centroids to get the following set of morphological parameters:

$$\mathrm{s}_i \equiv \int_{u_{min}}^{u_{max}} \left| \frac{\mathrm{d}\mathbf{p}_i}{\mathrm{d}u} \right| \mathrm{d}u \tag{2.2.17}$$

for $i = 0, .., 2$. Sometimes, however, these functions do not converge fast enough if we refine the resolution of the grid. As a more stable alternative we use[5]:

$$\mathrm{S}_i \equiv \sqrt{\left\langle (\mathbf{p}_i - \langle \mathbf{p}_i \rangle_{\mathrm{u}})^2 \right\rangle_{\mathrm{u}}} \quad . \tag{2.2.18}$$

4. Twist of morphological properties. Equally morphological relevant directions may change, if we enlarge the window or change the density threshold. This

inequality (Fenchel 1936; Alexandrov 1937; Schmalzing et al. 1999a) states that

$$I_1 \geq 1 \tag{2.2.12}$$

for convex bodies. The equality holds for, e.g., circles. If the isoperimetric ratio is larger than one, the shape of the cluster gets elongated, or the isodensity curves are very crooked. However, in practice this statistics does not work since often non–convex patterns are present within clusters. – This statistics is related to the shapefinders (Schmalzing et al. 1999a; Sahni et al. 1998).

[4]In the general case of d dimensions, we take the d non–trivial MFs of the simplex spanned by the curvature centroids $\triangle(\mathbf{p}_i)$

[5]This is a generalization of the centroid variation discussed by Mohr et al. (1995b).

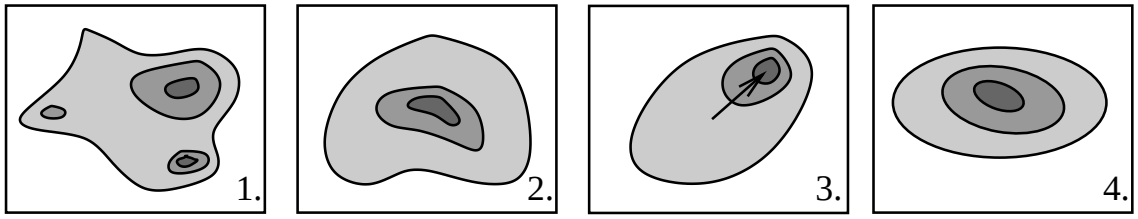

Figure 2.4: The basic morphotypes: Clumpiness, asymmetry and shape, shift and twist of morphological properties.

aspect of substructure can be featured using the Minkowski tensors. We concentrate on the second position moments and characterize the direction of the largest eigenvalue using the angle ϕ_i. Thus

$$\mathrm{T}_i \equiv \left\langle \left| \frac{\mathrm{d}|\phi_i|}{\mathrm{d}u} \right| \right\rangle_{\mathrm{u}} \tag{2.2.19}$$

for $i = 1, .., \dim(\mathbb{T}_2^d)$ characterizes the angular motion of the eigen direction determined by the largest eigenvalue[6]. In practice, the eigen directions of more or less isotropic tensors are not interesting, thus for the computation of the R_i, we exclude the ϕ_i for values of the density threshold, where $\frac{\lambda_1^i - \lambda_d^i}{\lambda_1^i + \lambda_d^i} \leq 0.2$. Moreover, we found that it is useful to exclude the very inner part of the cluster for this sort of analysis, thus we integrate only up to $0.8u_{max}$.

2.3 Tests

It is useful to probe the performance of our structure functions before applying them to data. Therefore, we test their robustness by statistical tests and apply the structure functions then to a number of model clusters. These tests facilitate the choice between the several structure functions for each morphotype, too.

2.3.1 Statistical robustness

To probe the robustness of our measures we use two different methods:

1. Poisson noise. How are the structure functions affected by random noise added to the true points? – We take one of the GIF clusters (the cluster is constructed as described in Subsection 3.2) and add Poisson points to the Dark Matter particles the cluster consists of within these simulations. More precisely, we have the cluster within a spherical window with a radius[7] of $\sim 3.4h^{-1}$Mpc. We

[6] See Mohr et al. 1995b; Fritsch 1996 for a comparison.

[7] h is the present day Hubble constant H_0 in usual units: $H_0 = h\frac{\mathrm{km/s}}{\mathrm{Mpc}}$.

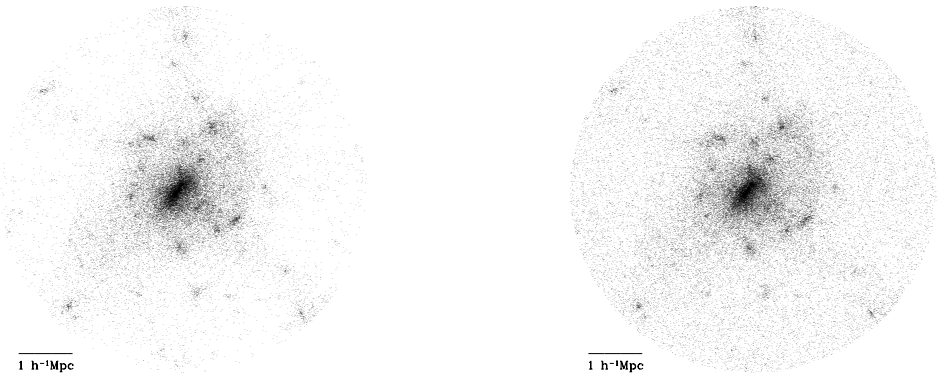

Figure 2.5: An illustration of how the data may be affected by noise. On the left hand side the full cluster within a large window, on the right hand side noise has been added (1600 noise points per $1h^{-1}$Mpc $\times$ $1h^{-1}$Mpc – this is about 40% noise). The cluster is one of the GIF clusters within the τCDM model at redshift $z = 0$.

add Poisson points and then determine the cluster and a region for boundary corrections as outlined in Subsection 3.2. The structure functions are calculated; the whole procedure is done for hundred realizations of random noise. In Figure 2.6 we show the mean structure functions and the 1σ bars vs. level of noise. In general, the structure functions are very stable, even Poisson noise at a level of fifty percent does not affect our results on average. For a smoothing of $0.2h^{-1}$Mpc, only S_2 shows a significant systematic deviation from the original clusters[8].

2. Subsampling. From the large "cluster image" of $\sim 3.4h^{-1}$Mpc size, we first subsample a certain percentage of points randomly and then treat the cluster as usual (see Subsection 3.2), the effect is illustrated in Figure 2.7. We average over 100 realizations of the subsampling and show the averages and the fluctuations in Figure 2.8. In general, the results are robust for all structure functions, only for smaller smoothing lengths of, e.g., $0.05h^{-1}$Mpc, we sometimes find systematic bias effects. The fluctuations are relatively small even for a subsampling of 50%. For the vector– and tensor–based measures, we find the general trend, that the structure functions relying on the volume are the most stable ones, followed by the surface– and curvature tensors.

This shows that the structure functions are stable and robust measures.

[8]Later on, we also need substructure functions which are normalized to the scale of the individual cluster. Since in this case the estimate of the cluster scale is strongly affected by the noise, some of the structure functions are, too.

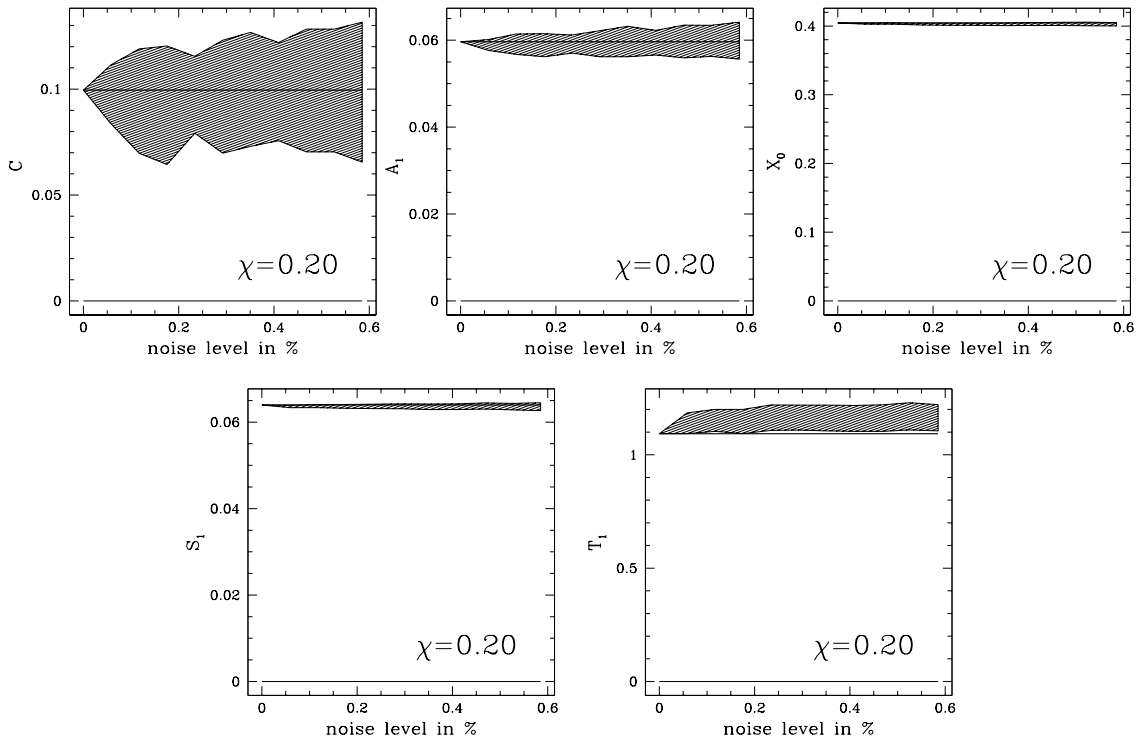

Figure 2.6: Some of the structure functions for the cluster depicted in Figure 2.5, when Poisson points are added. We show the true structure functions for this cluster (solid lines) and the 1σ fluctuations induced by the noise (shaded areas) vs. level of noise.

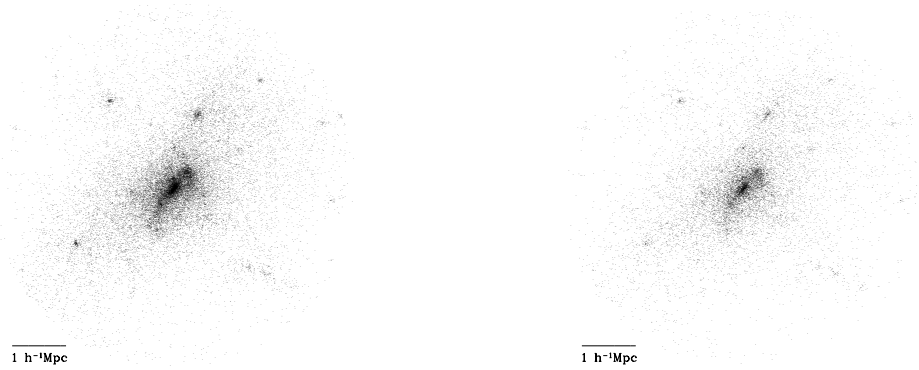

Figure 2.7: An illustration of the subsampling. On the left hand side the full cluster, on the right hand side only the subsampled points (50%). The cluster is one of the GIF clusters within the OCDM model at redshift $z = 0$.

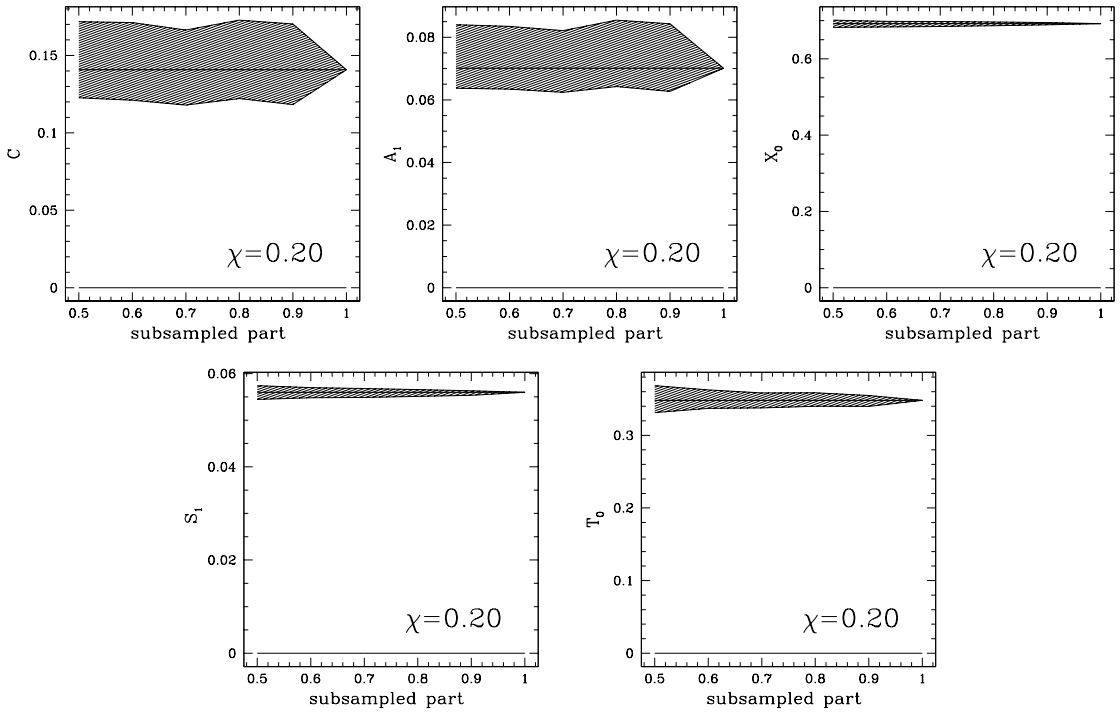

Figure 2.8: Some of the structure functions for subsampling. We took the cluster shown in Figure 2.7 and subsampled the points several times. We show the true value of the substructure functions for the cluster (solid line) together with the 1σ fluctuations from the subsampling. One recognizes that, on average, the subsampling does not affect the values of the structure functions. Furthermore, in many cases the fluctuations generated by the subsampling are rather small.

2.3.2 Model clusters

To understand the behavior of the structure functions better, we apply them to a number of model clusters. We simulate three–dimensional clusters and analyze two–dimensional projected images. We consider

1. the King model, an approximation of the isothermal sphere: for this model the points (representing, e.g., Dark Matter particles) follow the spherically symmetric three–dimensional profile:

$$n(\mathbf{r}) = \frac{n_0}{(1 + r^2/r_c^2)^{-3/2}} \quad ; \tag{2.3.20}$$

   we cut the distribution at a radius of $10h^{-1}$Mpc and consider a core radius $r_c = 0.07h^{-1}$Mpc (which is of the order or core radii of realistic clusters, see, e.g., Bahcall 1996);

2. an elliptically distorted King model,

$$n(\mathbf{r}) = \frac{n_0}{(1 + (r_1^2/a^2 + r_2^2/b^2 + r_3^2/c^2))^{-3/2}} \tag{2.3.21}$$

   viewed from one of the directions of the mayor axis; we choose $a = 0.07/\sqrt{0.7}$ and $b = 0.07 \times \sqrt{0.7}$, the value of c does not influence our results;

3. the superposition of two spherically symmetric King models, centered on different positions; for our example, we take two clumps with core radii $r_{c1} = 0.07h^{-1}$Mpc and $r_{c2} = 0.03h^{-1}$Mpc with equal weight and $1h^{-1}$Mpc apart from each other.

In each case, the clusters have of the order of $100,000$ particles each. We show examples in Figure 2.9. We average over 50 realizations for each model and show the averaged results together with the 1σ fluctuations in Figure 2.10, where we focus on the King model ($\chi = 0.05h^{-1}$Mpc). The results indicate that for small smoothing lengths the structure functions are dominated by small scale properties of the point distribution; the spherically symmetric reference clusters cannot be distinguished form the more realistic GIF clusters. For comparison, we also show the averaged results for about 40 images of GIF clusters. We conclude that smoothing scales smaller than $0.7h^{-1}$Mpc are not suited for our cluster investigations. However, at larger smoothing scales, the GIF clusters lie clearly outside the typical fluctuations of the model clusters. Often the structure functions are even one order of magnitude larger for the "real" GIF clusters than for the model clusters.
In Figure 2.11 the different models are compared using the structure functions. Whereas the King model shows mostly zero structure functions, the other two models clearly are distinguished by significant values of the shape parameter and the axes ratio of the tensors. The bimodal and the elliptical cluster can be distinguished by

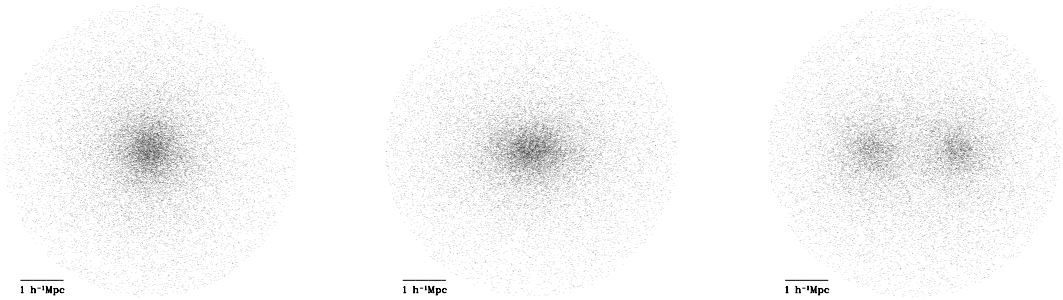

Figure 2.9: Realizations of different cluster models. Left panel: King model, middle panel: elliptically distorted King model, right panel: a bimodal cluster constructed by the superposition of two King models.

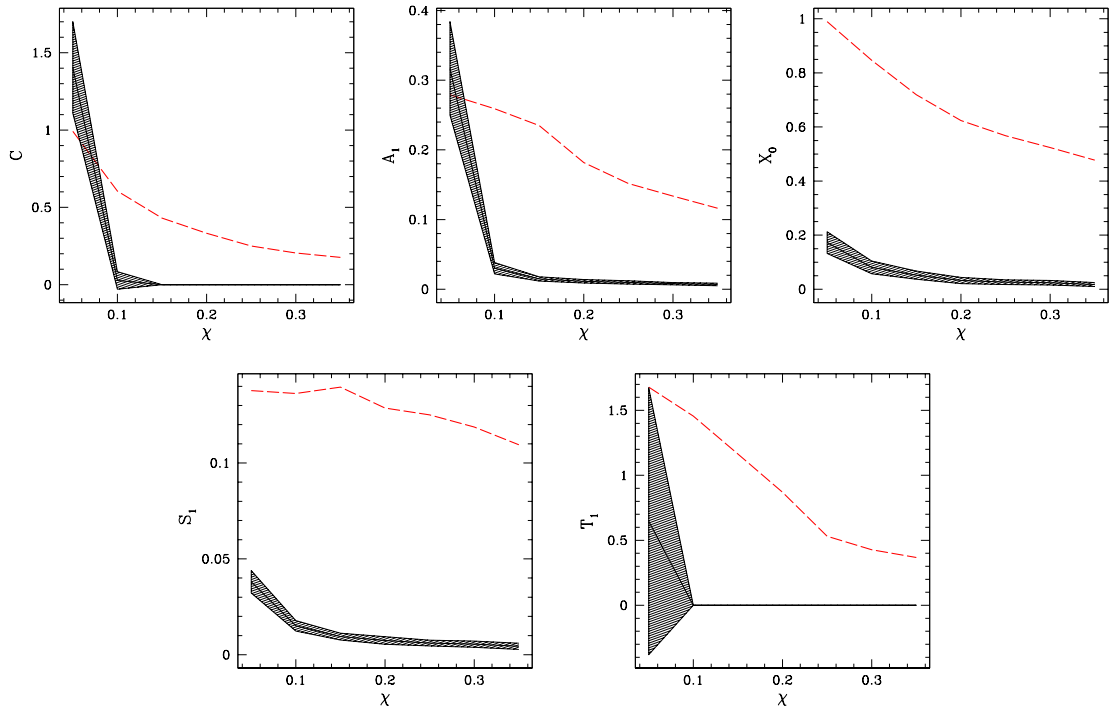

Figure 2.10: A comparison between an ensemble of 50 clusters following a King profile (solid line with 1σ bars as fluctuations), and a number of GIF clusters (dashed line, we took the τCDM model at $z = 0.06$ and had 14 clusters with 3 projections each, see Chapter 3 for further explanation).

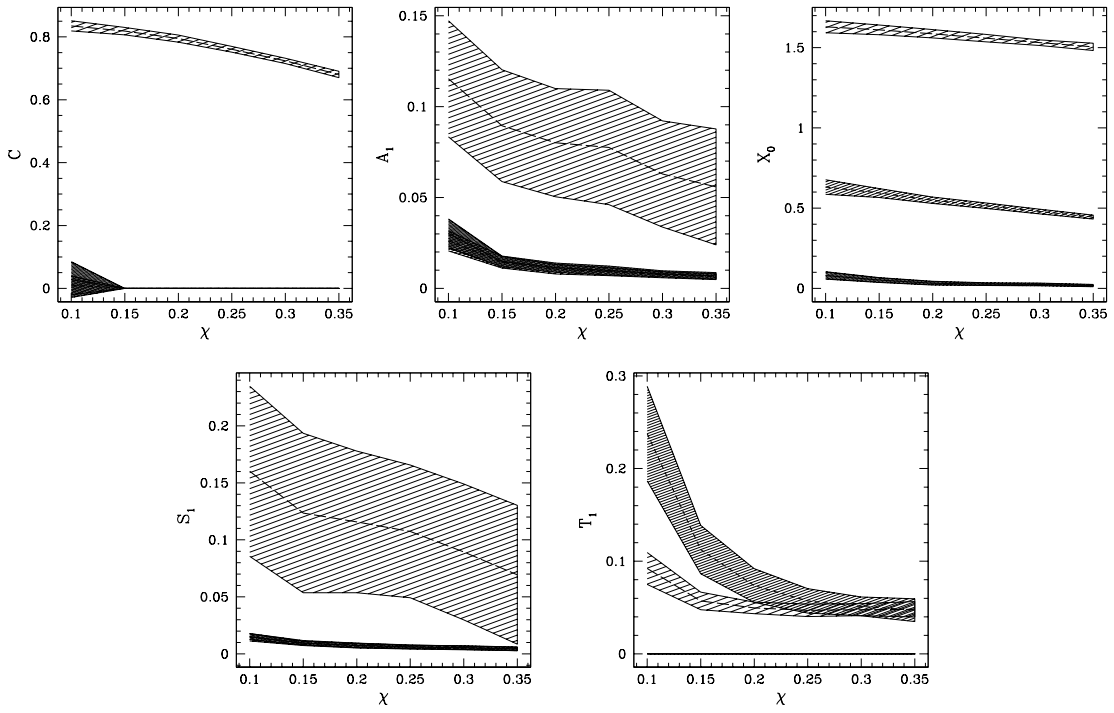

Figure 2.11: A comparison between different analytical models: King model: solid line/dark–shaded area, an elliptically distorted King model: short dashed line/medium–shaded area, a bimodal cluster: long dashed line/bright–shaded area. The values of the structure functions are plotted vs. the smoothing length.

means of the clumpiness, which shows the bimodality by a clumpiness close to one. Although all reference clusters are symmetric at least with respect to a symmetry axis, the bimodal clusters show an asymmetry parameter X_0 significantly different from zero, also the shift of morphological properties is relatively large. These values are only due to very high values of the density threshold: by chance one of both peaks is larger than the other one, thus for high density thresholds the centroids wander towards this peak; since this wandering is not uniform, the symmetry parameter becomes positive. But this is not undesirable, since the symmetry obviously is reduced for the bimodal cluster with respect to the King model.

2.4 Summary: a set of robust structure functions

To summarize the results of this chapter, we restrict ourselves to a number of *robust structure functions*. We select them from the above structure functions by the following requirements:

1. On average, the structure functions for the spherical King model should take values of at most 15% of the realistic clusters. Again, we consider smoothing lengths from $0.15h^{-1}$Mpc upward.

2. For a set of realistic clusters (GIF clusters, τCDM, $z = 0$) the structure functions should on average lie outside the 3σ range for spherically symmetric clusters following a King profile. We consider smoothing scales from $0.15h^{-1}$Mpc upward.

3. Under subsampling, the structure functions should be stable, i.e. the subsampling should not introduce a bias. We test this by requiring that the true value of a structure function lies within the 1σ bars from the subsampling. We take a fixed value of $\chi = 0.2h^{-1}$Mpc for the tests; for other values of χ, the effects of subsampling are usually smaller[9].

Note, that these tests are not universal since we probe only a subset of possible spherically symmetric clusters and single simulated clusters. Rather we interpret these tests as indicators for the robustness of the structure functions. In Figure 2.12 we illustrate the requirements.
The remaining robust structure functions are listed for the different morphotypes in Table 2.1. For the following applications they get simpler names which abbreviate the corresponding morphotypes and are listed in Table 2.1, too. – Some of the structure functions have a physical dimension; when we are interested only in the *relative* substructure of an object, then we divide them by a power of a typical scale to get dimensionless quantities. Such normalized quantities are denoted with an additional prime and marked in Table 2.1. – In the next chapter, we apply the robust structure functions to clusters of galaxies.

[9]For smoothing lengths larger than $0.2h^{-1}$Mpc, the parameter X_1 shows also a systematic shift. It thus has to be interpreted with caution.

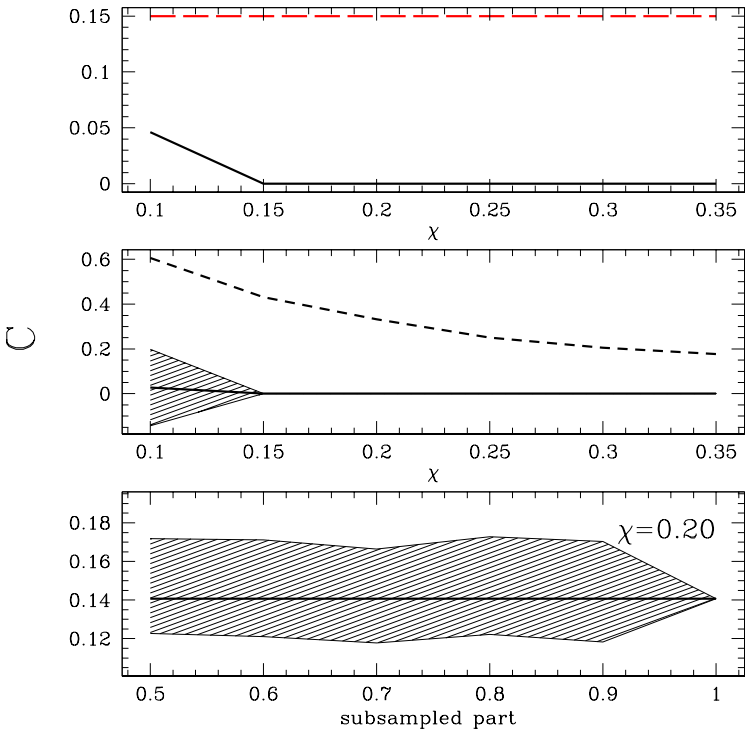

Figure 2.12: The robust structure functions are selected from the above structure functions by three requirements: Realistic clusters (here the GIF clusters within the τCDM model at $z = 0.06$) should on average have significantly larger absolute values of the structure functions than spherically symmetric clusters following a King model (top panel, see the main text for further explanation, the ratio of the mean structure functions for spherically symmetric clusters and GIF clusters: solid line; the criterion: long–dashed line); they should be clearly distinguishable from such clusters (middle panel, GIF clusters: short dashed line, model clusters: solid line), and a minimum stability under subsampling should be there (the real value of the structure function: solid line, 1σ fluctuations from 100 realizations of the subsampling: shaded area). Here we illustrate these criteria using the clumpiness, which matches the criteria without difficulty. For the other structure functions we proceed in the same manner.

Morphotype	Meaning of structure function	Name	Note
Clumpiness	Euler characteristic minus one	C	
Shape and Asymmetry	surface content of $\triangle(\mathbf{p}_i)$	A_0	dimension
	perimeter of $\triangle(\mathbf{p}_i)$	A_1	dimension
	axis ratio M^2	X_0	
	axis ratio $M_{0,1,2,0}$	X_1	
Shift	variation of $\mathbf{p}_0$	S_0	dimension
	variation of $\mathbf{p}_1$	S_1	dimension
	variation of $\mathbf{p}_2$	S_2	dimension
Twist	shift of ϕ_i	T_i	

Table 2.1: A summary of all robust structure functions for all morphotypes. The $\mathbf{p}_i$ are the curvature centroids, $\triangle(\mathbf{p}_i)$ denotes the triangle spanned by the curvature centroids.

Chapter 3

Applications: Galaxy clusters

3.1 Clusters of galaxies and their cosmological importance

Galaxy clusters play a key role in the understanding of the Universe since their discovery by Wolf (1906). For instance, the Dark Matter Problem was for the first time revealed within galaxy clusters (Zwicky 1933). Nowadays, clusters serve as tracers of the large scale structure (Postman 1998). However, not only their distribution in space, but also their inner properties are of cosmological interest since their intrinsic state depends on the cosmological background model. In this line of thought, clusters allow us to constrain the values of the cosmological parameters which govern the evolution of the Universe globally[1].

There are a variety of methods how to investigate clusters of galaxies. Since they consist of several components, namely galaxies, a hot gas, which emits thermal bremsstrahlung, and Dark Matter (DM for the sequel), they are visible both in the optical and in the X-rays (for a more observational review see Bahcall 1996, the X–ray–properties are discussed in Sarazin 1986, for the X-ray–properties of high–redshift clusters see, e.g., Schindler 1999; for non–thermal X–ray emission of clusters, e. g., Henriksen & Merrill 1993). The whole projected mass distribution of some clusters is accessible via gravitational lensing (Bartelmann 1998; Bartelmann & Schneider 1999).

Each of these methods provides us with images of clusters. A key point of under-

[1]The values of the cosmological parameters characterize the Friedmann models describing an ideal, homogeneous and isotropic fluid in the framework of General Relativity. They can be defined using the Friedmann equation for the cosmological scale factor $a(t)$:

$$\left(\frac{\frac{\mathrm{d}a}{\mathrm{d}t}}{a}\right)^2 = \frac{8\pi G}{3}\varrho + \frac{\Lambda}{3} - \frac{Kc^2}{a^2} \tag{3.1.1}$$

with the gravitational constant G, the density of the fluid ϱ, the cosmological constant Λ and the curvature K. c denotes the speed of light.

standing clusters is thus the *morphology* of galaxy clusters. Obviously, there are a number of questions which come immediately into one's mind when one looks at these pictures. How are the X–ray–, the optical and the DM–morphology related? What does the substructure in a cluster tell us about its dynamical state? What can we learn from the morphology of galaxy clusters about the structure of our Universe? – In this chapter, we quantify the cluster morphology using Minkowski functionals and try to answer a couple of the above questions investigating both simulated and observational clusters. Before this, however, we briefly review both theoretical predictions and observational results on the morphology of galaxy clusters.

The connection between the morphology of galaxy clusters and the cosmological background is based upon the following reasoning (Richstone et al. 1992): The formation and growth of cosmological structures depends significantly on the background cosmology. Especially, the value of Ω_m (the mass density in units of the critical density) plays a key role: if Ω_m is low, the cosmological expansion is fast, and structures will cease to attract matter. If we therefore live in a low–Ω_m–Universe, the clusters we observe at $z \sim 0$ should be relatively old. Clusters are thus a sort of cosmological clock. Using the spherical top–hat model, Richstone et al. (1992) could estimate the fraction of present–day clusters which had already been existing at a redshift z as function of the redshift.

On the other hand, clusters also show an inner dynamics which is thought of to lead to a virial equilibrium. If we assume, that the dynamical state of a cluster is mirrored by its morphology – a virialized cluster is commonly supposed to look more symmetric and substructure–poor than a young one –, one gets the so–called "cosmology–morphology" connection for galaxy clusters: in a low–Ω_m–universe, the clusters should look smoother and more relaxed than in high–Ω_m–universes – at least on average. The conclusions of Richstone et al. (1992) were strengthened by Bartelmann et al. (1993) who additionally used the Zel'dovich approximation (Zel'dovich 1970) to estimate the mean age of clusters in different background models. Evrard et al. (1993) investigated this connection for the first time using cosmological N–body simulations. So far, there was a variety of papers discussing this connection, e.g., Mohr et al. 1995b; Mohr et al. 1995a; Valdarnini et al. 1999.

However, there are some problems about the cosmology–morphology connection. From a theoretical perspective, the connection rests on an inconsistent description of cluster evolution: On the one hand, the clusters are modeled without substructure using the spherical collapse to get an estimate of the collapse time, on the other hand the substructure is treated as the only observable imprint of the cluster evolution and age (Böhringer, private communication). In particular, the overall evolution of the cluster and its inner dynamics are – unrealistically – thought of as independent[2]. Furthermore, it is not yet clear, what sort of equilibrium is possible within clusters

[2]The averaging formalism (Buchert & Ehlers 1997), which takes into account the backreaction from inhomogeneities on the overall evolution of a domain, is the correct framework to handle such problems; see (Kerscher et al. 2000) for an estimate of the abundance of collapsed domains.

and may serve as a dynamical attractor.
Oberservationally, one has to ask which data to analyze and to compare to simulations. Both X–ray data and optical data are available for clusters. Then, there are a number of substructure measures which quantify relevant aspects of the morphology. The challenge here is to reveal substructure within a system which is already of intrinsically inhomogeneous shape. Most of the morphological descriptors used so far were defined ad hoc and feature single aspects of substructure (Pinkney et al. 1996): mainly, one employed the centroid–shift (Mohr et al. 1993) and ellipticities (McMillian et al. 1989; Rhee & Latour 1991). They can be calculated using a spherical harmonics analysis of the surface brightness and its (volume)–moments. Further attempts are the Lee–Fitchett statistic (Lee 1979; Fitchett 1988) which focuses on bimodality, the Dressler–Shectman Δ, which mixes velocity and spatial information (Dressler & Shectman 1988), and the KMM–algorithm (Ashman et al. 1994) which describes the cluster as a superposition of a few Gaussian peaks. A spherical harmonics analysis of the estimated 2d gravitational potential (Buote & Tsai 1995; Valdarnini et al. 1999) and a wavelet analysis were used, too (Grebenev et al. 1995; Slezak et al. 1994; Gambera et al. 1997). Note, that many of these substructure measures are based implicitly on an assumed equilibrium shape of a galaxy cluster. Another problem is the question of how to identify clusters in the right way.
In this chapter, we investigate the morphology of clusters using the methods developed in Chapter 2. We use two sets of simulations, cluster simulations by Valdarnini et al. (1999) (V–clusters, for short) and the GIF simulations (Kauffmann et al. 1999) as well as real data (see below). From the V–clusters, we construct X-ray images, from all simulations we have DM–particles. For the GIF data (Kauffmann et al. 1999), additionally, we study galaxies which have been inserted into the simulated clusters using semianalytical models of galaxy formation by Kauffmann et al. (1999), compare also Diaferio et al. 1999.
From the physical point of view, main lines of thought are the connection between the background cosmology and the averaged cluster morphology. We compare the DM, the galaxy, and the gas distribution and ask, how the inner state of a cluster is related to its morphology.
After a short description of the simulations in Section 3.2, we investigate the cosmology–morphology connection for Dark Matter in Section 3.3 using the GIF clusters. Section 3.3 deals with the V–clusters focusing on X–ray images and fundamental plane relations (Section 3.4). In Section 3.5 we try to establish a cosmology–morphology connection for optical galaxy clusters using semianalytical models for the GIF data.

3.2 Cluster simulations and cluster images

Simulating galaxy clusters

The simulations we investigate rely on different simulation techniques and treat different cluster components. Whereas the GIF clusters are pure gravitational N–body simulations, the V–clusters additionally contain a gas component. The implementation of the cosmological background is different, too.
The "Hydra" code used for the GIF simulations is a parallelized version of an AP^{3}M code (Couchman et al. 1995; Pearce & Couchman 1997). One Dark Matter particle has a mass of $1.0 \times 10^{10} h^{-1} M_{solar}$ or $1.4 \times 10^{10} h^{-1} M_{solar}$ for low/high–Ω_m models, respectively[3].
The simulation technique used by Valdarnini et al. (1999) for the V–clusters consists of two steps: At first, a cosmological P^{3}M code is run. In a second step, the 40 most massive clusters found within this simulation at $z = 0$ are evolved a second time using a TREESPH–code with higher resolution. The basic idea of smoothed particle hydrodynamics (SPH) is to trace dynamical fields such as the density and velocity field with Lagrangian particles. This method is combined with a TREE–code, where the particles which are further away from the particle of interest are combined into more massive particles whose multipole moments replace the exact forces (Hernquist & Katz 1989). As output of these simulations, we get the positions of both the Dark Matter particles and the gas particles. To identify the clusters from the cosmological simulations, a friend of friend (FOF) algorithm was employed, the linking length was $0.2\Omega_m^{0.2}$ times the mean interparticle distance; for further details see (Valdarnini et al. 1999). Note that the clusters we obtain in this way are Lagrangian, i.e. we trace domains comoving with the fluid.

Cosmological background models and power spectra

The different cosmological models we investigate are summarized in Table 3.1, for further details compare the original papers describing the simulations (Bartelmann et al. 1998; Valdarnini et al. 1999). The basic differences consist in the values of the cosmological mass parameter Ω_m: we have several high–Ω_m and two low–Ω_m models. According to recent observations, which found a significant contribution of a cosmological constant using high–redshift Supernovae (Perlmutter et al. 1999), we consider even a flat low–Ω_m–universe.
Apart from the background cosmology, the power spectra expressing the initial conditions are important. For the simulations investigated here, mainly Cold Dark

[3]Particle–particle particle–mesh (P^{3}M) codes combine the advantages of both pure particle–particle codes, where the forces between the different particles are added up (good force resolution) and particle–mesh codes where the forces acting on a particle are calculated by integrating Poisson's equation on a grid (computational quickness). In P^{3}M codes the force on a particle divides into a part generated by the nearest neighbors and another part which accounts for the forces of the rest. AP^{3}M codes determine the scale separating these regimes adaptively respecting the local density.

name	model	Ω_m	Ω_Λ	Γ	h	L$\times h/Mpc$	σ_8
V	CDM	1.0	0.0		0.5	(200)	0.6
	CHDM	1.0	0.0		0.5	(200)	0.64
	ΛCDM	0.3	0.7		0.7	(200)	1.1
GIF	(SCDM)	1.0	0.0	0.50	0.5	85	
	τCDM	1.0	0.0	0.21	0.5	85	
	OCDM	0.3	0.0	0.21	0.7	141	
	(ΛCDM)	0.3	0.7	0.21	0.7	141	

Table 3.1: The model parameters of the simulations investigated here. For the V–clusters the boxsizes L of the simulation boxes are given in brackets since only the first step of the simulations uses these cosmological boxes. Comparing the models, we can distinguish between the effect of the power spectra (parametrized by the shift parameter Γ and the present day r.m.s fluctuations of the density contrast σ_8, compare White et al. 1993) and the cosmological parameters.

Matter (CDM) power spectra were used; within the CHDM model, however, Hot Dark Matter is present, too: both the GIF τCDM model and the Valdarnini CHDM model contain a massive neutrino (the τ neutrino). It shifts the power spectrum via the so–called shift parameter Γ in such a way that the power spectrum gets similar to power spectra of the low–Ω_m–Universes.

Cluster identification

The clusters within the GIF simulations were identified using a FOF algorithm, the linking length was 0.2 times the mean interparticle distance (Götz et al. 1998 show that an FOF algorithm with this linking length reproduces the Press–Schechter mass function quite well). We have both the pure FOF–clusters and larger infall regions around them.
For the V–clusters, cluster identification was already made after the first simulation step using a FOF algorithm.

Cluster images

The usual output of simulations consists of the positions of artificial simulation particles. Cluster images mimicking observations in a realistic manner thus have to be constructed by these particles. We investigate X–ray images and projected DM–images. Moreover, we look at galaxies within clusters in Section 3.5. Details of the

image construction are explained for each simulation separately together with the corresponding results. For the GIF clusters, overlapping clusters are not excluded, but investigated seperately.

3.3 The GIF clusters: the morphology–cosmology connection

What is the morphological evolution of galaxy clusters like and is it possible to distinguish between different cosmological background models using clusters? We start with the GIF clusters and study the OCDM and τCDM model as examples of a low–/high–Ω_m model, respectively. We first concentrate on the main component of galaxy clusters, the Dark Matter. Since the Dark Matter is invisible, real DM images are not possible. However, if we project the Dark Matter particles onto planes, we get an estimate of the projected mass density, which for real clusters can be reconstructed using gravitational lensing (Abdelsalam et al. 1998; Schneider et al. 2000). Thus, it is only useful to investigate two–dimensional images.

- Around the largest GIF clusters we got cluster regions of $15ah^{-1}$Mpc diameter, where a is the cosmological scale factor. Cylinders with fixed size in proper physical space (the radius is approximately $3.4h^{-1}$Mpc, the height approximately $6.8h^{-1}$Mpc) are cut out of the simulations. This mimicks observations which trace matter within a spherical window in a given range of distances. The particles are projected onto the bottom of the cylinder, the two–dimensional images are analyzed as follows: first the center of mass for the points within the image is constructed and a smaller window of $2.25h^{-1}$Mpc + 2χ size is centered at this point (if this smaller window does not fit within the original "observation", the image is discarded; χ denotes the scale for the smoothing to be applied later on). This smaller window consists of two parts, the inner disk of $2.25h^{-1}$Mpc width thought of as containing the real cluster and an annulus two times the smoothing length χ wide and allowing a sort of boundary correction. From now on only points within the smaller window enter our analysis. We determine a half–mass radius for the real cluster part and smooth the data. For the integration over the density thresholds, we take the maximum density at the edge of the cluster part as u_{min} in Equation 2.2.8. This guarantees that we do not use density thresholds where the estimated density may be affected by matter ouside the smaller window. Using an alternative account, we determine a background in the outer regions of the small window using similar methods as described in (Böhringer et al. 2000) and (Reiprich 1998). We do not subtract the background, but start our integration at two times this background density. This limit is usually lower than the maximum density at the cluster edge, especially when a large clump is falling onto the cluster and entering the window. On the other hand, we cannot ensure that

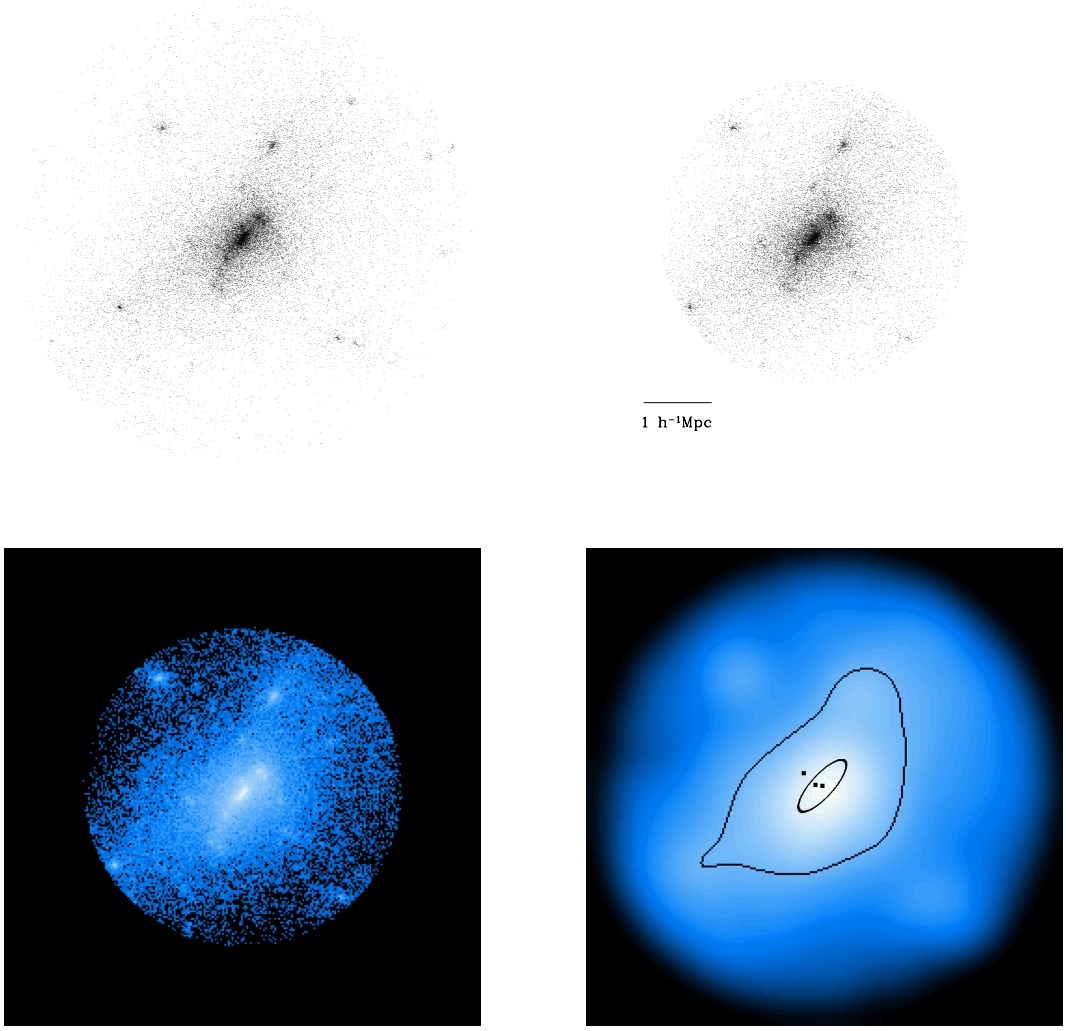

Figure 3.1: An illustration of our method. We first consider cylinders with a radius of about $3.4h^{-1}$Mpc radius and a height of about $6.8h^{-1}$Mpc (upper left panel). Then, a spherical image of $2.25h^{-1}\mathrm{Mpc} + 2\chi$ radius is positioned at the points (upper right panel for $\chi = 0$). The pure density field with 256×256 pixels can be seen in the lower left panel, in the lower right panel, we show the projected density field smoothed with a smoothing scale of $0.25h^{-1}$Mpc with one isodensity contour enclosing an excursion set with the corresponding curvature centroids. The inner ellipse illustrates the sizes of the eigenvalues and the eigendirections of the volume tensor for this excursion set.

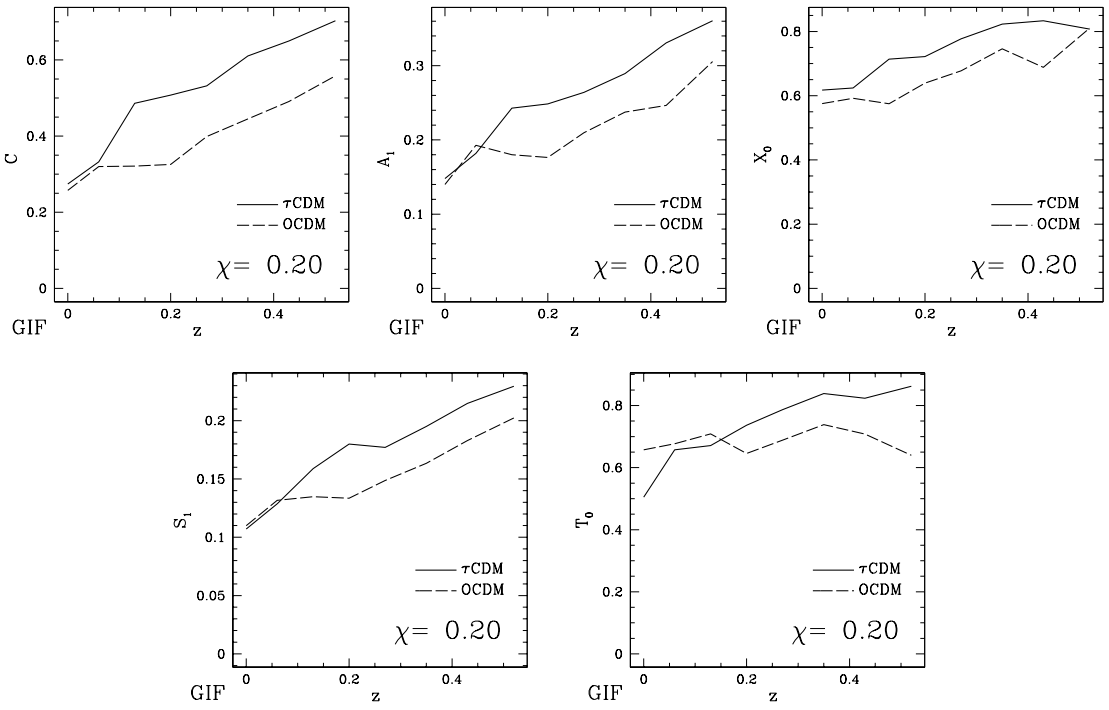

Figure 3.2: The averaged morphology evolution of the GIF clusters. We analyze the two–dimensional DM distribution in proper physical space as explained in the main text and apply the excursion set approach with a smoothing length of $0.2h^{-1}$Mpc. All structure functions show a clear evolution and distinguish well between the different cosmological models. τCDM: dashed line, OCDM: solid line.

we do not employ density thresholds which are significantly affected by matter outside the smaller window. Thus we mainly employ the first method. It is illustrated in Figure 3.1. We apply the excursion set approach and calculate the structure functions introduced in Section 2.2.

We have an ensemble of 14 clusters, per cluster we take three orthogonal projections as independent clusters to improve the statistics, thus we study 42 cluster images. The clusters correspond to each other throughout the models (i.e. stem from the same initial regions with the same initial random phases).
Results for the averaged morphological evolution can be seen in Figure 3.2 for a relatively small smoothing scale of $0.20h^{-1}$Mpc, and in Figure 3.3 for a larger smoothing length of $0.35h^{-1}$Mpc.
Already at first glance one sees a general evolution to more substructure–poor morphologies with decreasing redshift. Furthermore, as theoretically expected, the high–Ω model (τCDM) shows significantly less substructure then the low–Ω (OCDM)

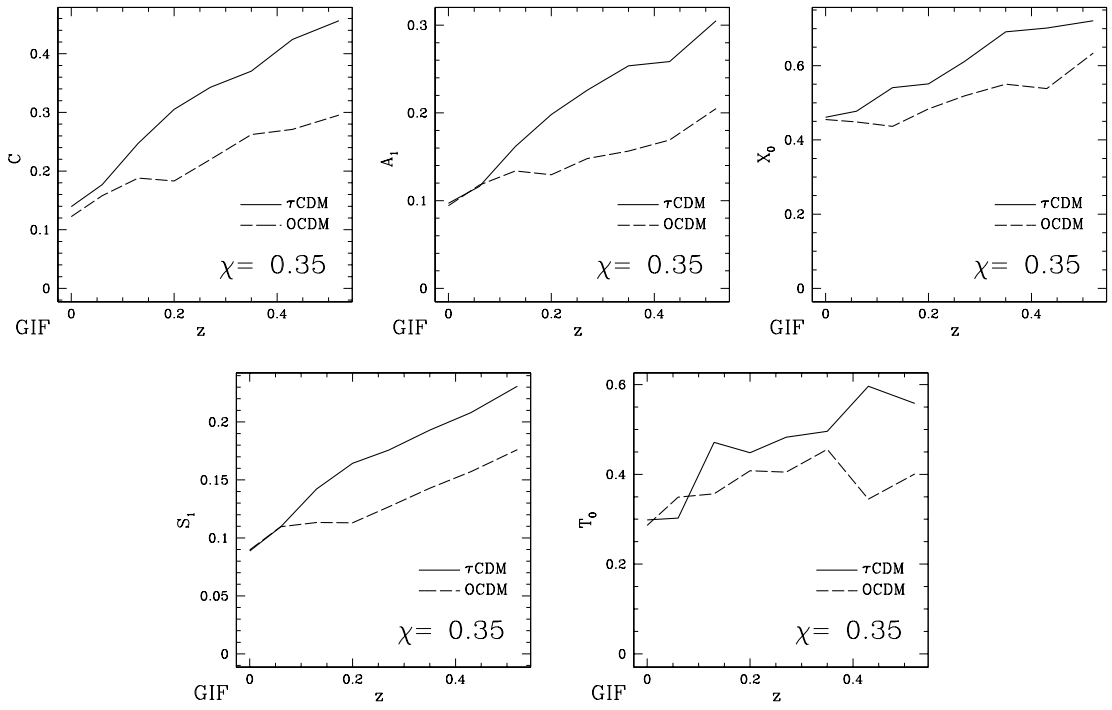

Figure 3.3: Again the morphological evolution of the GIF clusters, here at a smoothing of $0.35h^{-1}$Mpc.

model. Interestingly, this effect is almost vanishing for small redshifts, but becomes larger at higher redshifts. Thus, the *morphological evolution* is more important for the cosmology–morphology connection than the morphological state at redshift $z = 0$.
In more detail, the effect is visible in all structure functions. Especially the clumpiness and the asymmetry yield large differences. The effects are larger for larger smoothing lengths.
Although the general trend is clear and confirms the predictions of the theory, we still have to quantify the significance of such claims. In other words, so far we only investigated the averaged cluster morphology, but how are the other features of the distribution like? Since the clusters under investigation span a relatively wide mass range, large fluctuations are to be expected which do not mirror uncertainties within our structure functions, but rather reflect the variety of clusters "observed" within the simulations.
To investigate this we show the binned distributions in Figure 3.4. For a more quantitative analysis, we employ the Kolmogorov–Smirnov test (K–S test, henceforth). It compares two cumulative distributions $D_1(X) = p_1(x < X)$ and $D_2(X) = p_2(x < X)$

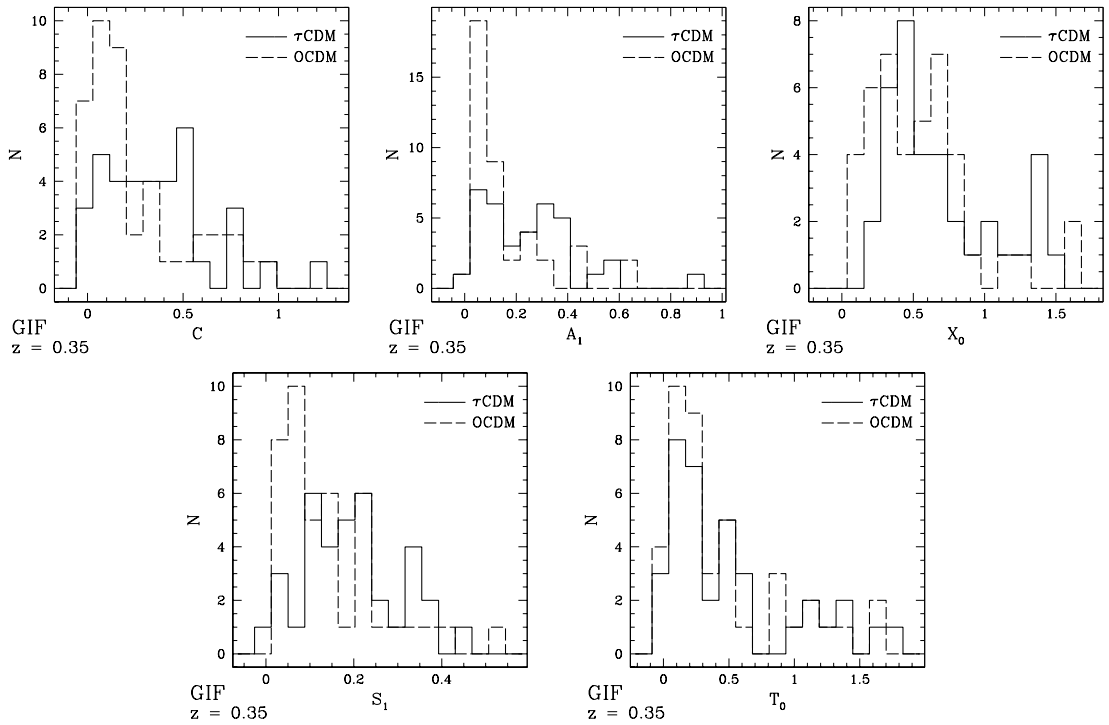

Figure 3.4: The distributions of the structure functions for the ensembles of GIF clusters ($z = 0.35$,the smoothing was $0.35h^{-1}$Mpc).

using the distance

$$d_{KS} = \max_{X \in \mathbb{R}} \{|D_1(X) - D_2(X)|\} \quad . \tag{3.3.2}$$

Advantageously, for every observed d_{KS} we can calculate the probability $p_{KS}(d_{KS})$ of the null hypothesis that this value of d_{KS} is obtained on the basis of two samples generated from the same random process. Thus the larger d_{KS} and therefore the smaller p_{KS} is, the more likely both data sets were generated by two different random processes. As usual in such cases, we require that $p(d_{KS}) < 0.05$ for significant claims.

In Figure 3.5 we plot the $p(d_{KS})$ vs. redshift for a smoothing of $0.35h^{-1}$Mpc. The values show that at higher redshifts, a significant distinction between the different cosmological models is possible with the clumpiness C, the asymmetry A_1 and the shift of morphological properties S_1. – If we start our integration of the structure functions in Equation (2.2.8) at two times the background density, the differences between the models seem to become larger for low redshifts in many cases.

The Dark Matter morphology thus discriminates effectively between different cosmological background models at least for higher redshifts, although the cluster sample is rather small.

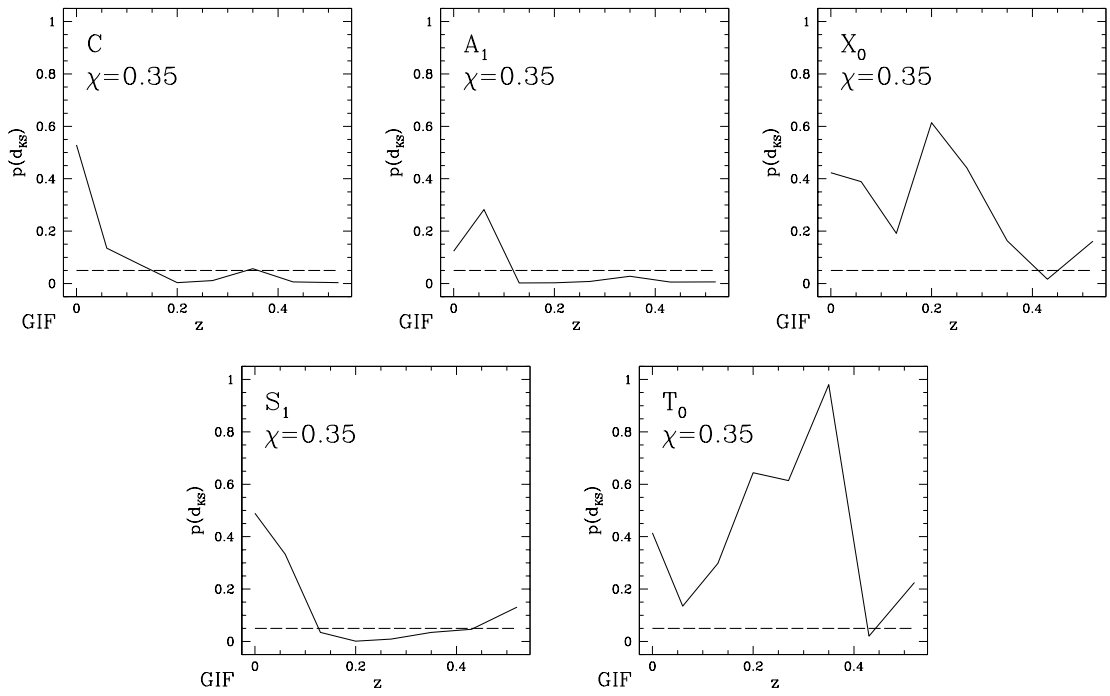

Figure 3.5: The results of a Kolmogorov–Smirnov test between the cosmological GIF models. We carry out a KS–test for each structure function and each redshift. The probability of the null hypothesis $p(d_{KS})$ is plotted vs. redshift. Only values of $p(d_{KS}) < 0.05$, as indicated by the dashed horizontal line, are supposed to indicate a significant discrimination between the different models.

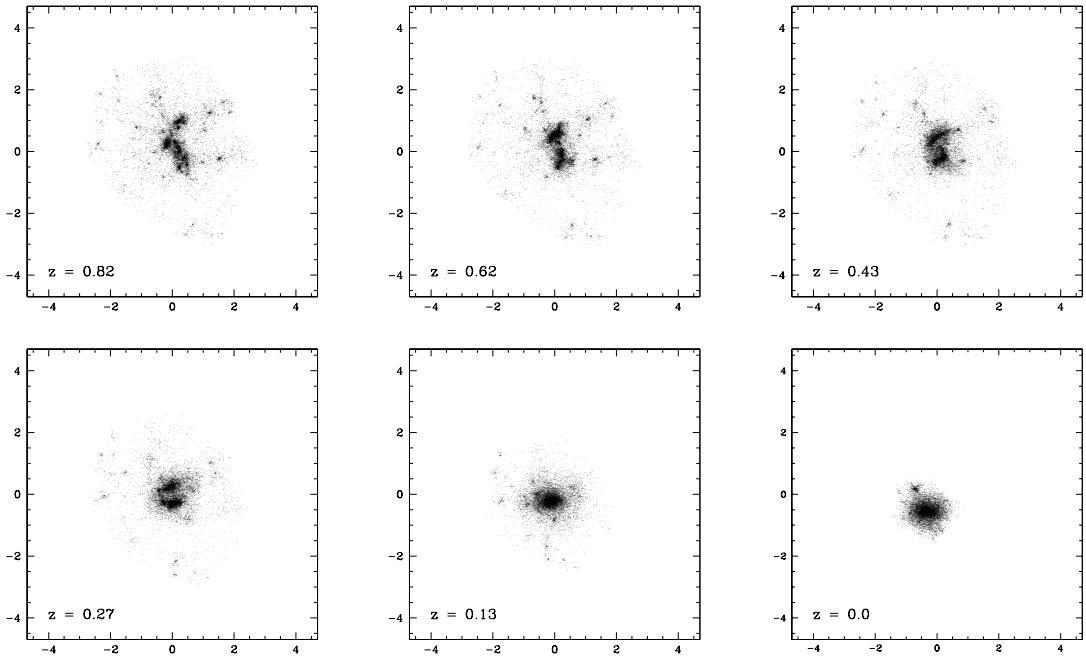

Figure 3.6: The dynamical evolution of one of the Lagrangian GIF clusters in proper physical coordinates (i.e. in units of h^{-1}Mpc) within the τCDM model.

Lagrangian clusters

From a theoretical point of view, it is also interesting to investigate the morphology of a domain comoving with the cosmological fluid. Of course, such results cannot be compared with observations. However, merger histories employed in numerical simulations are comparable to our methods, compare, e.g. (Evrard et al. 1993). We have an ensemble of 20 clusters for the τCDM and OCDM model, each; the clusters correspond to each other in terms of the initial conditions. The Lagrangian clusters consist of all particles found within the FOF clusters at $z = 0$ (see Section 3.2). Again, we take three orthogonal projections per cluster. For an illustration we show the evolution of a Lagrangian cluster in proper physical space within the τCDM model in Figure 3.6.
In this case, however, we have to compare clusters of different sizes. This is illustrated in Figure 3.7 where two two–dimensional estimates of the cluster scales averaged over all clusters are compared between the cosmological models. The first one relies on an estimation of a half–mass–radius, the second one is also sensitive to the outer cluster regions: we construct the two–dimensional convex hull of all cluster points and compute the length of its perimeter l. $l/2\pi$ serves as estimate of the cluster scale. As visible from Figure 3.7 one sees, that the OCDM clusters are on average

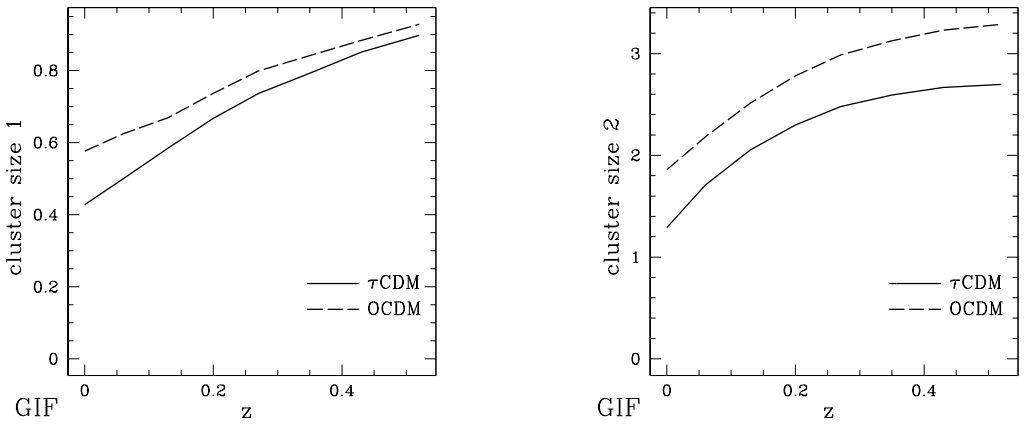

Figure 3.7: The evolution of the cluster size for the Lagrangian GIF clusters.

larger than the τCDM clusters. Possibly, this is an effect of the cluster identification. In Figure 3.8 one can see the morphological evolution. Although there is a general tendency to more relaxed clusters as above, the distinction between the cosmological models is either bad or even the other way round as expected. This is in part due to the different cluster sizes. Thus it is appropriate to scale the structure functions with dimensions to the typical scale of each individual cluster. From Figure 3.9 we see, that then the results point at least into the right direction.
Summarizing, one can state, that the DM evolution within the GIF–simulations confirms that the morphology of galaxy clusters can serve as a cosmological tool and discriminate between different cosmological models. Especially the morphological evolution is of interest. Lagrangian clusters are not effective in discriminating between different cosmological background models.

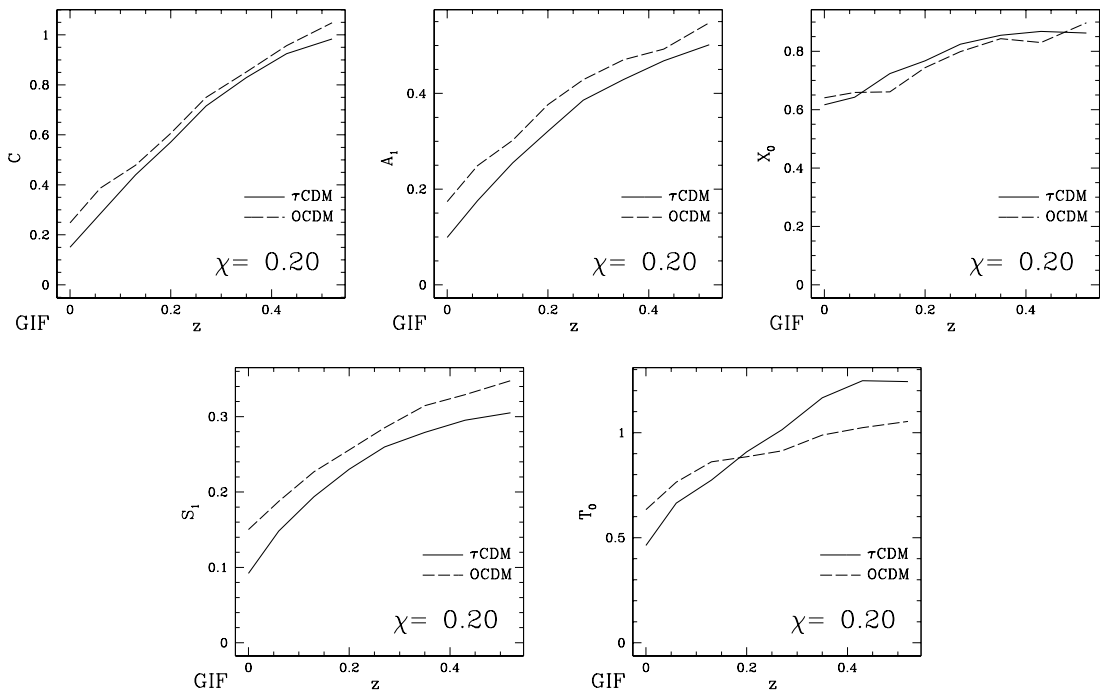

Figure 3.8: The morphological evolution of the Lagrangian GIF clusters, traced by the structure functions. The smoothing length was $0.20h^{-1}$Mpc. Only in part, the theoretical predictions of the cosmology–cosmology connection are confirmed. For larger smoothing scales, the results are even worse, and the τCDM clusters have even less substructure.

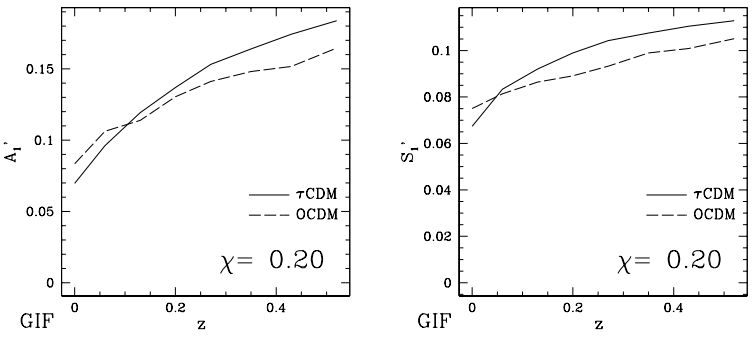

Figure 3.9: The morphological evolution of the Lagrangian GIF clusters, traced by the scaled structure functions

3.4 The morphology of X–ray clusters and fundamental plane relations

But does also the X–ray gas morphology allow claims on the cosmological background? And to what extent does it reflect the intrinsic dynamical state of a cluster? We investigate this and a couple of other questions using the V–clusters simulated by Valdarnini et al. (1999).
The images to be analyzed with the MVs are constructed as follows:

X–ray images Since bremsstrahlung is generated by a two–particle interaction, the X–ray emissivity is proportional to the square of the gas density:

$$\epsilon \propto \varrho_{gas}^2 T^{0.5} \quad ; \tag{3.4.3}$$

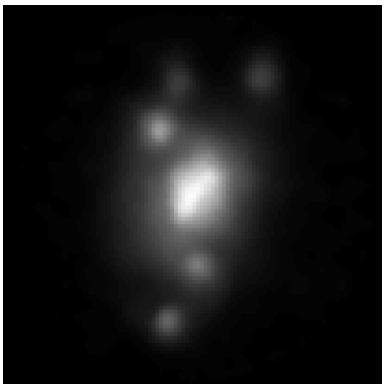

Figure 3.10: An X-ray cluster image for a V–cluster (cluster 05 in CDM at redshift $z \sim 0.05$). The cluster is sampled within a spherical window of $1.5h^{-1}$Mpc radius (logarithmic color scale).

where ϱ_{gas} denotes the gas density and T the temperature of the X–ray emitting gas. To generate X–ray images for the V–clusters, we assume that the influence of temperature variations within one cluster are negligible (which is relatively well fulfilled, since 1. the X–ray emissivity ϵ is only proportional to approximately $T^{0.5}$; 2. real temperature profiles of clusters are relatively flat at least in clusters with no cooling flow, for observational evidence see, e.g., Irwin & Bregman 2000; Irwin et al. 1999, for our clusters see Figures 3 and 4 in Valdarnini et al. 1999; and 3. the physical emissivity has to be convolved with the response function of the observational device. For the ROSAT satellite, the response–convolved emissivity is constant to a good approximation, see Tsai & Buote 1996). The SPH particles are sampled for an estimate of the gas density, then the three-dimensional squared density is projected onto a random plane. An absolute calibration of the surface brightness (and the detector count rate) is not necessary, since a constant factor drops out within the Minkowski analysis[4]. We get images of 101 times 101 pixels which are centered at the peak of the surface

[4]This calibration is only necessary if one wants to specify the cluster on the image (in our case the lower bound u_{min} of the integral in Equation 2.2.8) using, e.g., the signal–to noise ratio, which results from an interplay between the physical surface brightness and the detector performance. Here, however, we use a different approach to specify u_{min}. In general, the influence of u_{min} is relatively small since the X–ray images are sharply peaked, i.e. the integration in Equation (2.2.8) is to a large part due to the core of the cluster.

brightness[5]. The scale of the pixels always corresponds to physical $0.03h^{-1}$Mpc. To specify what the cluster is and to probe different regions of it, we put windows, namely spheres with radii r_w around the image centers and sample only pixels within this radius (this is in accordance with the cluster identification used by Abell 1958 in the optical). Using this method we do not presume a spherical shape of the cluster, rather we specify the observational window. Below, we test how large this window should be to allow significant results. We take only windows with radii r_w smaller than $1.5h^{-1}$Mpc in agreement with Cen (1997), who found that regions larger than $2h^{-1}$Mpc are too much affected by projection effects. To emphasize a certain scale of resolution we smooth the images and consider only pixels within the window after the smoothing. Thus, we do not apply boundary corrections accounting for the outer parts of the cluster. – To probe the DM morphology, we project the squared density of the DM, as if the DM behaved like the gas. Doing so we adopt the working hypothesis that the gas, which generates the X-ray luminosity, follows the DM. We can test this working hypothesis comparing to the gas morphology (see Subsection 3.4.5). For the structure functions, we choose u_{min} in Equation (2.2.8) as the maximum density value on the cluster edge (i.e. the sphere around the cluster), u_{max} is the maximum density found for this cluster (this procedure tends to underestimate the substructure of a cluster if a large subclump is on the border of the window, but this case occurs very seldom. Taking u_{min} as the minimum at the edge of the cluster gives comparable results).
We have 39 clusters for the CDM, 35 for the ΛCDM, and 37 for the CHDM model. Here we restrict ourselves to a smaller class of structure functions. We consider only the morphotypes clumpiness, shape, and asymmetry and shift of morphological properties. Within our applications, we take along C, A_0 and A_1, S_0, S_1 and S_2, as well as their dimensionless counterparts A_i' and S_j', for $i = 0, 1$ and $j = 0, 1, 2$. For the main applications, we mostly show C, A_1 and S_1. We investigate *cluster samples* which comprise all clusters for one model at one redshift. Unless otherwise stated, we take one random projection per cluster to construct the cluster samples.

3.4.1 The X–ray substructure of galaxy clusters

What should be established at the very outset is: what are the structure functions on average for the cosmological models like and is the cluster X–ray substructure able to reveal significant differences between the three cosmological models considered here (ΛCDM, CDM, CHDM)?
We show results where the X–ray–surface brightness was investigated with the Minkowski valuations after applying a small smoothing of $0.05h^{-1}$Mpc (Figure 3.11; without this small smoothing, the results are highly sensitive to noise, for comparison, Figure 3.12 shows results without a smoothing). Already at first glance, they confirm the theoretical expectations that the low–Ω_m model (i.e. the ΛCDM model)

[5]This was done by/in cooperation with R. Valdarnini.

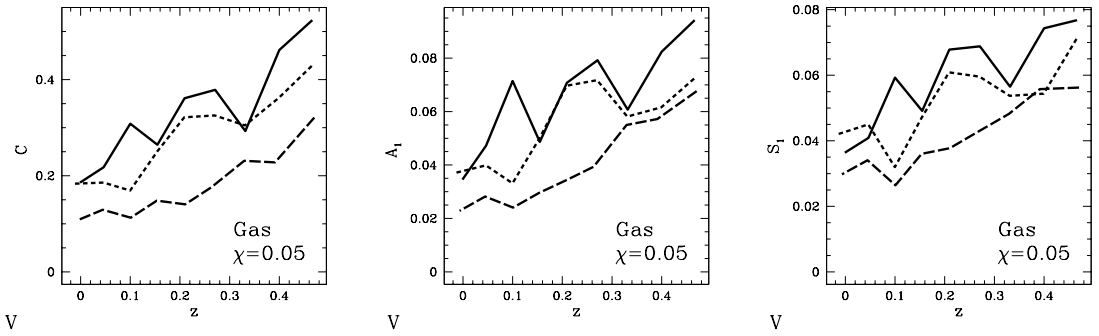

Figure 3.11: The averaged structure functions clumpiness C, asymmetry A_1, and morphological shift S_1 for the V–clusters using a sampling window of $1.4h^{-1}$Mpc scale for the gas distribution vs. redshift; to reduce the sensitivity to noise, a small smoothing of $0.05h^{-1}$Mpc was applied. CDM: solid line; ΛCDM: long dashed line; CHDM: short dashed line.

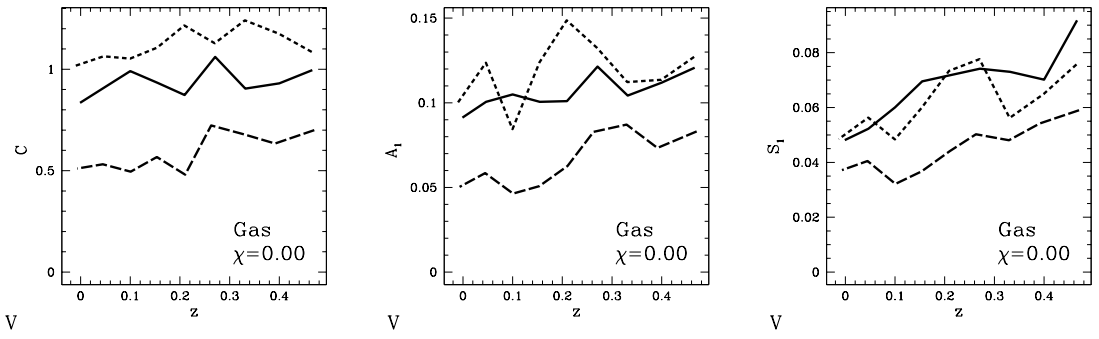

Figure 3.12: The averaged structure functions clumpiness, asymmetry, and morphological shift for the V–clusters using a sampling window of $1.4h^{-1}$Mpc for the gas distribution vs. redshift; here no smoothing was applied. CDM: solid line; ΛCDM: long dashed line; CHDM: short dashed line. Note, however, that without smoothing the structure functions are relatively sensitive to noise.

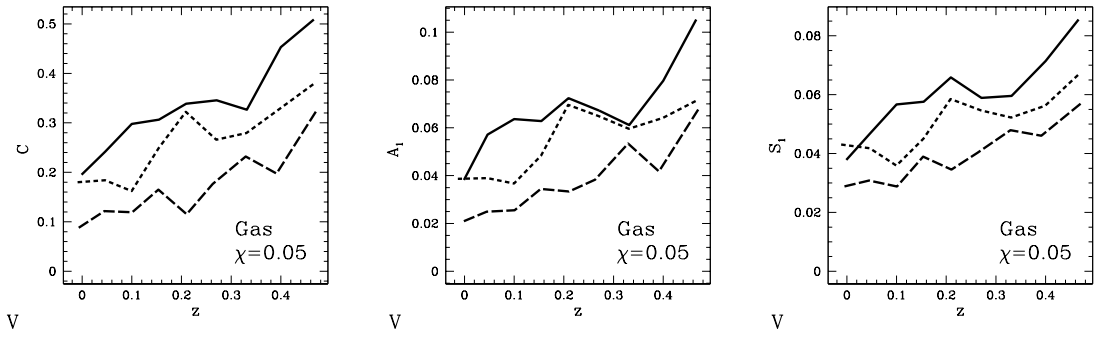

Figure 3.13: The same averaged substructure evolution for the clusters as in Figure 3.11, but now we artificially enlarged the cluster sample by taking three orthogonal projections per cluster as independent clusters. Thus, we had more than 100 clusters per model and redshift.

shows less substructure than the high–Ω_m models. This can be seen from the clumpiness, the symmetry and the shift parameter. These three structure functions also show an evolution to less substructure. – Of course, there is a large variance between the cluster morphologies within each model. In Figure 3.13 we took three orthogonal projections per cluster and took each projection as an individual cluster; thus, we artificially enlarged our cluster database. The results are in concordance with the previous ones. In Figure 3.14 we additionally show the 1σ bars for the ΛCDM model. Because of the variety of the clusters, the fluctuations are relatively large. However, sometimes, the high–Ω_m models are nearly one σ away from the ΛCDM model.
In Figure 3.15 we show the scaled symmetry parameter A_1' and the scaled morphological shift S_1'. These structure functions quantify the amount of substructure relative to the cluster size. The cluster scale is estimated via the half–light radius. But obviously, within our sample, the scaled quantities do not differ on average much from the unscaled ones. This means that the fluctuations of the cluster scales do not influence the substructure signal.
The DM morphology (i.e. the morphology the cluster would have, if the gas followed the DM) shows even stronger differences between the models (Figure 3.16). In particular, at $z = 0$ large differences are to be found.
A more effective comparison of the cosmological models can be obtained if we take into account the whole distribution of the structure functions. A quantitative comparison is based on the Kolmogorov–Smirnov test (see Subsection 3.3 for further explanation). In Table 3.2 we show the results of the K–S test. We compare each pair of models using the gas or the DM and our structure functions at $z = 0$. The results show that the CDM and the CHDM model exhibit comparable distributions of the structure functions whereas they significantly differ from the ΛCDM model, where $\Omega_m = 0.3$. Both the Gas and the DM are powerful for a comparison of cosmo-

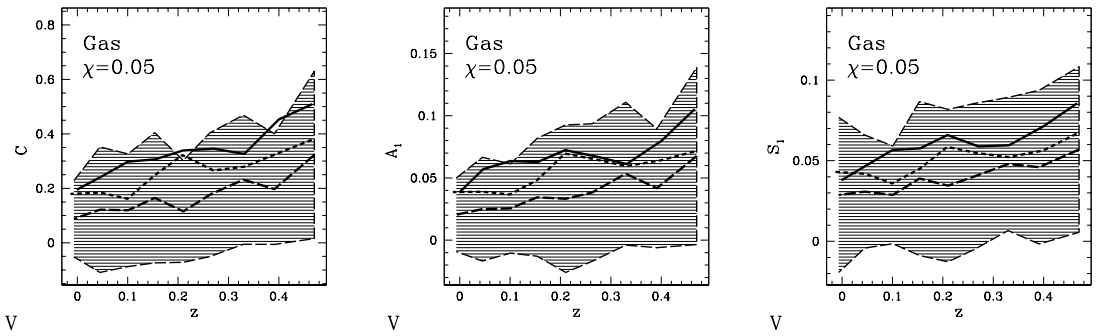

Figure 3.14: The same structure functions as in Figure 3.13, but now 1σ bars for the ΛCDM model (long dashed line) have been added.

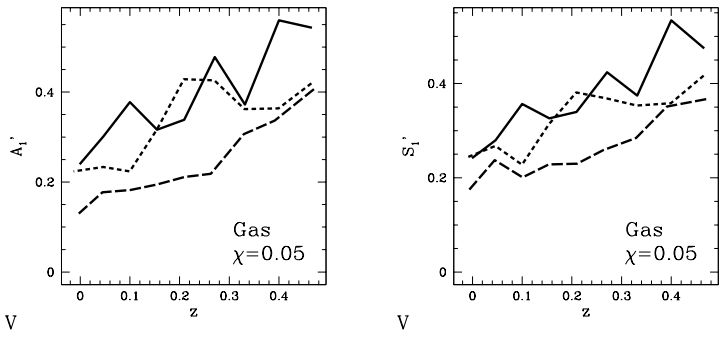

Figure 3.15: The scaled structure functions clumpiness A_1' and morphological shift S_1' for the V–clusters using a sampling window of $1.4h^{-1}$Mpc for the gas distribution vs. redshift; a small smoothing of $0.05h^{-1}$Mpc was applied. CDM: solid line; ΛCDM : long dashed line; CHDM: short dashed line.

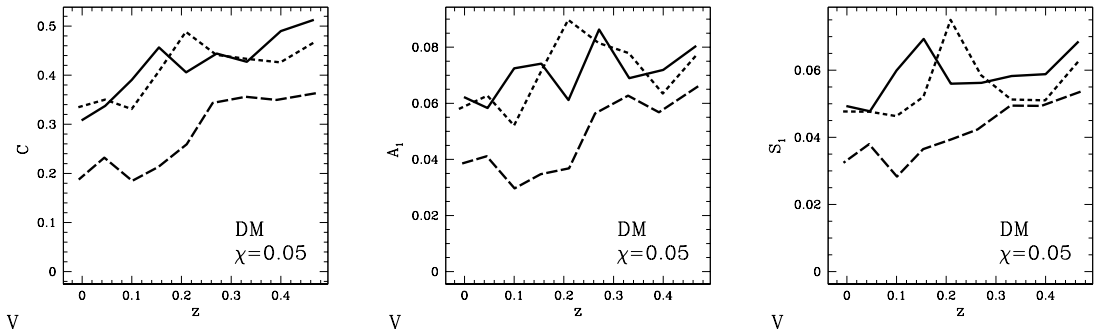

Figure 3.16: Now the DM distribution is investigated with the averaged clumpiness, asymmetry, and shift of morphological properties for the V–clusters using a sampling window of $1.2h^{-1}$Mpc; a small smoothing of $0.05h^{-1}$Mpc was applied.

Gas, $r_w = 1.40h^{-1}$Mpc, $z = 0$

$\chi = 0.05h^{-1}$Mpc	CDM - ΛCDM		CHDM - ΛCDM		CDM - CHDM	
	d_{KS}	p_{KS}	d_{KS}	p_{KS}	d_{KS}	p_{KS}
C	0.57	<0.05 %	0.56	<0.05 %	0.10	99.1 %
A_1	0.63	<0.05 %	0.66	<0.05 %	0.17	59.2 %
S_1	0.42	0.2 %	0.42	0.3 %	0.10	98.4 %

DM, $r_w = 1.40h^{-1}$Mpc, $z = 0$

$\chi = 0.05h^{-1}$Mpc	CDM - ΛCDM		CHDM - ΛCDM		CDM - CHDM	
	d_{KS}	p_{KS}	d_{KS}	p_{KS}	d_{KS}	p_{KS}
C	0.42	0.2 %	0.49	<0.05 %	0.10	98.4 %
A_1	0.44	0.1 %	0.63	<0.05 %	0.23	23.6 %
S_1	0.42	0.2 %	0.52	<0.05 %	0.23	25.5 %

Table 3.2: K–S test for the three cosmological models at $z = 0$. As the Kolmogorov–Smirnov distance d_{KS} and the corresponding probability p_{KS} show, the high–Ω_m-models can be distinguished from the low–Ω_m model very effectively, whereas the power spectra marking the difference between both high–Ω_m models do not lead to remarkable differences in the distributions of cluster morphology.

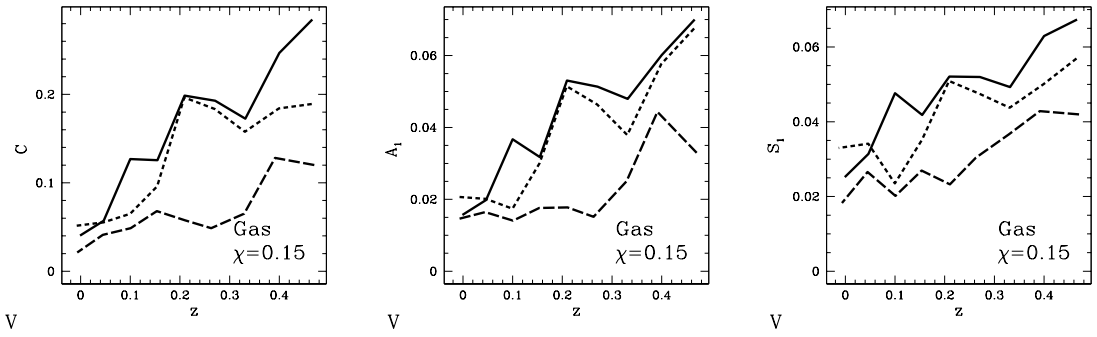

Figure 3.17: Clumpiness, asymmetry, and shift of morphological properties for the gas of the V–clusters using a sampling window of $1.4h^{-1}$Mpc, a larger smoothing of $0.15h^{-1}$Mpc was applied.

logical models, at least if only a small smoothing has been applied ($\chi = 0.05h^{-1}$Mpc). In this section we concentrate on the fertility of the gas and the DM for a distinction between cosmological models; the morphology bias for *single* clusters is investigated in Section 3.4.5.

To emphasize different resolutions and to enhance the discriminatory power of the method, we tentatively smooth the data with larger smoothing scales. As before, after having put the cluster into a window, we smooth with a Gaussian kernel and then cut out the part of the original sampling window. We show results for the morphological evolution within the different cosmological models for the gas in Figure 3.17 and for the DM in Figure 3.18.

One can see that during the dynamical evolution the differences between the background models are significant for larger smoothing lengths, too. We compare systematically how different smoothing scales perform in discriminating between the cosmological models in Figure 3.19 and carry out Kolmogorov–Smirnov tests for each pair of background models for a couple of smoothing scales χ using our structure functions. As results we show the Kolmogorov–Smirnov distance d_{KS} vs. smoothing scale χ for redshift $z \sim 0$. The results indicate that the discriminatory power of the clumpiness strongly depends on the smoothing length: for large smoothing scales, all subclumps are mixed together, and the differences between the clusters disappear. However, the other structure functions give still good results for higher smoothing lengths. The behavior of the other structure functions not shown in Figure 3.19 is similar; for the gas, the symmetry parameter A_0 seems to be even more discriminatory than A_1.

For the DM the situation is qualitatively similar as one can see from Figure 3.20. This figure also confirms, that the DM morphology sometimes shows stronger differences between the models than the gas morphology.

Using the same method, we systematically investigate in Figure 3.21, how the dis-

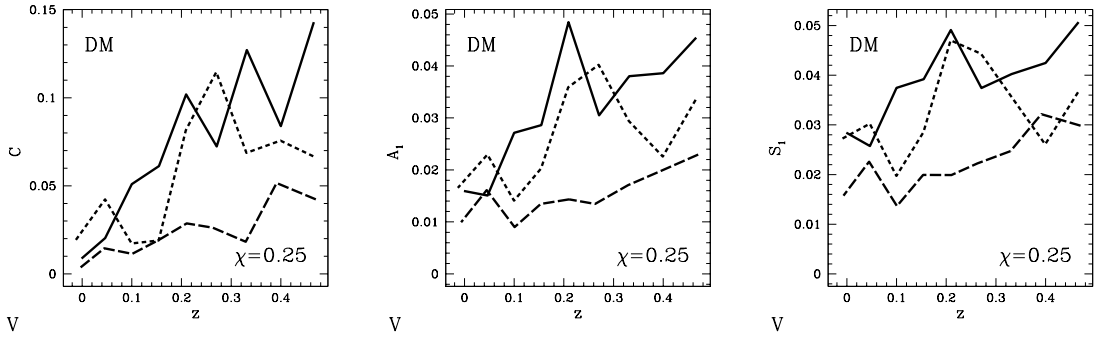

Figure 3.18: Clumpiness, asymmetry, and shift of morphological properties for the V–clusters using a sampling window of $1.4h^{-1}$Mpc; here the DM distribution was investigated using a larger smoothing length of $\chi = 0.25h^{-1}$Mpc.

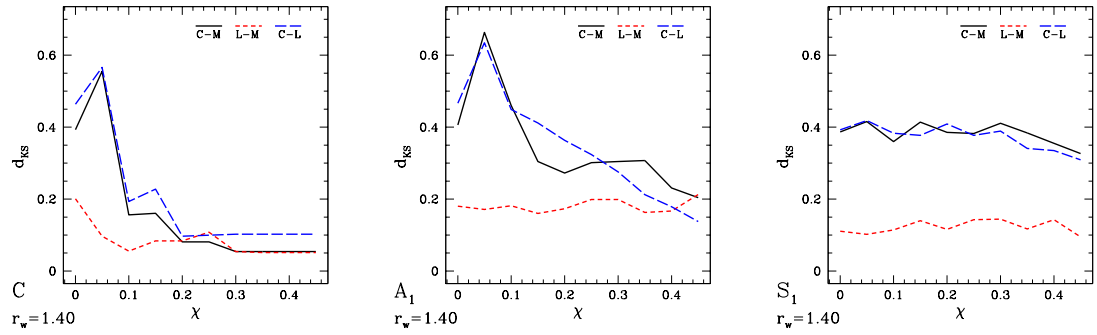

Figure 3.19: The effectiveness of the structure functions for different resolutions is analyzed using the Kolmogorov–Smirnov test. We plot the distance d_{KS} between the distributions of the substructure functions vs. smoothing length χ. We consider X–ray images from the V–simulations. CDM vs. ΛCDM: long dashed line; CDM vs. CHDM: solid line; ΛCDM vs. CHDM: short dashed line. One sees that larger windows enhance the discriminatory power of the structure functions for the clumpiness (left panel) and the asymmetry parameter (middle panel).

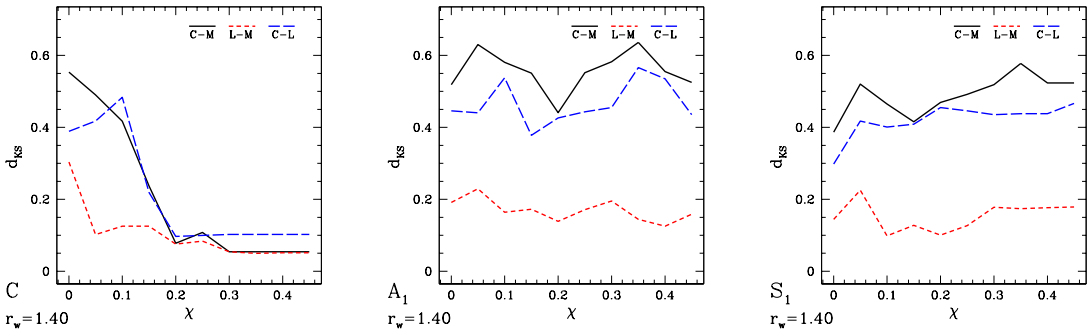

Figure 3.20: The effectiveness of the structure functions at different resolutions is analyzed systematically using the Kolmogorov–Smirnov test for the DM. We plot the distance d_{KS} between the distributions of the substructure functions vs. the smoothing length χ. CDM vs. ΛCDM: long dashed line; CDM vs. CHDM: solid line; ΛCDM vs. CHDM: short dashed line. The size of the window was $r_w = 1.4h^{-1}$Mpc.

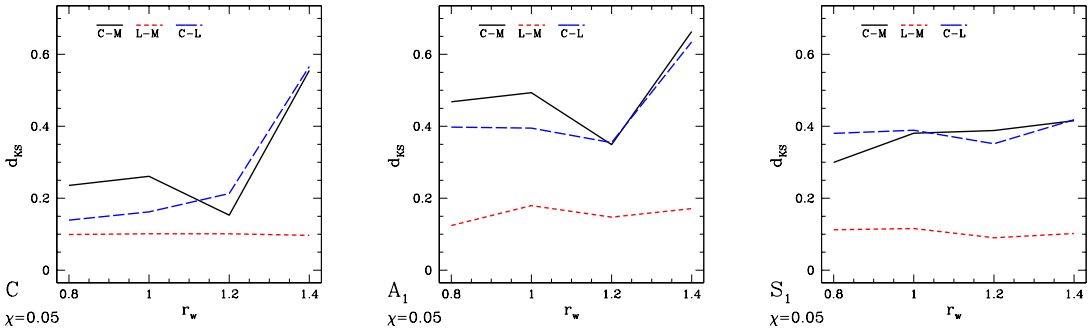

Figure 3.21: The effectiveness of the structure functions at different sizes of the window r_w is compared systematically using the Kolmogorov–Smirnov test. The Kolmogorov–Smirnov distance d_{KS} between the distributions of the substructure functions is plotted vs. r_w. We only consider the gas and a smoothing of $0.05h^{-1}$Mpc. CDM vs. ΛCDM: long dashed line; CDM vs. CHDM: solid line; ΛCDM vs. CHDM: short dashed line.

crimination between the cosmological models is influenced by the scale of the window r_w, i.e. which parts of the clusters allow for the strongest claims regarding the cosmological background. For the gas and a smoothing length of $0.05h^{-1}$Mpc, a large box is the best choice. From a physical point of view, this means that the outer cluster regions, where current infall is going on, are of most importance for cosmological purposes. It turns out that for higher smoothing lengths the influence of the box size is decreasing. For the DM the dependence on the window scale is weaker.

3.4.2 Relationships among the substructure functions

So far, the structure functions gave qualitatively comparable results for the mean morphological evolution. But how are the structure functions related to each other for single clusters? There is a technical and a physical interest about this question. Technically, it is important to know whether the structure functions feature independent aspects of substructure. From a physical point of view, one can ask whether the substructure functions are empirically related, and whether their relationships are different for the different cosmological models. We cannot answer these questions independently since the physical question presumes that the technical one in answered. Therefore, these questions have to be treated carefully. By their construction, the substructure functions feature different aspects of substructure. Tentatively, we carry out Kendall's test (a non–parametric correlation test) to probe their mutual relationships for the gas morphology[6].
For each sample (defined by one redshift and one model) we test each pair of structure functions evaluated at a fixed smoothing. Results can be seen from Figure 3.22 and 3.23; note, that a small smoothing length was employed. Figure 3.22 shows the correlations within the classes of substructure. In general, there a highly positive correlations between the structure functions. The two asymmetry parameters A_0 and A_1 are only badly connected, but this may be explained by the fact, that both parameters are sensitive to different classes of asymmetry: merely axial symmetric patterns are recognized as asymmetric by A_1, but as symmetric by A_0. However, the correlations between the shift parameters S_0 and S_1 are very strong; S_2 is less correlated with the other two shift parameters. The unscaled structure functions and their corresponding scaled counterparts are again well connected, this is, however, not true for S_2 (not shown here). Figure 3.23 shows that there are also relatively strong correlations between the structure functions of different morphotypes, some-

[6]Given data points $\{x_i, y_i\}_{i=1}^N$, Kendall's τ (Kendall 1938) tests in a robust and nonparametrical way to what extent a positive or negative correlation among the data points exists. It relies basically on comparing the number of all concordant ($\mathrm{sig}(y_i - y_j) = \mathrm{sig}(x_i - x_j)$) and discordant ($\mathrm{sig}(y_i - y_j) = -\mathrm{sig}(x_i - x_j)$) pairs of data points (see also Press et al. 1987). The absolute value of τ quantifies the strength of the correlations, the sign tells us whether the correlations are positive or negative. The probability of the null hypothesis $p(\tau)$, that a given value of τ is generated by purely uncorrelated random points can be estimated as a function of N. Usually only τs with $p(\tau) < 0.05$ are supposed to indicate significant correlations.

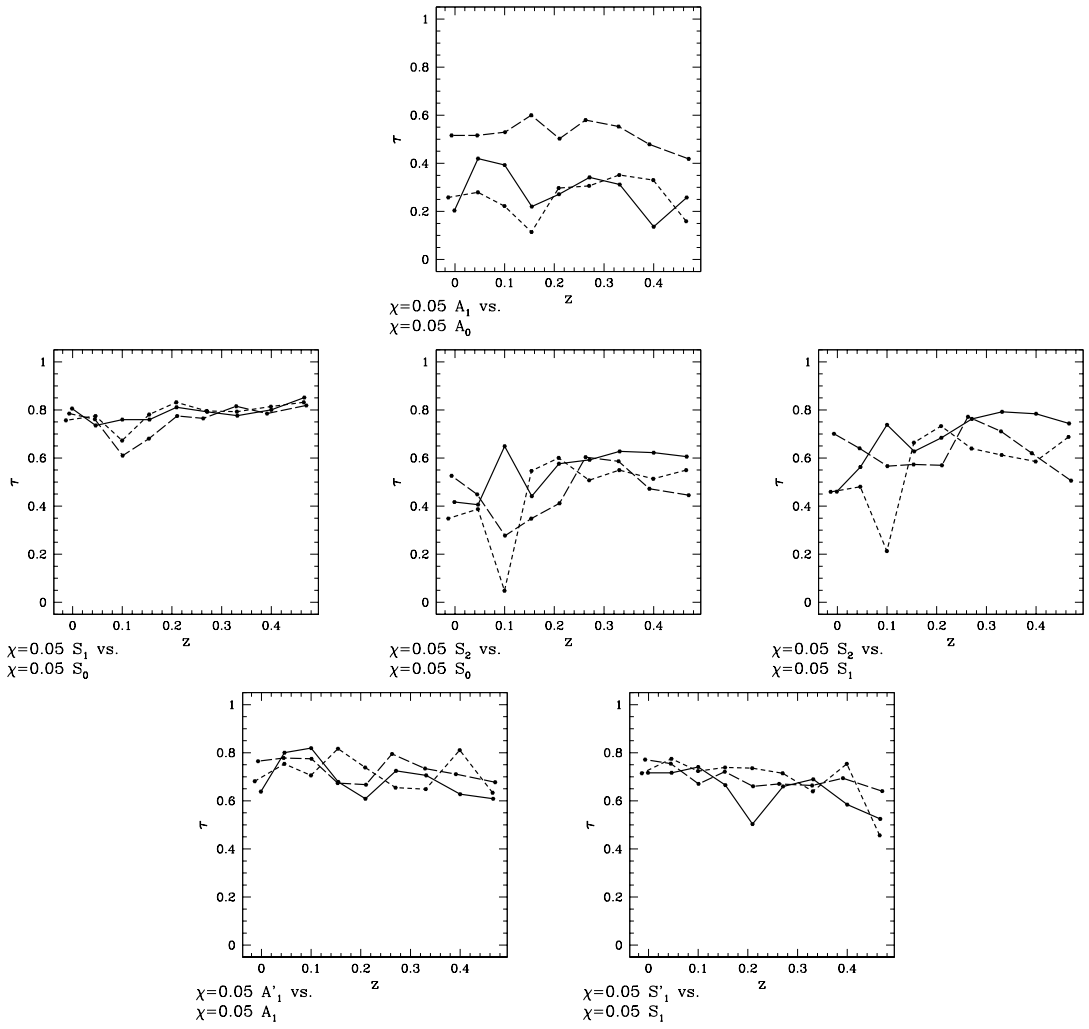

Figure 3.22: A systematic correlation analysis between different structure functions. For each cosmological model (CDM: solid line; ΛCDM: long dashed line; CHDM: short dashed line) and each redshift, we consider a pair of structure functions and calculate Kendall's τ. It is shown vs. redshift. Here we concentrate on correlations within each class of substructure. In the upper row, we look at the two symmetry parameters A_0 and A_1, in the middle row, the three shift parameters S_0, S_1 and S_2 are compared. In the row at the bottom we compare the A_1 and its scaled counterpart A_1' as well as S_1 and S_1'.

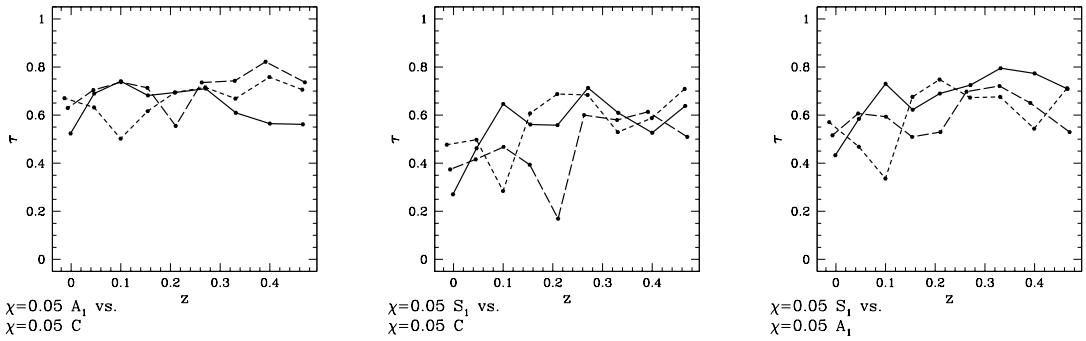

Figure 3.23: Kendall's τ for the different structure functions as a function of the redshift. CDM: solid line; ΛCDM: long dashed line; CHDM: short dashed line. Here we concentrate on correlations between different types of substructure.

times they are even stronger than the correlations within one morphotype. It is, however, not possible to answer the question, whether this is due to our sample (i.e. mirrors physical properties) or to the definitions of the substructure functions. We conclude, however, from these results that S_2, the shift of the curvature centroid $\mathbf{p}_2$, is a special measure. It is comparably weakly correlated to the other two shift parameters, but relatively well to the clumpiness C; it mixes thus the connectivity and the shift of morphology. Indeed, $\mathbf{p}_2$ jumps if subclumps fall out of the excursion sets. These subclumps generate a large C and a large S_2. – Mostly, the cosmological models are comparable regarding the correlations of the structure functions. Furthermore, there is a tendency to better correlations for higher smoothing lengths.
Altogether, the relationships between the different models let us understand why all structure functions show a similar signal in discriminating the different models (*cf.* Section 3.4.1). However, individually, the clusters should be investigated using all kinds of structure functions.
A similar test, where we compare single clusters whose substructure has been quantified at different smoothing lengths, shows that with exception of the clumpiness and the asymmetry A_0 the structure functions are well correlated for different smoothing scales.

3.4.3 Projection effects

"Projection effect" is an ambiguous word in the field of cluster investigations: on the one hand the fore– and background effects which come along with the projection are subsumed under this word. These effects were investigated by Cen (1997) in detail. For X-ray images they turn out to be rather small since the X–ray emissivity is proportional to ϱ_{gas}^2; thus, mainly the very peaks of the gas density contribute to the X–ray images. On the other hand, there is the geometrical question of how

$\chi = 0.05h^{-1}\mathrm{Mpc}, \quad r_w = 1.40h^{-1}\mathrm{Mpc}$

	CDM		ΛCDM		CHDM	
	Gas	DM	Gas	DM	Gas	DM
C	0.639	0.331	-	-	-	0.371
A_0	0.812	0.732	0.960	0.933	0.929	0.626
A_1	0.370	0.333	0.331	0.321	0.436	0.376
S_0	0.303	0.279	0.293	0.284	0.337	0.345
S_1	0.295	0.268	0.317	0.269	0.329	0.355
S_2	0.371	0.292	0.455	0.387	0.393	0.294
A_0'	0.808	0.697	0.973	0.976	0.919	0.629
A_1'	0.341	0.269	0.334	0.342	0.428	0.308
S_0'	0.261	0.211	0.267	0.289	0.298	0.297
S_1'	0.256	0.210	0.281	0.270	0.302	0.298
S_2'	0.371	0.268	0.454	0.433	0.392	0.278

Table 3.3: The averaged relative fluctuations of the structure functions for the gas and the DM at $z \sim 0$.

certain substructures in three dimensions are reflected in two–dimensional projections. In this section we adopt the second point of view and ask for the variance of cluster substructure for a single cluster, if we "observe" it from different directions neglecting back–and foregrounds.

For each cluster the X-ray maps are calculated for three orthogonal projections (here onto the surfaces of the simulation boxes), the structure functions are calculated and averaged. The averages over three projections are denoted by $\overline{\mathrm{Y}}$, the fluctuations by $\Delta\mathrm{Y}$ for each structure function Y. They are shown together in Figure 3.24. The relative fluctuations are averaged over each cluster ensemble (one model at one redshift) to give $\left\langle \Delta\mathrm{Y}/\overline{\mathrm{Y}} \right\rangle$ and listed in Table 3.3 (insofar as they can be calculated, i.e. insofar as none of the cluster averaged structure functions equals zero). The variances are relatively large, especially for the clumpiness and the asymmetry A_0. It is clear that the subclumps are projected onto each other. Since the gas distribution is smoother, less subclumps exist, and the relative fluctuations are larger. The fluctuations of the DM structure functions are slightly smaller than for the gas.

Altogether, we see that for individual clusters one projected image is not enough for a reliable estimate of their substructure. Only the shift of morphological properties is relatively constant for different projections. This result, however, refers to individual clusters, for larger cluster databases these fluctuations do not matter.

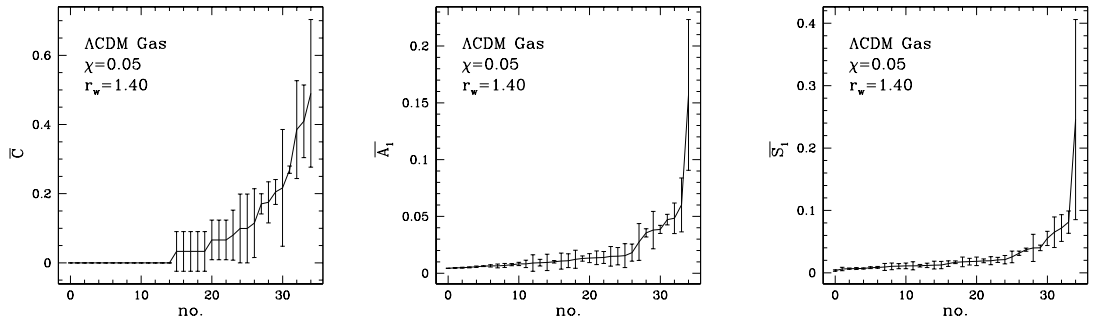

Figure 3.24: The averaged structure functions for the ΛCDM model (gas) for no smoothing and a window of $r_w = 1.4h^{-1}$Mpc. The clusters are ordered according to the mean structure functions. The variances – we show 1σ bars – were estimated using three orthogonal projections.

3.4.4 Fundamental plane relations and the substructure of galaxy clusters

So far, we empirically investigated the morphology of galaxy clusters conducted by the assumption that the inner cluster state is reflected by its substructure. Now we address the validity of this assumption.

Since a couple of years, fundamental plane relations have been of interest in the field of cluster research. Fundamental plane relations were originally found for elliptical galaxies (see, e.g., Bender et al. 1992) and denote the fact that elliptical galaxies populate a plane in a three–dimensional space of global galaxy parameters. This plane is usually interpreted in terms of a virial equilibrium (Chandrasekhar & Lee 1968).

Even clusters of galaxies lie on a plane in a number of observational phase spaces of global cluster parameters (often referred to as "threespaces"; henceforth we speak of "parameter spaces"). This was found by Schaeffer et al. (1993); Adami et al. (1998b) in the optical, and by Annis (1994); Fritsch & Buchert (1999); Fujita & Takahara (1999) for X–ray clusters. The three global cluster parameters indirectly refer to the cluster's mass, its scale, and its velocity dispersion or X–ray temperature as an estimate of the kinetic energy[7].

As in the case of the elliptical galaxies, the fundamental plane (FP, for short) for clusters was interpreted in terms of a virial equilibrium. However, the straightforward application of the tensor virial theorem (Chandrasekhar & Lee 1968) to galaxy clusters suffers from a number of systematic problems (Fritsch & Buchert 1999).

[7]More precisely, the global parameter space is spanned by logarithmic variables like the logarithm of the cluster mass in typical units. A plane within this space corresponds to a powerlaw constraint for the physical variables.

Since the FP was defined purely in terms of observational parameters, its physical origin was not clear, too. Fritsch & Buchert (1999) (see also Fritsch 1996) gave clues in showing that the distance from the fundamental plane within the global parameter space and the substructure of a galaxy cluster are correlated (although very weakly) using the COSMOS/APM data and the ROSAT data[8]. Relating substructure to the inner dynamical state of galaxy clusters, their results do not only confirm the physical origin of the FP, but also provide a "missing link" in the cosmology–morphology connection. – In this section, we look for fundamental planes in cluster simulations and try to relate them to our substructure measures.

For the fundamental plane relations, we concentrate on real parameters and do not care about questions like how the cluster mass can be estimated using real observations. We focus on the following cluster parameters: the mass of the core (or "virial mass"), the emission–weighted temperature T, the X-ray luminosity L_X, the scale of the cluster r_h, and the velocity dispersion of all cluster particles, σ_v. Tentatively we investigate the following three parameter spaces and thus probe three possible planes[9]:

$$\begin{aligned} &\text{1. fundamental plane} \\ &\log\left(M_{vir}/(10^{15}M_\odot h^{-1})\right) + \beta_1^1 \log\left(r_h/(100h^{-1}\mathrm{kpc})\right) \\ &\qquad + \beta_1^2 \log\left(T/(10^7 K)\right) = \beta_1^3 \quad , \end{aligned} \tag{3.4.4}$$

$$\begin{aligned} &\text{2. fundamental plane} \\ &\log\left(M_{vir}/(10^{15}M_\odot h^{-1})\right) + \beta_2^1 \log\left(r_h/(100h^{-1}\mathrm{kpc})\right) \\ &\qquad + \beta_2^2 \log\left(L_X/(10^{43}\mathrm{ergs}^{-1}h^{-2})\right) = \beta_2^3 \quad , \end{aligned} \tag{3.4.5}$$

$$\begin{aligned} &\text{3. fundamental plane} \\ &\log\left(M_{vir}/(10^{15}M_\odot h^{-1})\right) + \beta_3^1 \log\left(r_h/(100h^{-1}\mathrm{kpc})\right) \\ &\qquad + \beta_3^2 \log\left(\sigma_v/(10^2\mathrm{km\ s}^{-1})\right) = \beta_3^3 \quad . \end{aligned} \tag{3.4.6}$$

The cluster parameters defining the parameter spaces are estimated from the simulations as follows: The mass M_{vir} is the mass within the virial radius: $M_{vir} = \frac{4\pi}{3}\Delta_c \rho_b r_{vir}^3$, where r_{vir} is determined from the three–dimensional matter distribution and encloses the mass $M(r_{vir}) = 4\pi \int_0^{r_{vir}} \mathrm{d}r r^2 \varrho(r) = \frac{4\pi}{3}\varrho_c \Delta_c r_{vir}^3$; here $\Delta_c \simeq 178 \cdot \Omega_m^{-0.45}$ is a conventional value from the spherical collapse model[10], and ϱ_c denotes the critical density. r_h is the three–dimensional half–mass radius. T denotes

[8] As substructure measures they employed variations of the ellipticity, the centroid and the orientation angle of a number of ellipses fitted to the X–ray cluster data at different scales.

[9] The velocity dispersion is a mass–weighted statistics, the computations of the global parameters were made in cooperation with/by R. Valdarnini.

[10] For the spherical collapse in an Einstein–de Sitter background model, the overdensity of the perturbation at collapse time is approximately 180 (Coles & Lucchin 1994).

$z \sim 0$	CDM - ΛCDM		CDM - CHDM		CHDM - ΛCDM	
	d_{KS}	p_{KS}	d_{KS}	p_{KS}	d_{KS}	p_{KS}
M_{vir}	0.185	0.512	0.237	0.205	0.336	0.026
r_h	0.286	0.079	0.425	0.001	0.469	$< 10^{-3}$
T	0.219	0.300	0.218	0.289	0.154	0.754
L_X	0.897	$< 10^{-3}$	0.270	0.105	0.890	$< 10^{-3}$
σ_v	0.221	0.289	0.100	0.987	0.231	0.256

Table 3.4: The distributions of the global cluster parameters are compared between the cosmological models using a K–S test. Values of $p_{KS} < 0.05$ indicate that two distributions of parameters are likely to be incompatible.

the emission–weighted temperature of the gas, computed by its thermal energy density assuming an ideal gas. The bolometric X–ray luminosity L_X is estimated as $\int \mathrm{d}V(\frac{\varrho_{gas}}{\mu m_p})^2 \Lambda_c$, where ϱ_g denotes the gas density, $\mu = 0.6$ is the mean molecular weight and Λ_c the cooling function, where the local temperature enters. A standard SPH estimator has been applied (Navarro et al. 1995); only the particles within r_{200} contribute to L_X.

First, we look how large the differences between the distributions of all relevant parameters are for the different cosmological models using a K–S test in Table 3.4. Additionally, the distributions at redshift $z = 0$ are shown in Figure 3.25. The results indicate that, except for the radius r_h and the luminosities, the distributions are compatible with each other. For the luminosity, there seems to be a systematic effect due to the cosmology, only the high–Ω_m models are consistent with each other. Regarding the half–mass radius, the CHDM model is distinguishable from the other models. For higher redshifts, most distributions become different. These results are useful later on, when we ask whether the fundamental planes are consistent with each other for the different cosmological models.

After these preliminaries, the fundamental planes were fitted using all galaxy clusters for each model. For each redshift, background model and parameter space, the best fundamental plane is searched using an orthogonal distance regression[11]. The quadratic scatter $\sigma_{fp}^2 \equiv \frac{1}{N_{cl}} \sum_{i=1}^{N_{cl}} d_i^2$ is minimized, where d_i denotes the distance of the ith cluster from the plane within the parameter space. From Figure 3.26 the evolution of the FP–parameters for two of the FPs can be seen. The exponents determining the FP seem to converge for all models for redshift $z = 0$. This supports the hypothesis that the fundamental plane is a global characteristic forming in every background cosmology. Since we do not have uncertainties within the measurements, we cannot draw physical error bars; however, it seems that the fundamental planes

[11] In part, we used the package ODRPACK, see Boggs et al. 1987; Boggs et al. 1989.

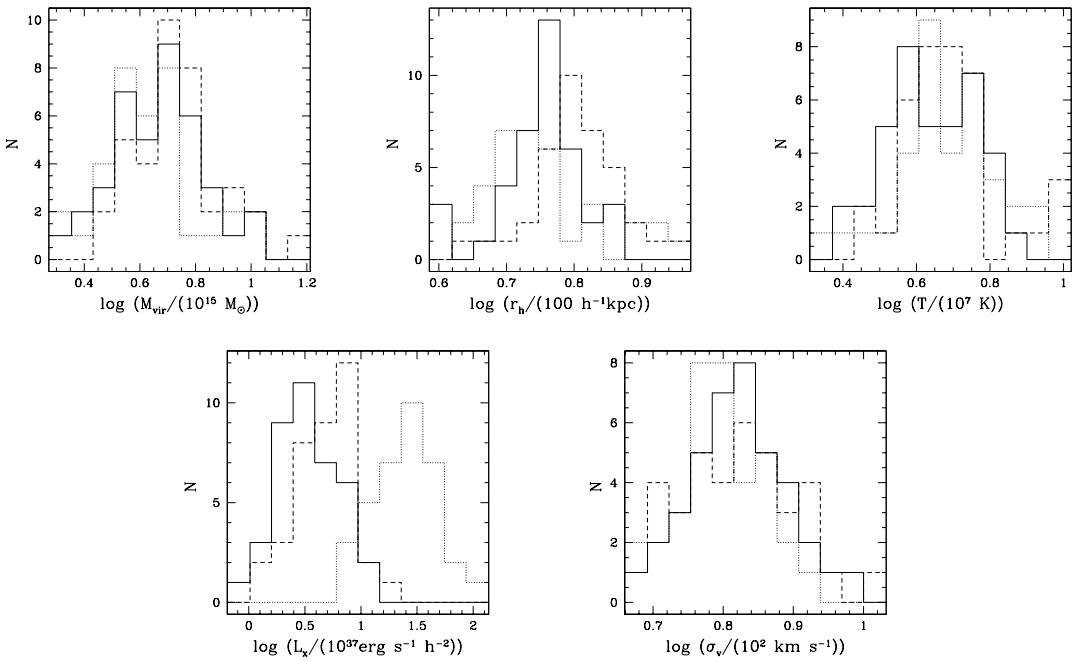

Figure 3.25: The distributions of the global cluster parameters for all cosmological models at $z = 0$. CDM: solid line; ΛCDM: dotted line; CHDM: short dashed line.

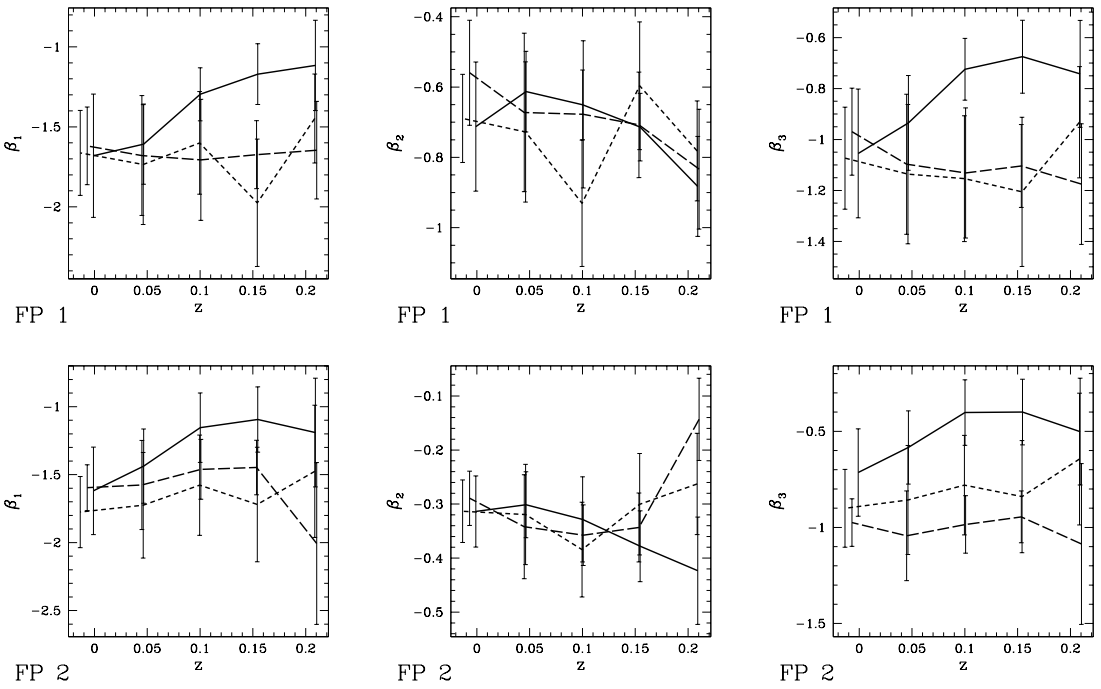

Figure 3.26: The exponents determining the fundamental planes together with their errors; since we do not have measurement–like errors, the 95% confidence regions visible in the plots are calculated assuming the goodness of the fit. CDM: solid line; ΛCDM: long dashed line; CHDM: short dashed line.

are consistent within the error bars. We show the 95% confidence regions in Figure 3.26, as usual in such a case, the errors are calculated using the covariance matrix and thereby *assuming* the goodness of the fit.
In Figure 3.27 we show the mean scatter around the fundamental planes as a function of redshift. The fundamental planes FP1 and FP2 clearly show the theoretically expected behavior, since the scatter goes down for lower redshifts, i.e. the clusters approach the plane indicating the dynamical equilibrium. This evolution is visible within all models. The third fundamental plane however does not show such a clear evolution to an equilibrium state. The reasons for this behavior will be explained below.
Note, that the scatters around the fundamental planes are comparable for all of the cosmological models. Thus, the pure scatter around the fundamental planes could not serve as a diagnostic tool for the distinction between different cosmological models.
We test this further and compare the distributions which the cosmological models show for the distances from the fundamental planes using a K–S test. From Table 3.5

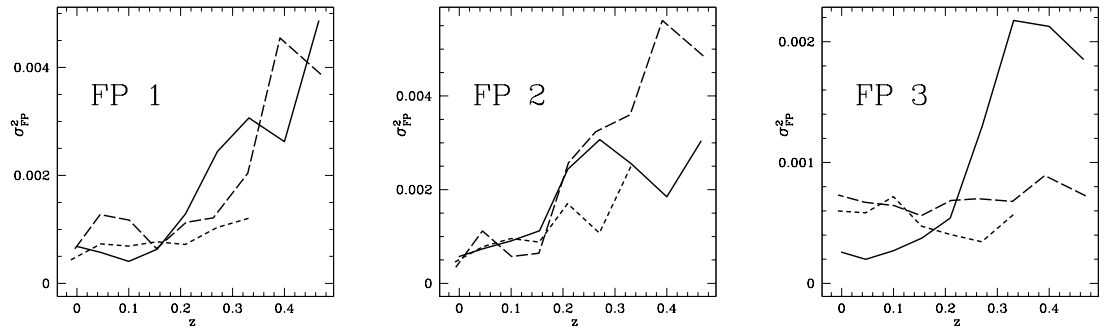

Figure 3.27: The mean quadratic scatter around the fundamental planes vs. redshift for all cosmological models (solid line: CDM; long dashed line: ΛCDM; short dashed line: CHDM). For technical reasons (a very strong outlier in the CHDM data) we consider the CHDM FP2 only for redshifts $z < 0.36$. In general, we do not remove outliers, but since for one cluster in the CHDM, the determination of L_X and a couple of other parameters leads into problems, we do not consider the CHDM model at $z > 0.36$.

we see that for most of the redshifts investigated, the distributions are consistent with each other. Only the ΛCDM and the CDM model are sometimes incompatible for the first and the second FP. For the third FP, the CDM model can be distinguished form the other ones. But the FP3 has to be interpreted with care. Altogether, this shows that we really need the substructure if we want to relate the inner states of galaxy clusters to the cosmological parameters.

But to what extent does the morphology of a cluster mirror its inner dynamical state? What is the connection between the cluster substructure and its distance from an equilibrium?

In Table 3.6 we ask whether the averaged structure functions (for the whole sample) and the mean scatter around the fundamental plane are correlated during redshift evolution. Again we use Kendall's τ; the results indicate that the mean cluster morphology and the mean scatter around the fundamental plane are well correlated except for the third fundamental plane, where sometimes (especially for the CHDM model) even significant anticorrelations occur.

In Figure 3.28 we give a visual impression of the fundamental planes. We fit a second fundamental plane to the data under the constraint that this plane is orthogonal to the first one (see Fujita & Takahara 1999). A new Cartesian coordinate system $\{x, y, z\}$ is chosen in order to let the best fitting plane coincide with the $x - y$–plane and the best fitting orthogonal plane with the $y - z$–plane. As one can see from Figure 3.28, seen from edge–on (third column), the fundamental plane is distinguished by a small scatter. Seen from face–on (first column), the morphology of the whole

FP 1	CDM - ΛCDM		CDM - CHDM		CHDM - ΛDM	
	d_{KS}	p_{KS}	d_{KS}	p_{KS}	d_{KS}	p_{KS}
0.21	0.172	0.603	0.281	0.081	0.307	0.053
0.15	0.085	0.999	0.141	0.817	0.134	0.882
0.10	0.429	0.001	0.230	0.233	0.228	0.271
0.04	0.304	0.052	0.211	0.325	0.144	0.817
0	0.275	0.100	0.271	0.102	0.176	0.590

FP 2	CDM - ΛCDM		CDM - CHDM		CHDM - ΛDM	
	d_{KS}	p_{KS}	d_{KS}	p_{KS}	d_{KS}	p_{KS}
0.21	0.186	0.502	0.130	0.881	0.287	0.083
0.15	0.319	0.036	0.196	0.417	0.236	0.236
0.10	0.116	0.952	0.151	0.744	0.183	0.539
0.04	0.196	0.438	0.214	0.310	0.136	0.869
0	0.196	0.433	0.148	0.764	0.179	0.567

FP 3	CDM - ΛCDM		CDM - CHDM		CHDM - ΛDM	
	d_{KS}	p_{KS}	d_{KS}	p_{KS}	d_{KS}	p_{KS}
0.21	0.152	0.755	0.174	0.572	0.208	0.377
0.15	0.344	0.019	0.315	0.035	0.192	0.480
0.10	0.295	0.065	0.304	0.047	0.154	0.754
0.04	0.383	0.006	0.356	0.012	0.202	0.415
0	0.383	0.006	0.267	0.112	0.222	0.301

Table 3.5: K–S tests for the distributions of the distances from the three fundamental planes among all models.

model	FP	C		A_1		S_1	
$\chi = 0.05$		τ	p	τ	p	τ	p
CDM	1	0.50	0.061	0.44	0.095	0.50	0.061
CDM	2	0.61	0.022	0.56	0.037	0.61	0.022
CDM	3	0.56	0.037	0.50	0.061	0.56	0.037
ΛCDM	1	0.56	0.037	0.67	0.012	0.61	0.022
ΛCDM	2	0.78	0.004	0.89	0.001	0.83	0.002
ΛCDM	3	0.22	0.404	0.33	0.211	0.39	0.144
CHDM	1	0.52	0.099	0.52	0.099	0.43	0.176
CHDM	2	0.43	0.176	0.43	0.176	0.52	0.099
CHDM	3	-0.90	0.004	-0.90	0.004	-0.81	0.011

Table 3.6: Correlation of the mean substructure functions (evaluated with a smoothing length of $\chi = 0.05h^{-1}$Mpc) and the mean quadratic scatter around the fundamental planes. The size of the window size is $1.4h^{-1}$Mpc.

plane resembles a band, the plane is not populated homogeneously, rather the clusters fan out along a line. This is true for all fundamental planes, especially for the third parameter space, and confirms results by Fujita & Takahara (1999), who found in a different threespace a morphology they call the "fundamental band".
The fact that FP3 nearly degenerates into a line allows us to understand the evolution of the scatter (Figure 3.27) in more detail: the "distance" from the FP is no longer well–defined, and the scatter as depicted in Figure 3.27 gets meaningless. Probably the parameters M, r_h and σ_v evolve to form a one–parameter family.
To explore the structure of the fundamental planes further, we investigate the scatter around the fundamental planes and the orthogonal planes in Figure 3.29. For the first two types of fundamental planes, both scatters decrease in a similar way resulting in a band that becomes thinner and narrower. The ratio of the scatters is increasing slightly, as visible from Figure 3.30. On the other hand, for the third fundamental plane, the scatters around the planes are relatively close to each other, and the evolution can be described as a collapse of the fundamental plane (for the ΛCDM and the CHDM models). Therefore, the notion of a plane gets meaningless in this case, the distance from the FP is no well–defined quantity any more, and the relation to substructure is different. – These results indicate, that we should also try to fit a line to our cluster data (see below).
So far we focused on the mean distance from the fundamental plane and the mean structure functions for the whole ensemble. But how reliably does the substructure reflect the dynamical state for individual clusters? Using the fundamental plane, we can try to answer this question. To "measure" the dynamical state of a cluster, we

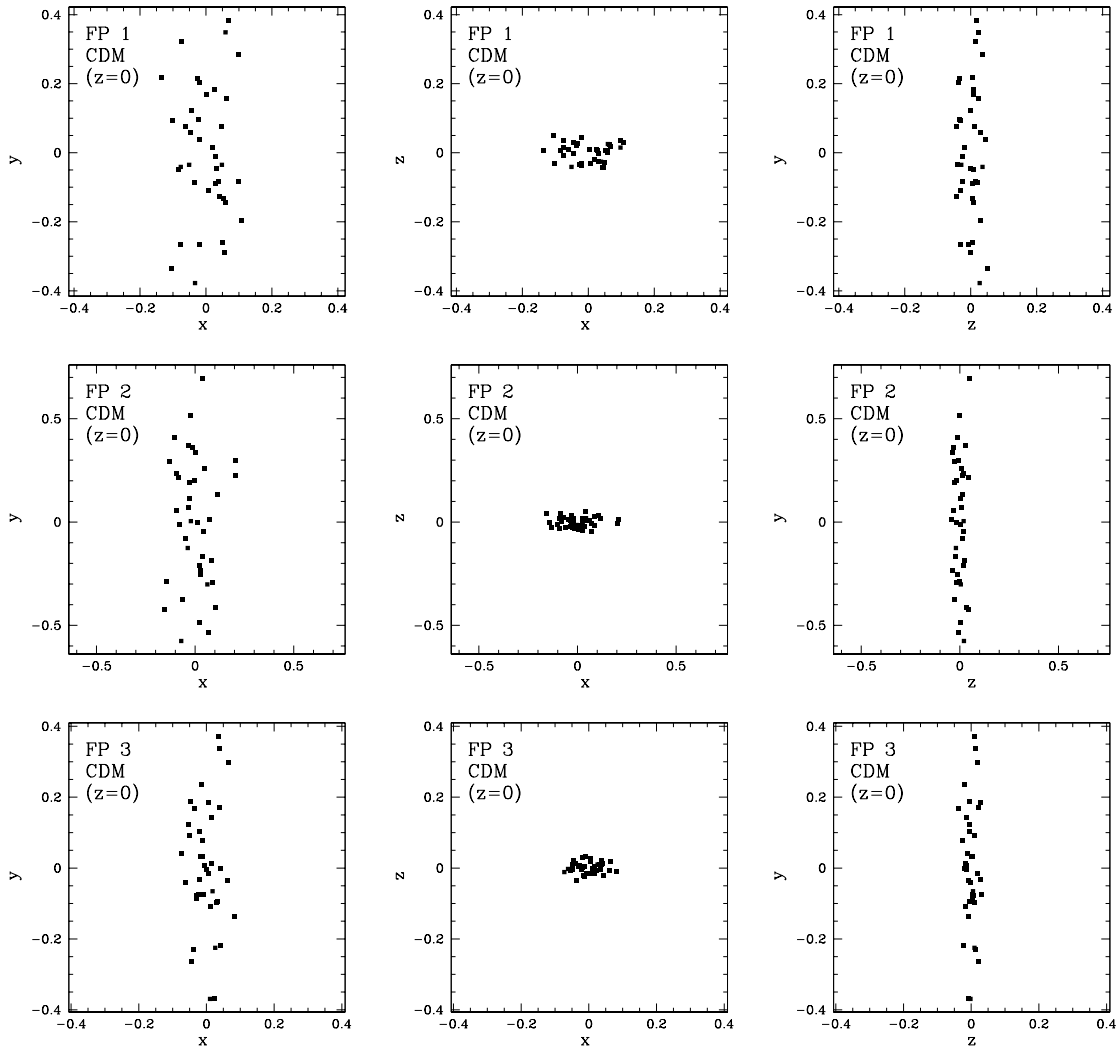

Figure 3.28: The fundamental planes. We consider the three FPs as defined in Equations (3.4.4)–(3.4.6). The coordinate axes x, y and z are defined in such a way, that the FP coincides with the $x - y$ plane.

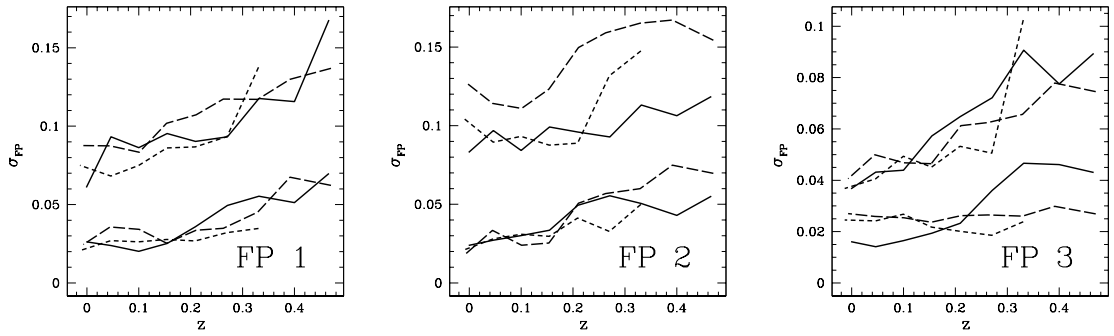

Figure 3.29: The scatters around the fundamental plane and the best fitting orthogonal planes. CDM: solid line; ΛCDM : long dashed line; CHDM: short dashed line.For technical reasons, we consider the CHDM model from $z \sim 0.27$ on, only.

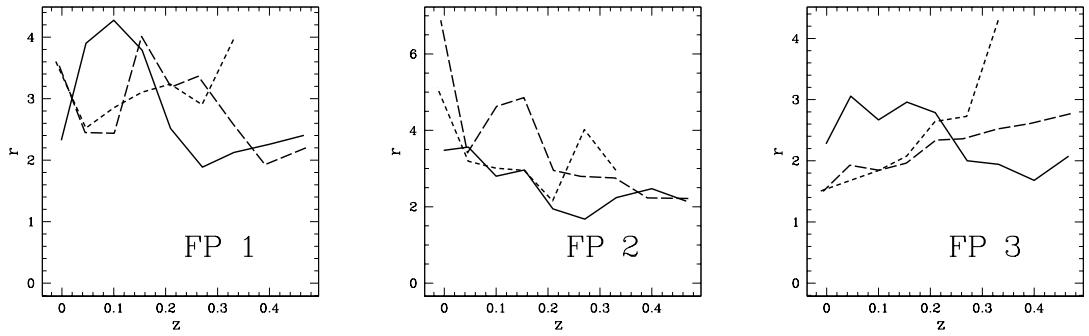

Figure 3.30: The ratio r of the scatter σ_{OP} (around the orthogonal plane) and the scatter σ_{FP} (around the fundamental plane) for the different background models: CDM: solid line; ΛCDM : long dashed line; CHDM: short dashed line.

calculate its distances from the FPs within the parameter spaces. We then correlate the FP–distance with the morphological structure functions (gas, for one random plane per cluster) using Kendall's τ. Note, that only τs for which the probability of the null hypothesis $p(\tau) < 0.05$ are supposed to indicate significant correlations. Results for low–redshift clusters are shown in Table 3.7. These results clearly confirm the connection between the substructure and the fundamental planes FP2 and also FP1. A number of positive correlations can be seen, which extend to both relevant fundamental planes and to all aspects of substructure. Thus, we establish the connection found by Fritsch & Buchert (1999) also for simulated X–ray clusters.
A closer analysis yields that even at higher redshifts, positive correlations between cluster substructure and inner cluster state can be seen. Note, that this is theoretically expected for higher redshifts, too, even if the scatter around the FP is much larger, since we do not ask for the existence of a fundamental plane, but for the deviations from a fundamental plane. In Figure 3.31, we visualize the results showing an evolutionary track of the τ (we show all τs where $p(\tau) < 0.05$ for one of the eleven structure functions under investigation with smoothing lengths of $0.05, 0.1, .., 0.3h^{-1}$Mpc). In detail, the distance from the second fundamental plane seems to be well correlated to substructure for all models and a number of redshifts. The distances from the first fundamental plane are reflected by morphology for the ΛCDM model, only. The physical nature of the third fundamental plane could not be confirmed for higher redshifts; a mixture of positive and negative correlations is to be found. Together with the visual impression of FP3, we explain this by the fact that this plane is the most probable and earliest one to collapse into a line.
In summa, we established a connection between substructure and dynamical state (measured within the second parameter space) for simulated X–ray clusters; but the statistical evidence for the results is not very strong. Below we test the performance of a number of different substructure measures, which prove to be worse and sometimes give anti–correlations. One critical point are projection effects; as outlined in Section 3.4.3, the substructure depends significantly on the direction the cluster is observed from; here we simply used one random plane per cluster thus mimicking real observations. We can strengthen our results by comparing the distances from the FPs with the averaged substructure quantities (averaged over three orthogonal projections). This is done in Table 3.7. Some of the correlations are clearly confirmed there, others are added. Especially the clumpiness seems to be well correlated with the distance from the FPs.
In Table 3.8 we show correlations between the DM morphology and the distance from the fundamental plane, the results are comparable with the ones of the gas morphology. We focus on the first two threespaces and do not consider the third FP.

There is another possibility to strengthen our claim regarding the connection between substructure and fundamental plane relations: We divide our samples into substructure–poor (p) and –rich (r) clusters with the aid of one of our structure functions, fit a plane in the parameter space for each subsample and ask which sub-

model	z	FP	r_w	χ	SF	τ	p
CDM	0	2	1.4	0.1	C	0.337	0.003
CDM	0	2	1.4	0.1	S_1	0.274	0.014
CDM	0	2	1.4	0.15	C	0.276	0.013
CDM	0	2	1.4	0.15	S_1	0.306	0.006
ΛCDM	0	1	1.4	0.15	C	0.236	0.046
ΛCDM	0.04	2	1.4	0.05	C	0.380	0.001
ΛCDM	0.04	2	1.4	0.05	A_1	0.240	0.042
ΛCDM	0.04	2	1.4	0.15	C	0.323	0.006
ΛCDM	0	2	1.4	0.15	C	0.236	0.046
CHDM	0.05	2	1.4	0.05	S_1	0.285	0.013
CHDM	0.05	2	1.4	0.1	C	0.292	0.011
CHDM	0.05	2	1.4	0.1	A_1	0.273	0.017
CHDM	0.05	2	1.4	0.1	S_1	0.309	0.007
CHDM	0.05	2	1.4	0.15	A_1	0.270	0.019
CHDM	0.05	2	1.4	0.15	S_1	0.372	0.001
CDM	0.05	2	1.4	0.05	C	0.239	0.032
CDM	0.05	2	1.4	0.05	S_1	0.271	0.015
CDM	0.05	2	1.4	0.1	S_1	0.239	0.032
ΛCDM	0.04	1	1.4	0.1	C	0.266	0.025
ΛCDM	0.04	1	1.4	0.15	C	0.321	0.007
ΛCDM	0.04	2	1.4	0.1	C	0.274	0.021
ΛCDM	0.04	2	1.4	0.15	C	0.278	0.019
ΛCDM	0	2	1.4	0.15	C	0.291	0.014
CHDM	0.05	2	1.4	0.05	C	0.317	0.006
CHDM	0.05	2	1.4	0.05	S_1	0.327	0.004
CHDM	0.05	2	1.4	0.1	C	0.321	0.005
CHDM	0.05	2	1.4	0.1	A_1	0.225	0.050
CHDM	0.05	2	1.4	0.1	S_1	0.360	0.002
CHDM	0.05	2	1.4	0.15	A_1	0.246	0.032
CHDM	0.05	2	1.4	0.15	S_1	0.369	0.001

Table 3.7: Results for a correlation analysis distance from the fundamental plane vs. gas morphology for the first two of the fundamental planes. We list all significant correlations ($p_{KS} < 0.05$) for the structure functions C, A_1 and S_1 for smoothing lengths of $\chi = 0.05, 0.1, 0.15 h^{-1}$Mpc. Above the double line, one projection per cluster is considered, beneath we take averaged structure functions (for each cluster we average over three orthogonal projections).

model	z	FP	r_w	χ	SF	τ	p
ΛCDM	0.04	2	1.4	0.1	C	0.235	0.047
ΛCDM	0.04	2	1.4	0.1	A_1	0.244	0.039
ΛCDM	0.04	2	1.4	0.15	C	0.252	0.033
CHDM	0.05	1	1.4	0.05	C	0.247	0.032
CHDM	0.05	1	1.4	0.1	S_1	0.234	0.041
CHDM	0.05	2	1.4	0.05	S_1	0.225	0.050
CHDM	0.05	2	1.4	0.1	C	0.228	0.047
CHDM	0.05	2	1.4	0.1	A_1	0.261	0.023
CHDM	0.05	2	1.4	0.1	S_1	0.282	0.014
CHDM	0.05	2	1.4	0.15	A_1	0.249	0.030
CHDM	0.05	2	1.4	0.15	S_1	0.231	0.044
CHDM	0	2	1.4	0.05	C	0.245	0.033
CHDM	0	2	1.4	0.05	A_1	0.285	0.013
CHDM	0	2	1.4	0.05	S_1	0.231	0.044
CHDM	0	2	1.4	0.1	A_1	0.297	0.010
CHDM	0	2	1.4	0.15	A_1	0.261	0.023

Table 3.8: Results from a correlation analysis distance from the fundamental plane (FP1 and FP2) vs. DM morphology. As in Tables 3.7, we consider only small redshifts as indicated in the table and the structure functions C, A_1 and S_1.

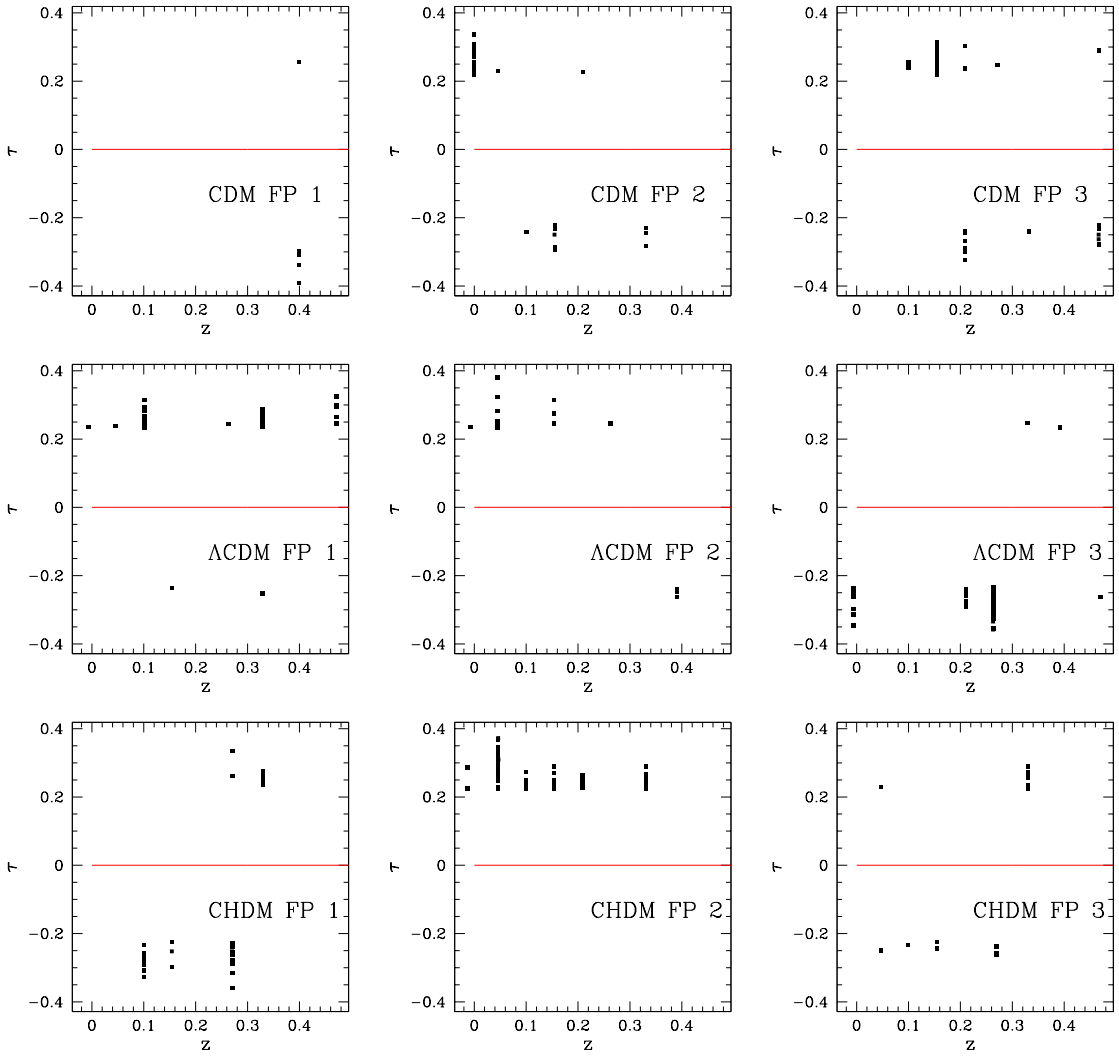

Figure 3.31: A summary of all significant correlations of substructure with the FP–distance using Kendall's τ for the whole redshift evolution of all models. Note, that for the CHDM model only redshifts $z < 0.36$ were considered. We consider C, A_0, A_1, S_0, S_1, S_2 and the rescaled A'_0, A'_1, S'_0, S'_1 and S'_2 for smoothing lengths of $0.05, 0.1, .., 0.3h^{-1}$Mpc.

model	sample	FP	N_{cl}	β^1	β^2	β^3	mean scatter×1000
($z \sim 0$) $A_1(\chi = 0.10h^{-1}\mathrm{Mpc})$ dividing the samples is $0.0108h^{-1}\mathrm{Mpc}$							
CDM	p	1	13	−2.57	0.01	−1.23	0.613
CDM	r	1	26	−1.47	−0.78	−0.95	0.542
CDM	w	1	39	−1.68	−0.71	−1.05	0.689
CDM	p	2	13	−1.80	−0.23	−0.79	0.400
CDM	r	2	26	−1.64	−0.34	−0.75	0.535
CDM	w	2	39	−1.62	−0.31	−0.71	0.570
ΛCDM	p	1	22	−1.89	−0.52	−1.13	0.411
ΛCDM	r	1	13	−1.59	−0.31	−0.81	0.493
ΛCDM	w	1	35	−1.62	−0.56	−0.97	0.601
ΛCDM	p	2	22	−1.83	−0.23	−1.05	0.275
ΛCDM	r	2	13	−1.58	−0.27	−0.94	0.308
ΛCDM	w	2	35	−1.60	−0.29	−0.97	0.343
CHDM	p	1	17	−1.51	−0.61	−0.90	0.223
CHDM	r	1	20	−1.80	−0.72	−1.21	0.529
CHDM	w	1	37	−1.66	−0.69	−1.07	0.426
CHDM	p	2	17	−1.60	−0.29	−0.75	0.360
CHDM	r	2	20	−1.91	−0.33	−1.01	0.418
CHDM	w	2	37	−1.78	−0.31	−0.90	0.424

Table 3.9: Fittings of the fundamental planes for all cosmological models. Each sample (one background model at one redshift) is divided into two subsamples using the structure function A_1. Then the fundamental plane is fitted within the three-space. We look whether the scatter around the FP is smaller for the sample with the substructure–poor clusters (p) than for the sample with the substructure–rich clusters (r).

model	sort of FP	χ	p
CDM	1	0.00	0.636
CDM	1	0.05	0.706
CDM	1	0.10	0.545
CDM	2	0.00	0.773
CDM	2	0.05	1.000
CDM	2	0.10	0.864
ΛCDM	1	0.00	0.864
ΛCDM	1	0.05	0.941
ΛCDM	1	0.10	0.909
ΛCDM	2	0.00	0.682
ΛCDM	2	0.05	0.529
ΛCDM	2	0.10	0.591
CHDM	1	0.00	0.455
CHDM	1	0.05	0.824
CHDM	1	0.10	0.818
CHDM	2	0.00	0.909
CHDM	2	0.05	1.000
CHDM	2	0.10	0.818

Table 3.10: Metastatistics for the divisions of the samples. We divide each sample (one model at one redshift) according to each substructure function for three different smoothing lengths and fit the fundamental planes for all models at the two smallest redshifts ($z = 0$ and $z \sim 0.05$). Then we average over the redshifts and the type of structure functions to summarize the behavior of the fundamental planes. p is the fraction of samples, where the substructure–poor clusters define the fundamental plane better than the substructure–poor clusters. $p \sim 0.5$ does not indicate anything relevant, only high ps show that the f–sample fixes the FP better than the r sample. One observers that especially for the second fundamental plane, the substructure mirrors the cluster inner dynamical state quite well.

sort of FP	sort of sf	p	sort of FP	sort of sf	p
1	C	0.533	2	C	0.800
1	A_0	0.533	2	A_0	0.533
1	A_1	0.733	2	A_1	0.933
1	S_0	0.833	2	S_0	0.778
1	S_1	0.611	2	S_1	0.778
1	S_2	0.889	2	S_2	0.778
1	A'_0	0.800	2	A'_0	0.667
1	A'_1	0.667	2	A'_1	0.889
1	S'_0	0.833	2	S'_0	0.833
1	S'_1	0.778	2	S'_1	0.722
1	S'_2	0.867	2	S'_2	1.000

Table 3.11: As in Table 3.10 we show the statistic from fitting the fundamental planes within the f and e–f sample. Here we compare the power of the substructure functions. Since there are many indications for the fact that the fundamental plane in the third threespace is not well–established, we omit it and refer only to our first two threespaces. The clumpiness and the shift of morphological properties is, e.g., more interesting for the cluster shape than the shape of cluster.

sample fixes the FP better than the other one (i.e. reduces the mean scatter more). This is in the spirit of Fritsch & Buchert (1999) where an empirical plane is distinguished from the fundamental plane defined by the substructure–poor clusters only. Since we want to compare different models whose structure functions are different on average, we take the same cut for all of the models; for each substructure function dividing the sample, we determine the cut in such a way, that for all models both the substructure–rich and the substructure–poor subsample have at least eight clusters. A problem about this method is that often the best fitting parameters for the smaller subsamples are not compatible with the fundamental plane parameters found for the whole sample (called w). This is, at least in part, caused by the small numbers of clusters within the subsamples; we do not exclude such problematic fits.
As an example we show some results for FP1 and FP2 in Table 3.9. Since we have a number of structure functions, and the smoothing length is a free parameter, too, there are a number of possible divisions of the samples. To get an overview, we carry out a sort of metastatistics where we compute the ratios of those sample divisions which result in scatters as theoretically expected (namely the scatter around the fundamental plane is smaller for the substructure–poor clusters), to all sample divisions. Results can be seen from Table 3.10. These results show that especially the second fundamental plane is better fixed within the threespace for the CDM and the CHDM model. As already expected, the first plane is weakly correlated to

substructure for the ΛCDM model. Comparing different χs, we see, that for higher χ better results are obtained. Therefore, to feature the dynamical state of a cluster, a higher smoothing length is useful.
In Table 3.11 we test the performance of the structure functions for the first two FPs. It turns out that, for instance, S_2' divides the sample in a way that is illuminating the dynamical properties of the clusters. To summarize the results, one can say, that the divisions of the samples confirm our previous results: the distance from an equilibrium is mirrored by substructure especially for the second parameter space.

A fundamental band?

Since we could show that in some parameter spaces band–like structures are forming, which become in part narrower throughout the dynamical evolution, it seems promising to fit the data also using a *line*; physically this means that the clusters form a one–parameter family. Again, we probe the link between morphology and dynamics.
We investigate the spaces of global parameters listed above and look at the following fundamental lines (FLs for the sequel):

1. fundamental line

$$\begin{aligned} \log\left(r_h/(100h^{-1}\mathrm{kpc})\right) &= \gamma_1^1 \log\left(M_{vir}/(10^{15}M_\odot h^{-1})\right) + \gamma_1^3 \quad , \\ \log\left(T/(10^7 K)\right) &= \gamma_1^2 \log\left(M_{vir}/(10^{15}M_\odot h^{-1})\right) + \gamma_1^4 \quad , \end{aligned}$$

2. fundamental line

$$\begin{aligned} \log\left(r_h/(100h^{-1}\mathrm{kpc})\right) &= \gamma_2^1 \log\left(M_{vir}/(10^{15}M_\odot h^{-1})\right) + \gamma_2^3 \quad , \\ \beta_2^2 \log\left(L/(10^{43} ergs^{-1}h^{-2})\right) &= \gamma_2^2 \log\left(M_{vir}/(10^{15}M_\odot h^{-1})\right) + \gamma_2^4 \quad , \end{aligned}$$

3. fundamental line

$$\begin{aligned} \log\left(r_h/(100h^{-1}\mathrm{kpc})\right) &= \gamma_3^1 \log\left(M_{vir}/(10^{15}M_\odot h^{-1})\right) + \gamma_3^3 \quad , \\ \log\left(\sigma_v/(10^2 km\ s^{-1})\right) &= \gamma_3^2 \log\left(M_{vir}/(10^{15}M_\odot h^{-1})\right) + \gamma_3^4 \quad . \end{aligned}$$

After having minimized the scatter around the lines to get the best fit for each model and each redshift, we trace the evolution of the scatter in Figure 3.32. Now the scatter decreases during the evolution for the first and third parameter space[12]. We show the best fitting lines in Figure 3.33 where the z–axis is orientated parallel to the fundamental line. The ranges in x– and y–direction mirror the length of the

[12]Note that during the whole discussion of the fundamental planes and lines statistical outliers have not been removed. Since statistical outliers tend to have a large influence on orthogonal distance fitting, it may be the case that one or the other fundamental plane is distorted by one or more outliers; for the most cases, however, a visual inspection shows that we are fitting the FP acceptably.

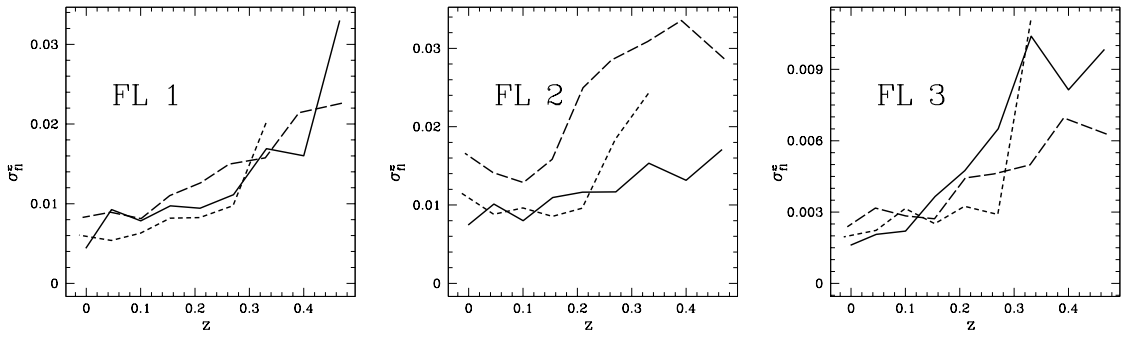

Figure 3.32: The scatter around the fundamental lines vs. redshift. CDM: solid line; ΛCDM : long dashed line; CHDM: short dashed line.

fundamental line along the z–axis. If the distribution of clusters collapses into a point within the $x - y$ plane, and the clusters are scattered isotropically around the line, the concept of a fundamental line is justified.
The results show that, especially within the third parameter space, a fundamental line is given, whereas in the other two parameter spaces a preferred direction still indicates the presence of a plane–like structure. A visual analysis of the redshift evolution shows that in the first threespace, a plane is formed which is collapsing, especially for the CDM and CHDM model. In the second threespace, a band is forming quite recently, whereas in the third threespace the distribution is plane-like at intermediate redshifts ($z \sim 0.5$) and is contracting then into a line. In Figure 3.34 we show the parameters γ_i^j determining the fundamental lines. They all seem to converge to compatible values for all models; only in the case of the second fundamental band where the luminosity enters, the ΛCDM model is very different from the other models. This, however, can be explained by the fact, that the ΛCDM–luminosities are incompatible with the luminosities of the other models (see Figure 3.25 and Table 3.4). Moreover, for higher redshifts the fitting is influenced remarkably by one outlier for the ΛCDM model.
In Table 3.12 we ask whether the distribution of the distances around the fundamental lines can distinguish the cosmological background models. The results of a K–S test clearly indicate that this is not the case. This is similar to the case of the fundamental plane, where the clusters were distributed around the fundamental plane in a similar manner within all cosmological models (see Table 3.5).
Now we want to answer the question, whether there is a connection between the cluster substructure and its dynamical state measured using the distance from the fundamental line. This would indicate that the fundamental line really corresponds to a sort of equilibrium state the cluster is reaching. A first test is again a comparison of the dynamical evolution of the averaged structure functions and the averaged

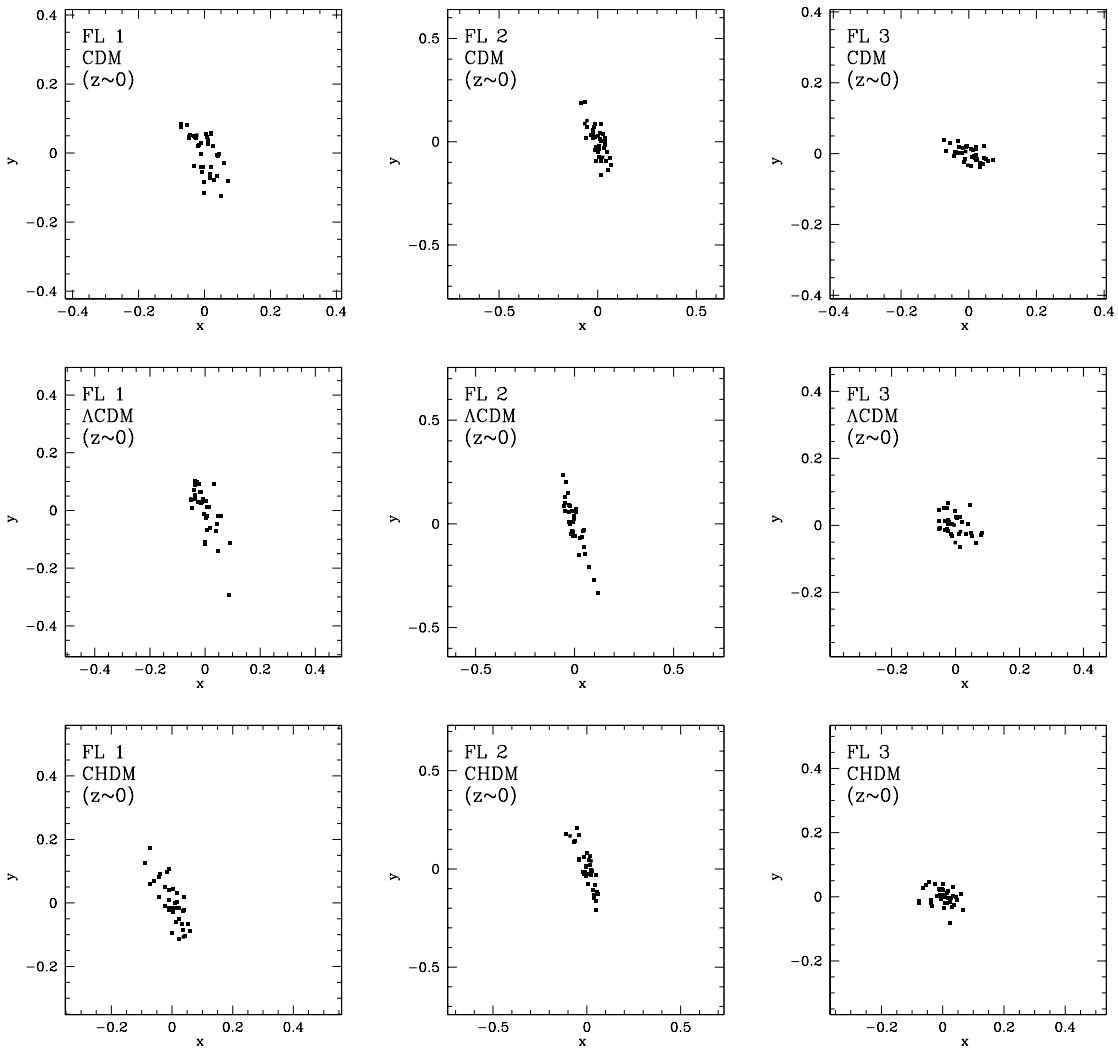

Figure 3.33: The fundamental lines. The FLs coincide with the z–axis.

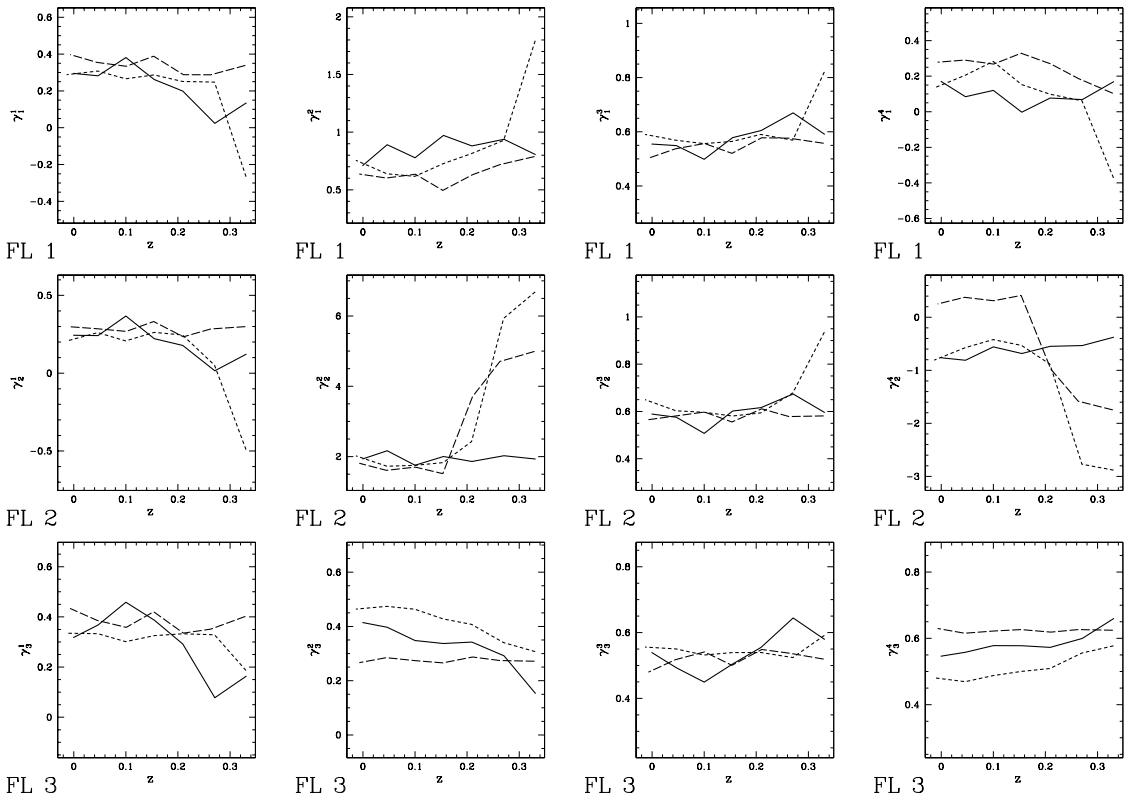

Figure 3.34: The exponents determining the fundamental lines vs. redshift. As usual: CDM: solid line; ΛCDM : long dashed line; CHDM: short dashed line. For technical reasons, we omit one of the redshifts for the CHDM model.

FL 1	CDM - ΛCDM		CDM - CHDM		CHDM - ΛDM	
$z \sim 0$	d_{KS}	p_{KS}	d_{KS}	p_{KS}	d_{KS}	p_{KS}
0.04	0.103	0.984	0.195	0.421	0.176	0.590
0	0.270	0.114	0.252	0.154	0.201	0.420
FL 2	CDM - ΛCDM		CDM - CHDM		CHDM - ΛDM	
$z \sim 0$	d_{KS}	p_{KS}	d_{KS}	p_{KS}	d_{KS}	p_{KS}
0.04	0.213	0.332	0.198	0.408	0.288	0.082
0	0.287	0.077	0.198	0.408	0.237	0.230
FL 3	CDM - ΛCDM		CDM - CHDM		CHDM - ΛDM	
$z \sim 0$	d_{KS}	p_{KS}	d_{KS}	p_{KS}	d_{KS}	p_{KS}
0.04	0.215	0.320	0.143	0.798	0.195	0.460
0	0.246	0.183	0.112	0.960	0.212	0.351

Table 3.12: K–S tests of whether the distributions of the distances from the three fundamental lines differ between the cosmological models. Almost no significant results are to be found, even for higher redshifts. The scatter around the fundamental lines is thus comparable for all models.

model	FL	C		A_1		S_1	
$\chi = 0.05$		τ	p	τ	p	τ	p
CDM	1	0.61	0.022	0.56	0.037	0.61	0.022
CDM	2	0.67	0.012	0.61	0.022	0.67	0.012
CDM	3	0.67	0.012	0.61	0.022	0.67	0.012
ΛCDM	1	0.83	0.002	0.94	0.000	1.00	0.000
ΛCDM	2	0.61	0.022	0.72	0.007	0.78	0.004
ΛCDM	3	0.72	0.007	0.83	0.002	0.78	0.004
CHDM	1	0.52	0.099	0.52	0.099	0.43	0.176
CHDM	2	0.14	0.652	0.14	0.652	0.05	0.881
CHDM	3	0.33	0.293	0.33	0.293	0.43	0.176

Table 3.13: Correlations (Kendall's τ) between the averaged substructure and the mean quadratic scatter around the fundamental line for a smoothing of $\chi = 0.05h^{-1}$Mpc and $r_w = 1.4h^{-1}$Mpc.

scatter around the fundamental line. Kendall's τ and the corresponding $p(\tau)$ can be found in Table 3.13. They show that, especially for the ΛCDM and the CDM model, the connection between the substructure and the deviations from the fundamental line are good. For the CHDM model, however, there are no significant correlations.
To complement this result, we ask whether the substructure of an *individual* cluster and its distance from the fundamental line are correlated. Results of a Kendall's test can be seen from Figure 3.35, where we trace the evolution of the correlation coefficients by marking all positive correlations found with one of our structure functions. Again, we take into account smoothing lengths of $0.05, 0.1, .., 0.3h^{-1}$Mpc and all of our eleven structure functions. As already the visual inspection of the global parameter space showed, for the second phase space, the fundamental line is not a good concept. This is confirmed by the behavior of the correlation coefficients which are more or less randomly distributed, some positive, some negative. For the first and also the third threespace, however, besides a small fraction of negative τs, one can see a number of positive correlations confirming the link between the substructure and the inner cluster state.
As mentioned above, the hypothesis of a connection between substructure and dynamical equilibrium (here measured by the distance from a fundamental line) can also be tested by dividing the samples according to their substructure functions. We show results of metastatistics in Table 3.14. Altogether they confirm the physical picture of the substructure for the first and third threespace. To summarize this subsection on *fundamental relationships* or *fundamental structures* (these labels may serve as a generic term for fundamental planes and lines or bands) one can state the following:

- Fundamental relationships can be observed within three phase spaces of global cluster parameters: the clusters form band–like structures in these spaces, which can be fitted using either a plane or a line.
- The exponents determining the fundamental relationships are compatible with each other for the different cosmological background models.
- There is a complex dynamical behavior of the clusters in the global parameter spaces: In the first parameter space a bandlike plane exists. In the second space there is a plane; in the third space a plane which existed at a redshift of $z \sim 0.4$ collapsed to form a band (ΛCDM , CHDM).
- During the dynamical evolution the scatter around the fundamental structures FP1, FP2, FL1, and FL3 is decreasing.
- There is no significant evolution of the FP–exponents governing the fundamental structures at low/intermediate redshifts.
- In most cases, the pure scatter around the fundamental structures cannot distinguish between the cosmological models.

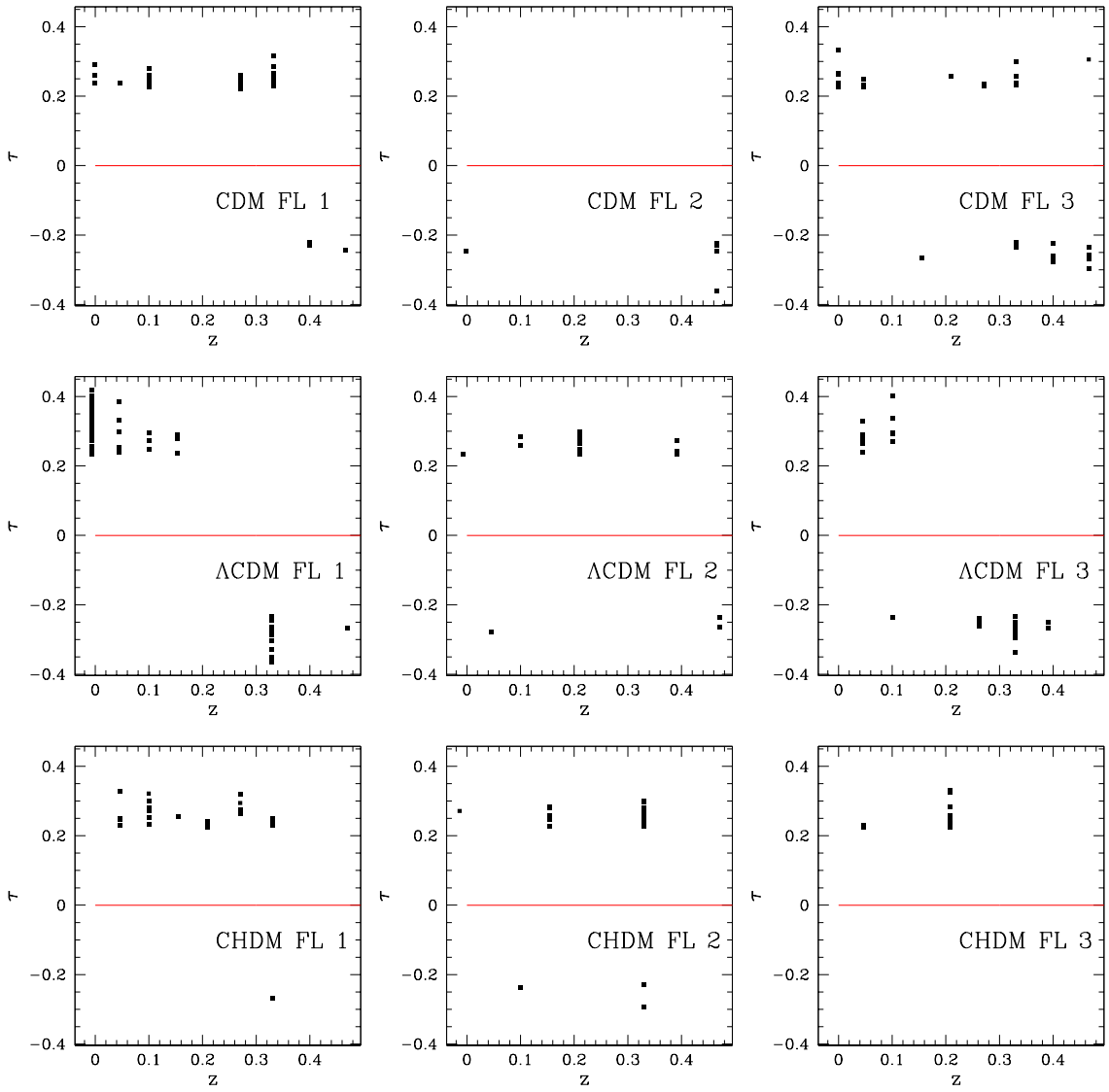

Figure 3.35: A summary of significant correlations of morphology with the FL–distances using Kendall's τ for the whole redshift evolution of all models. Here we take into account all significant correlations with one of our substructure measures for the X–ray images using smoothing lengths of $0.05, 0.1, .., 0.3h^{-1}$Mpc. We consider C, A_0, A_1, S_0, S_1, S_2, and the rescaled A_0', A_1', S_0', S_1', and S_2'.

model	sort of FP	χ	p
CDM	1	0.00	1.000
CDM	1	0.05	0.647
CDM	1	0.10	0.773
CDM	2	0.00	0.545
CDM	2	0.05	0.471
CDM	2	0.10	0.409
CDM	3	0.00	0.864
CDM	3	0.05	0.882
CDM	3	0.10	0.818
ΛCDM	1	0.00	1.000
ΛCDM	1	0.05	0.941
ΛCDM	1	0.10	0.727
ΛCDM	2	0.00	0.727
ΛCDM	2	0.05	0.588
ΛCDM	2	0.10	0.591
ΛCDM	3	0.00	0.773
ΛCDM	3	0.05	0.765
ΛCDM	3	0.10	0.545
CHDM	1	0.00	0.773
CHDM	1	0.05	0.471
CHDM	1	0.10	0.545
CHDM	2	0.00	0.318
CHDM	2	0.05	0.353
CHDM	2	0.10	0.455
CHDM	3	0.00	0.591
CHDM	3	0.05	0.824
CHDM	3	0.10	0.818

Table 3.14: A metastatistics for the performance of the substructure–poor and substructure–rich samples in fixing the fundamental lines. As above in Table 3.10, the whole cluster sample for each model and two redshifts was divided according to one of our structure functions evaluated at a certain smoothing length. p is the fraction of cases, where the p sample has lower scatter than the r sample as theoretically expected. The results show that for the first and especially the third threespace, the substructure traces the dynamical cluster state quite well.

- During dynamical evolution the average cluster substructure and the average scatter around the fundamental plane are correlated for most cosmological models.

- One can try to correlate the morphology and the distance from the fundamental structures which in some cases gives good results. Linking the morphologies of the fundamental structures, the evolution of the scatter and the relation to substructure gives a consistent picture for the cluster evolution: in the second parameter space a plane exists at $z = 0$, in the first space, a band–like structure indicates an equilibrium. In the third parameter space, there is weak evidence for positive correlations between morphology and distance from a line. We interpret these relationships, which are connected to substructure, as a physical equilibrium.

Comparison with power ratios

We compare these results to another quantification of cluster substructure, the power ratios introduced by Buote & Tsai (1995), see also Buote & Tsai 1996; Valdarnini et al. 1999. These measures are based on a spherical harmonics analysis of the gravitational potential estimated via the surface brightness[13]. We ask whether they reflect the dynamical state of a cluster at $z = 0$. Results of a correlation analysis for the distance from the fundamental plane/line are shown in Table 3.15 and in Table 3.16, respectively. We tested both three orthogonal projections for each cluster and the power ratios averaged over the three orthogonal directions. The results are rather insignificant, for the fundamental plane, we get no positive correlations, but a number of negative correlations for the third cluster phase space. Also for the fundamental line we get more negative than positive correlations. Altogether, the Minkowski valuations seem to be better in establishing the link between substructure and dynamical state.

3.4.5 Gas and Dark Matter distribution

But how are the Dark Matter and the gas related to each other? One example is given in Figure 3.36, where we show both the DM and the gas for one individual cluster. To conclude the investigation of the V–clusters, we try to answer that question in a statistical sense. The X–ray and the gas images were constructed as described above. Since we want to have statistical claims on the behavior of gas and DM, we construct for each cosmological model a sample by taking three orthogonal images per cluster as independent pictures. We analyze the gas images and the DM images separately and show scatter plots for all cosmological models in Figure 3.37. Obviously, there is a large scatter in the data, but there is a global trend, that the DM is more

[13]We got the power rations for our clusters by Valdarnini et al. (1999). They were computed for spherical images with a radius of $1.5h^{-1}$Mpc centered at the center of mass of the images.

model	FP	r_w	sort of proj.	sort of PR	τ	p
ΛCDM ($z \sim 0$)	2	1.5	1	1	-0.249	0.035
ΛCDM ($z \sim 0$)	2	1.5	2	1	-0.240	0.042
ΛCDM ($z \sim 0$)	2	1.5	3	1	-0.240	0.042
ΛCDM ($z \sim 0$)	3	1.5	0	1	-0.271	0.022
ΛCDM ($z \sim 0$)	3	1.5	1	1	-0.266	0.025
ΛCDM ($z \sim 0$)	3	1.5	2	1	-0.271	0.022
ΛCDM ($z \sim 0$)	3	1.5	3	1	-0.277	0.019
CHDM ($z \sim 0$)	3	1.5	1	4	-0.272	0.018
CHDM ($z \sim 0$)	3	1.5	2	4	-0.252	0.028
CHDM ($z \sim 0$)	3	1.5	2	5	-0.246	0.032

Table 3.15: The significant correlations of the power ratios with the distance from the FP.

model	FP	r_w	sort of proj	sort of PR	τ	p
ΛCDM ($z \sim 0$)	3	1.5	0	1	-0.257	0.030
ΛCDM ($z \sim 0$)	3	1.5	1	3	0.254	0.032
CDM ($z \sim 0$)	1	1.5	2	2	0.257	0.021
CDM ($z \sim 0$)	2	1.5	1	3	-0.220	0.049
CDM ($z \sim 0$)	3	1.5	0	2	-0.342	0.002
CDM ($z \sim 0$)	3	1.5	1	2	-0.380	0.001
CDM ($z \sim 0$)	3	1.5	3	2	-0.273	0.014

Table 3.16: Here the power ratios were correlated with the distance from the fundamental line. We list all significant correlations found within all of our data. We use cluster images from three orthogonal projections labelled by $0, 1, 2$. We also averaged the power ratios over the three projections (labelled by 3).

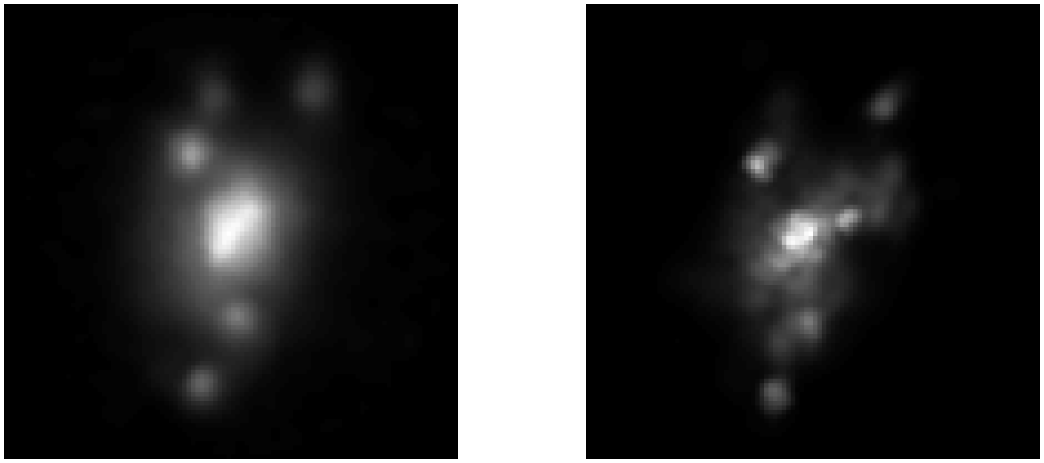

Figure 3.36: The cluster 05 in the CDM model at $z \sim 0.05$. An X-ray image constructed by the gas particles (left panel) and an image constructed by the DM (logarithmic color scale).

substructure–rich, at least at this smoothing scale. One can interpret these diagrams as a sort of phase diagrams. Using an orthogonal distance regression we fit a line to our data, but a caveat is appropriate insofar as the scatter is very large and the fit is probably influenced by outliers. We show the best fitting slopes for a number of different smoothing lengths in Figure 3.38 and add as a different measure the averaged ratio of $\frac{C(DM)}{C(gas)}$ for each cosmological model. These results show systematically, that the DM has a higher clumpiness than the gas. – It is difficult to obtain similar results for the other structure functions, since the fittings are often influenced by outliers, and the averaged ratios by clusters with very small structure functions.

3.5 A morphology–cosmology connection for optical galaxy clusters?

In this section we investigate optical galaxy clusters with the aid of the Minkowski valuations. Since galaxy clusters typically consist of the order of $30 - 300$ galaxies (Bahcall 1996), single points may bear important information, therefore, an investigation with the Boolean grain method which is more sensitive to local information than the excursion set approach is appropriate.
We first illustrate our method with the aid of the real cluster Cl 0016+161 observed by Belloni & Röser (1996). They give the angular positions and spectral properties of galaxies in a field of $3.5' \times 3.5'$ size and brighter than $R = 23.5$mag. A galaxy is considered as cluster member, if its redshift lies within a fixed redshift range dependent on the morphological type. Roughly following Belloni & Röser (1996),

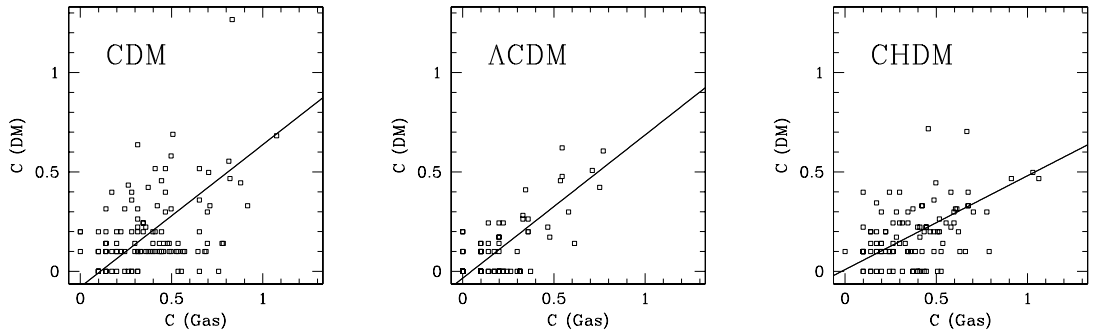

Figure 3.37: The structure function C for the gas and the DM for all cosmological models. Each points represents one image, in each case a smoothing with $0.05h^{-1}$Mpc was applied. Often structure functions coincide at one data point.

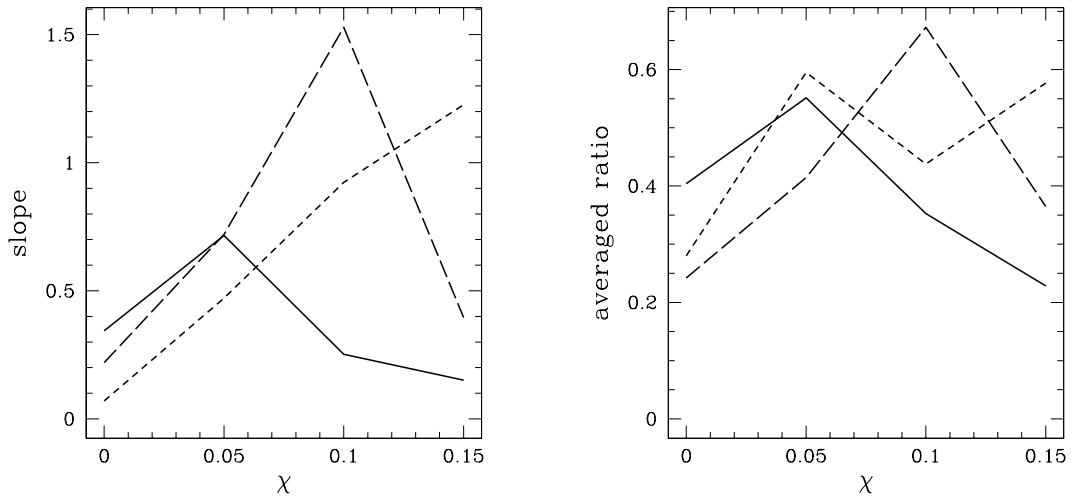

Figure 3.38: The slope of the best fitting line in a scatter plot C(Gas) vs. C(DM). In the left panel we show the ratio of $\frac{C(Gas)}{C(DM)}$, averaged over the whole cluster sample. As usual CDM: solid line; ΛCDM : long dashed line; CHDM: short dashed line.

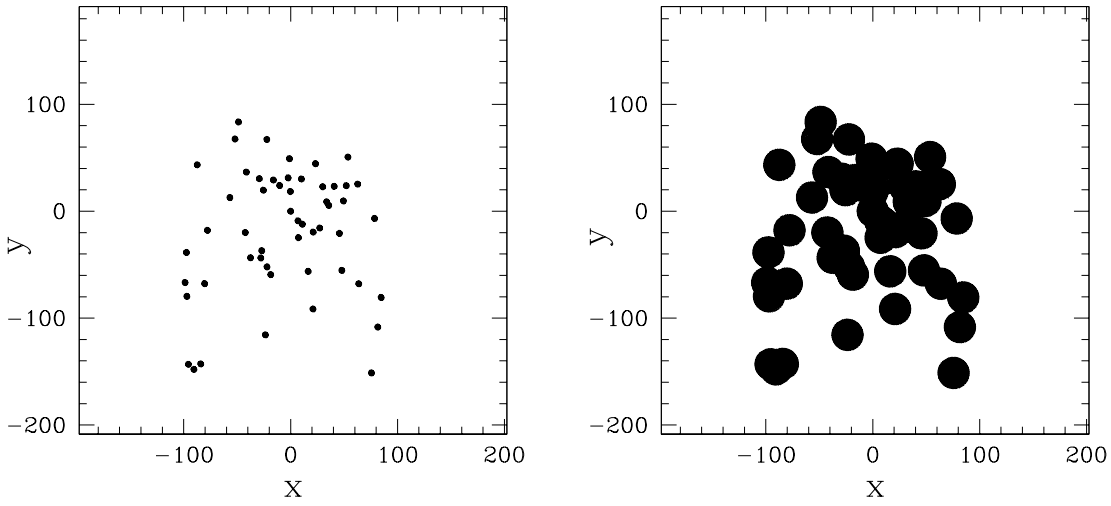

Figure 3.39: The positions of the galaxies for the cluster Cl 0016+161 (left panel) and an illustration of the Boolean grain method (right panel).

the redshift range is $0.525 < z < 0.575$ for the elliptical and A+E galaxies, and $0.515 < z < 0.585$ for spirals and irregulars. We consider only those galaxies, whose morphological type could be determined (*cf.* Table 5 in Belloni & Röser 1996). In Figure 3.39 we show the positions of the cluster galaxies. To apply the Boolean grain method, we put spherical windows of different radii around the center of mass of the points and compute the Minkowski valuations for the intersection of the union set of all Boolean grains and the spherical window. For a statistical comparison, we simulate 100 realizations of an inhomogeneous, but spherically symmetric Poisson process following the same density profile as the observed cluster Cl 0016+161. The radial galaxy number density profile for Cl 0016+161 is estimated by collecting the galaxies in bins around the center of mass. We tested several binnings which qualitatively gave similar results. Then we simulate a spherically symmetric Poisson processes characterized by the same radial profile (Stoyan & Stoyan 1994). This serves as a non–parametric spherically symmetric reference model to compare the real data to. Results can be seen from Figure 3.40. By definition of our reference model, the curves for the volume V_0 vs. radius are similar for the real cluster and the Poisson model. Also the other scalar Minkowski functionals are roughly consistent within the 1σ fluctuations. However, the curvature centroids reveal that this cluster is incompatible with a spherically symmetric Poisson process around its center of mass: the y–component of all curvature centroids lies outside the 1σ variations of the Poisson model. This shows that the higher–order Minkowski functionals contain more detailed information than their scalar counterparts. They also uncover the direction where the substructure is to be found. We now turn to the question whether

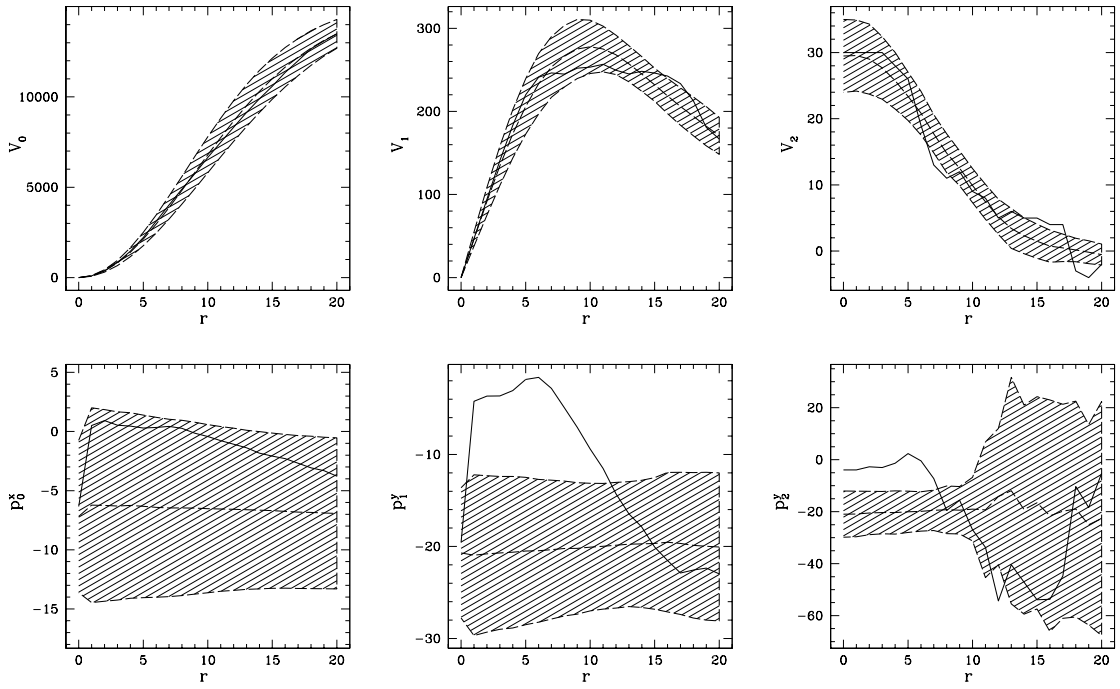

Figure 3.40: A comparison of the cluster Cl 0016+161 (solid line) and a spherically symmetric Poisson process (dashed line, the shaded areas indicate the 1σ fluctuations) using the Boolean grain method. We put a spherical window of $69''$ on the points and investigate the union set of the Boolean grains. The radius of the Boolean grains r is given in units of arcseconds. The Minkowski functionals and the curvature centroids are given in units of powers of arcseconds, too.

a cosmology–morphology connection can be found for optical galaxy clusters within the GIF–simulations.

Cluster galaxies in simulations. From numerical simulations we get cluster galaxies using the "semianalytical models" discussed, e.g., by Kauffmann et al. (1999); Diaferio et al. (1999). The basic idea behind this sort of models is to follow merger histories in order to get stable galaxies and to insert some global properties of the galaxies like morphological type and luminosity using well–established scaling relations. Of course, there are a number of cautions to be kept in mind with such semianalytical models, but after all they supply galaxies for N–body simulations. For all clusters in the simulations with masses M_{200} larger than $10^{14} M_{\odot} h^{-1}$ we have all galaxies within r_{200} around the cluster center; M_{200} is the integrated mass of all cluster parts where the mass density exceeds 200 times the critical density and r_{200} is the scale corresponding to M_{200}.
We investigate two models, one high–Ω_m model (τCDM) and one low–Ω_m model (ΛCDM)[14]. We have 80 clusters for the ΛCDM model and 57 clusters for the τCDM model at $z = 0$. The galaxies are only complete up to magnitudes $M_V < -17.5 + 5\log(h)$, thus we only consider galaxies with magnitudes smaller than this bound in the V–band.
To estimate the cluster scales we compute the radius which contains half of the galaxies around the center of mass ("half–galaxy radius") and a parameter from the convex hull of the points. The first radius refers to the core of the cluster. We find that on average the half–galaxy radius is larger for the ΛCDM model, whereas the other radius is within the τCDM model. As an estimate of the cluster scale, we prefer the half–galaxy radius, since it is more stable than the other estimates.
For the Boolean grain method we proceed as described in Chapter 2.1; the window is chosen large enough to contain the whole cluster with all Boolean grains. We vary the radius of the Boolean grains from 0 to $1h^{-1}$Mpc. We sum over one hundred bins within this range to get the shift parameters[15] s_i and S_i for $i = 0, 1, 2$, as well as the asymmetry parameters A_j for $j = 0, 1$ and the axis ratios X_k for $k = 0, .., 6$. Results are shown in Table 3.17. There is a clear evidence that the ΛCDM clusters have less substructure than the τCDM clusters. This shows that there is also a cosmology–morphology connection for optical galaxy clusters. The application of a K–S test shows that indeed the differences between the models are significant. Only the shift and asymmetry parameters reveal significant differences between both cosmological background models. The anisotropy parameters are only marginally different between the models. These results could be confirmed using the excursion set approach. Two structure functions are shown for different smoothing lengths in

[14]Because of technical reasons, only these models were accessible.

[15]For technical reasons, we neglect the shift parameters for the centroid $\mathbf{p}_0$, since it is dominated by fluctuations due to the Monte Carlo integration. Also the asymmetry parameters may be affected by this.

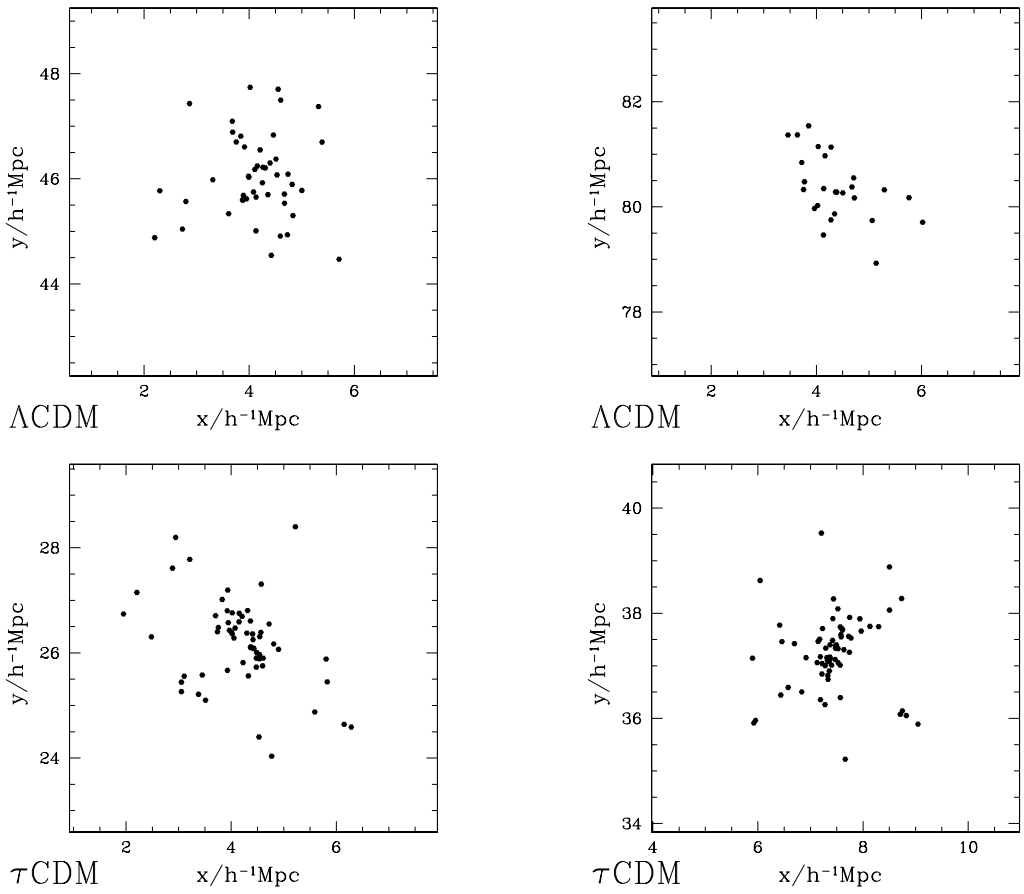

Figure 3.41: Two clusters in the optical from the GIF–simulations for the ΛCDM and the τCDM clusters each, at redshift $z = 0$. We show only the galaxies with $M_V < -17.5 + 5\log(h)$, where M_V is the absolute magnitude in the V–band.

	ΛCDM		τCDM		K–S test	
	average	r.m.s.	average	r.m.s.	d_{KS}	$p(d_{KS})$
s_1	0.778	0.268	0.943	0.239	0.38	$< 0.1\%$
s_2	16.418	17.472	18.414	19.441	0.15	42.1%
S_1	0.126	0.062	0.141	0.050	0.24	3.6%
S_2	0.595	0.418	0.655	0.380	0.22	6.0%
X_0	0.834	0.176	0.827	0.189	0.09	94.5%
X_1	0.637	0.304	0.625	0.268	0.11	77.1%
X_3	0.160	0.063	0.165	0.076	0.09	93.7%
X_4	0.669	0.279	0.677	0.240	0.15	43.4%
X_5	0.160	0.063	0.165	0.076	0.09	93.7%
A_0	0.056	0.050	0.066	0.041	0.28	0.9%
A_1	1.629	0.764	1.802	0.635	0.33	0.1%
s_1'	1.143	0.389	1.637	0.524	0.46	$< 0.1\%$
s_2'	20.964	15.642	27.390	19.760	0.23	5.6%
S_1'	0.186	0.091	0.249	0.120	0.29	0.5%
S_2'	0.816	0.407	1.066	0.429	0.33	0.1%
A_0'	0.115	0.079	0.190	0.108	0.39	$< 0.1\%$
A_1'	2.337	0.807	3.047	0.881	0.40	$< 0.1\%$

Table 3.17: A comparison of the ΛCDM and the τCDM model using optical galaxy clusters and the Boolean grain method. The first two columns show the mean structure functions together with their r.m.s. fluctuations. The other columns contain the result of a K–S test. The meanings of the tensors behind the anisotropy parameters X_i are listed in Table 1.1.

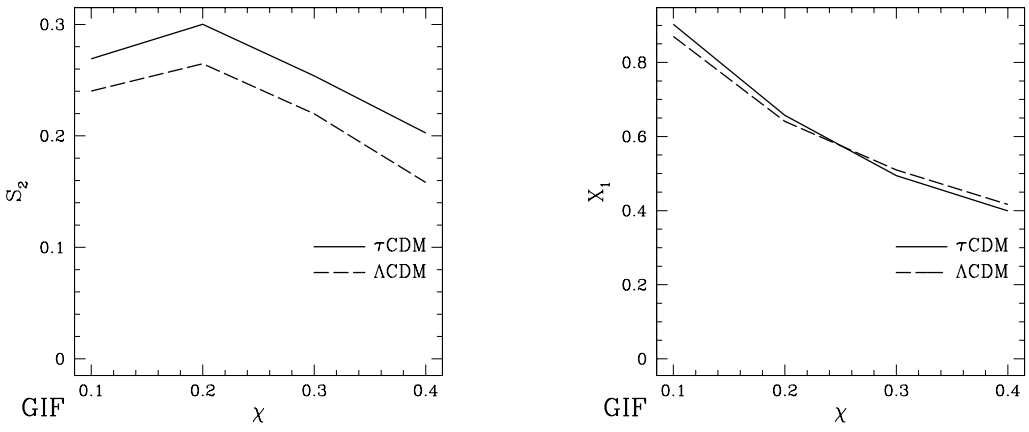

Figure 3.42: Two structure functions comparing the optical galaxy clusters for the excursion set approach. We show the values of the structure functions vs. the smoothing length χ.

Figure 3.42. Note, however, that, if we rescale the structure functions by the radius of the convex hull, the results become insignificant, or point into the wrong direction.

3.6 Summary and outlook

The Minkowski valuations provide an elegant framework to characterize the morphology of patterns. They are based on a solid mathematical ground and can be characterized axiomatically. The mathematical theory of integral geometry provides a number of results which allow for an effective computation of the Minkowski valuations. Based upon the hierarchy of Minkowski valuations, we constructed a number of structure functions which are well–suited to characterize different aspects of the substructure found in galaxy clusters.

Using these tools we could show that the morphology of galaxy clusters can effectively discriminate between different cosmological background models within cosmological simulations. The Dark Matter distribution as well as the X–ray images of clusters and the distribution of the cluster galaxies permit us to constrain the values of the cosmological parameters.

Furthermore, we investigated the relation between the inner dynamical state of a cluster and its substructure. To measure the intrinsic cluster state we used the concept of fundamental plane relations, which hold in certain spaces of global cluster parameters. Our results indicate that, at least for some fundamental plane relations, the distance from the fundamental plane is mirrored by the substructure.

The measures developed in this part, however, are not only suitable for cluster investigations, but also for the morphometry of cosmic structure on larger scales. Homogeneity and isotropy are principles which govern our understanding of the Universe. They enter most of the cosmological models, and even a number of statistics for the cosmic structure such as usual estimates of the two–point correlation function (Peebles 1980; Kerscher 1999) presuppose homogeneity and isotropy. With the aid of the Minkowski valuations, especially the higher–order ones, one can test to what extent and from which scale on those assumptions are fulfilled (scale of homogeneity).
In the second part of this work we turn indeed to the large–scale structure, but from a different point of view. We consider the spatial information given by the positions of galaxies together with their intrinsic properties.

Part II

Mark correlations and the bias problem

Introduction

Illuminating the Universe nowadays means in particular to illuminate the nature of the Dark Matter which is thought of as filling the Universe as its main component. For the cosmologist Dark Matter comes up in the fields of statistics and the theories of structure formation. The main questions are: How is the Dark Matter distributed? And what is its imprint on the formation of cosmic structures such as galaxy clusters?

The efforts of the following chapters are loosely connected to the first of these questions. Since the Dark Matter is not directly observable, one usually investigates the distribution of the luminous matter such as galaxies and tries to fill the gap between luminous and Dark Matter using biasing schemes. One particular issue in this context is the question of whether certain classes of objects trace the distribution of the Dark Matter reliably. There was a long–standing debate on whether different classes of objects, galaxies of different morphological types or luminosities, e.g., are differently distributed on the sky, in other words whether they are biased with respect to each other. Therefore, the big *bias problem* of how the Dark Matter is related to the luminous one is being translated into a number of small bias problems of whether the distribution of certain objects is biased towards the distribution of other objects. Indeed, one observed that in series of volume–limited samples the clustering properties change slightly; in particular, the amplitude of the two–point correlation function grows when deeper samples are investigated (Park et al. 1994). This observation was usually interpreted as an imprint of *luminosity segregation*: Since deeper volume–limited samples (given a fixed flux limit of the detector) trace only the more luminous galaxies, a peculiar distribution of the brightest galaxies would change the amplitude of the correlation function. However, Pietronero and coworkers gave an alternative explanation of why the clustering strength was growing for deeper samples (Sylos Labini et al. 1998): if the Matter distribution in the Universe is a fractal, the notion of homogeneity on which an estimation of the two–point correlation function is based on becomes meaningless. Pietronero and coworkers showed that for a fractal distribution the "scale of nonlinearity" (often referred to as "correlation length", see Gaite et al. 1999 for an interpretation) grows linearly with the sample depth. More generally, one does not need to believe that the Universe is a fractal to question the standard argument, since any inhomogeneity in the data (eventually generated by evolution effects) renders the usual approach problematic.

So there was a degeneracy between claims on luminosity segregation and fractality (or more generally inhomogeneity on large scales).
Additionally, there were a couple of other investigations asking whether the clustering of galaxies depends on their intrinsic properties. The empirical investigations mainly probed two directions. The first direction investigated the large–scale distribution of galaxies. As main tool two–point statistics such as the two–point correlation function were used; they were calculated for different subsamples determined by intrinsic properties of the galaxies, see, e.g., Binggeli et al. 1990; Hermit et al. 1996; Davis et al. 1988; Einasto 1991a; Einasto 1991b for morphology segregation, and Hamilton 1988; Davis et al. 1988; Benoist et al. 1996 for luminosity segregation. To avoid the degeneracy with claims of fractality, at least partly one constrained to one fixed volume.
Sometimes also higher–order and non–standard statistics were employed to test for luminosity and morphology segregation, for instance the void probability function (Maurogordato & Lachièze–Rey 1987), the skewness (Benoist et al. 1999), and a multifractal analysis (Domínguez-Tenreiro & Martínez 1989); see also (Domínguez-Tenreiro et al. 1994). Tully (1988) and White et al. (1988) investigated the distribution of distances for different galaxy classes. Santiago & Strauss (1992) focused on the local densities dependent on morphology. Most of these works compare statistical descriptors for different subsamples, but do not develop specific measures to confirm or to characterize an eventual segregation more closely. Only Börner et al. (1989) introduced a scheme where correlation functions were weighted with the luminosity. Alimi et al. (1988) focused on ratios of correlation functions to overcome the normalization problem.
To summarize the results of these works, one found luminosity segregation for a number of samples in the sense that bright galaxies cluster more strongly than the dim ones. The analysis often was not scale–dependent, but some authors claim to have found luminosity segregation even at large scales of $\sim 10h^{-1}$Mpc, see, e.g., Mo et al. 1992. Morphology segregation was discovered in a couple of catalogues, too.
A second direction of research focused on galaxy clusters and looked at the distribution of the galaxies of different types within the clusters, see, e.g. Giovanelli et al. 1986; Andreon 1994; Andreon 1996; Caon & Einasto 1995; Adami et al. 1998a; Giuricin et al. 1988. Luminosity segregation in clusters was investigated, too (Capelato et al. 1980; Adami et al. 1998a; Magtesyan & Movsesyan 1995). This line of research was mainly directed by the well–known morphology–density relation (Dressler 1980) which states that in clusters elliptical galaxies prefer the high–density regions (compare also Postman & Geller 1984).
However, a unifying framework for all these investigations was missing so far. Most of the work done within this area of research applied usual point process statistics to a couple of subsamples or used ad–hoc defined measures. Statistics which concentrate on the interplay of the spatial clustering and the inner properties of the galaxies have not yet been developed. Another weak point was the analysis of errors: almost none of the cited works quantifies the statistical errors to be expected in such

an analysis. Therefore, the claims on luminosity segregation have to be handled carefully. Regarding the question of how the claimed luminosity segregation looks like, no quantitative study was done.
These difficulties shall be addressed in the present part under recourse to mathematical theory. We raise the question of luminosity/morphology segregation in the more general context of mark correlations. We discuss this in the mathematical framework of marked point processes. Marked point processes generate random point sets where the points bear intrinsic properties. The mathematical theory allows us to introduce simple test quantities which ask whether there is an interplay between the spatial clustering of the points and their intrinsic properties. A mathematical treatment has many advantages; especially it allows us to break the degeneracy between claims of luminosity segregation and fractality. It also enables us to asses the statistical significance of claims regarding luminosity segregation. We can define unbiased estimators for our test quantities and furthermore compare with analytical models.
In Chapter 4 the basic concepts constituting the theory of marked point processes are developed. We also clarify the notion of mark segregation there. A number of statistical test quantities is introduced in Chapter 5. We concentrate on two–point properties, but mention higher–order statistics, too. In Chapter 6 we ask for luminosity and morphology segregation within real data. We investigate the SSRS 2 galaxy catalogue. To understand the signals of luminosity segregation found at a high level of significance, we compare with different models in Section 6.3. In Chapter 7 we show that marked point processes are an appropriate framework to model the bias[16].

[16]Part of the results presented in this part were published in (Beisbart & Kerscher 2000).

Chapter 4

Marked point processes and their description

Suppose one is given the positions and some intrinsic properties of objects within a well–defined sample. Usually a good ansatz to analyze such data is to interpret them as a realization of a random process. Random processes which produce points in space together with their intrinsic properties are called marked point processes. In this chapter we provide an introduction into marked point processes. We develop the basic concepts (Section 4.1) and clarify the notion of mark segregation (Section 4.2). The mathematical foundations were developed by Stoyan (1984) and Stoyan & Stoyan (1994), where also some mark–weighted correlation functions were proposed.

4.1 Basic theory of marked point processes

To begin with, we have N data points $\{(\mathbf{X}_i, M_i)\}_{i=1}^N$ with positions $\mathbf{X}_i \in \mathcal{D} \subset \mathbb{R}^d$ within the sample geometry $\mathcal{D}$ and marks $M_i \in \mathbb{M}$. The marks have to represent intrinsic properties of the objects, one may think of the luminosity L_i of a galaxy or its mass. Discrete marks such as the morphological type or vector–valued marks such as the velocity or an orientation are possible, too; thus, we do not specify the mark space $\mathbb{M}$ further. It is, however, useful at this point to restrict ourselves to real properties of galaxies; apparent qualities such as the redshift or the apparent magnitude are discussed later on.
Marked point processes, on the other hand, are defined via statistical ensembles and described via moments or probability densities. Of course, the pure points $\{\mathbf{X}_i\}_{i=1}^N$ as well as the marks $\{M_i\}_{i=1}^N$ can be thought of and characterized as realizations of separate point processes each. The spatial part of the marked point process can be described using the hierarchy of moments, such as the one–point density $\varrho^{\mathcal{S}}(\mathbf{x})$. In many cases it is appropriate to assume homogeneity of the point process; then the mean density $\overline{\varrho}$ can be estimated using the ratio $\frac{N}{|\mathcal{D}|}$, where $|\mathcal{D}|$ is the volume of the

sample $\mathcal{D}$. Higher–order statistics are based on the n–point probabilities of finding n points within the volumes $\mathrm{d}V_1$, $\mathrm{d}V_2$,.. and $\mathrm{d}V_n$ centered at $\mathbf{x}_1$, $\mathbf{x}_2$,.. and $\mathbf{x}_n$, respectively: $\mathrm{d}p = \varrho_n^{\mathcal{S}}(\mathbf{x}_1, \mathbf{x}_2, .., \mathbf{x}_n)\mathrm{d}V_1\mathrm{d}V_2..\mathrm{d}V_n$. For a homogeneous and isotropic point process these quantities depend only on the differences of these positions, especially $\varrho_2^{\mathcal{S}}(\mathbf{x}_1, \mathbf{x}_2) = \varrho_2^{\mathcal{S}}(r)$, where $r = |\mathbf{x}_2 - \mathbf{x}_1|$.
Usual descriptors for the pure mark distribution are the (one–point) probability of finding the mark of a given point within the range[1] $[m, m + \mathrm{d}m]$: $\mathrm{d}p = \varrho_1^{\mathcal{M}}(m)\mathrm{d}m$. Unlike the spatial point process the mark distribution cannot be thought of as homogeneous in the most cases. Thus, not only the mark mean

$$\overline{m} = \int_{\mathbb{R}} \mathrm{d}m \; m\varrho_1^{\mathcal{M}}(m) \quad , \tag{4.1.1}$$

but also higher moments such as the mark variance

$$\mathbb{V}(m) = \int_{\mathbb{R}} \mathrm{d}m \, (m - \overline{m})^2 \, \varrho_1^{\mathcal{M}}(m) \tag{4.1.2}$$

and the skewness and kurtosis may be of interest. Using our empirical data set and assuming that it is a fair sample with respect to the marks[2], we can estimate the mark mean and mark variance by

$$\frac{1}{N}\sum_{i=1}^{N} M_i \quad \text{and} \quad \frac{1}{N-1}\left(\sum_{i=1}^{N} M_i^2 - N\left(\sum_{i=1}^{N} M_i\right)^2\right) \quad , \tag{4.1.3}$$

respectively. – Since point processes are defined via statistical ensembles, it is in principle possible that even non–trivial joint higher–order probabilities exist; more formally, e.g., the joint two–point probability density of finding two marks m_1 and m_2 at two galaxies within one realization of the point process, $\varrho_2^{\mathcal{M}}(m_1, m_2)$, may *not* factorize to give $\varrho_1^{\mathcal{M}}(m_1)\varrho_1^{\mathcal{M}}(m_2)$. In this case, however, it would not be possible to estimate the one–point properties of the pure mark distribution using one sample. From a physical point of view, it does not seem to be useful to assume that there exist different realizations with different mark properties. Formally, we can always shrink the ensemble in such a way that intrinsic mark correlations are not present. Thus, unless otherwise stated, we adopt the assumption that

$$\varrho_2^{\mathcal{M}}(m_1, m_2) = \varrho_1^{\mathcal{M}}(m_1)\varrho_1^{\mathcal{M}}(m_2) \tag{4.1.4}$$

[1] To simplify the formalism, we write down all formulae for the case of continuous marks $m_i \in \mathbb{R}$. It is straightforward to generalize this to the case of discrete or vector–valued marks. We also simplify our notation and speak somehow loosely of "finding a mark m" instead of "finding a mark within the range $[m, m + \mathrm{d}m]$" and similarity of "finding a point at position $\mathbf{x}$" instead of "finding a point within a volume $\mathrm{d}V$ centered on $\mathbf{x}$."

[2] I.e., the mark properties do not vary in space in a statistical sense, see below for further explanation.

and in a similar manner for higher–order quantities[3].
However, not only the distribution of the marks and the spatial clustering of the points, but also their interplay and their relations are of interest. Therefore, we have to move to joint space–mark probabilities.

Joint one–point measures Let therefore

$$\varrho_1^{\mathcal{S},\mathcal{M}}\left((\mathbf{x}_1, m_1)\right) \mathrm{d}V_1 \mathrm{d}m_1 \tag{4.1.5}$$

denote the probability of finding a point at position $\mathbf{x}_1$ with mark m_1. If we integrate $\varrho_1^{\mathcal{S},\mathcal{M}}$ over the whole mark space, we get the spatial probability density. We define a "mark–fair marked point process" via the factorization of the one–point density:

$$\varrho_1^{\mathcal{S},\mathcal{M}}\left((\mathbf{x}_1, m_1)\right) = \varrho_1^{\mathcal{S}}(\mathbf{x}_1)\varrho_1^{\mathcal{M}}(m_1) \quad . \tag{4.1.6}$$

This assumption states that each region in space in principle shows the same mark distribution. It neither presumes that the spatial distribution of the points is homogeneous, nor rules out that, e.g., in the central regions of clusters the mark distribution is biased; it only postulates that the properties of the mark distribution are *supervenient* on the spatial distribution of the points, i.e. systematic differences in the mark distribution are always accompanied and caused by a special spatial clustering. From a physical point of view, it is useful to adopt the assumption (4.1.6) even in cases where we do not presume spatial homogeneity[4].
A homogeneous marked point process (at the one–point level) is defined via

$$\varrho_1^{\mathcal{S},\mathcal{M}}\left((\mathbf{x}_1, m_1)\right) = \overline{\varrho}\varrho_1^{\mathcal{M}}(m_1) \quad . \tag{4.1.7}$$

where $\overline{\varrho}$ is a constant in space and estimated via $\frac{N}{|\mathcal{D}|}$.

Joint two–point measures Now consider the probability that we find two galaxies at positions $\mathbf{x}_1$ and $\mathbf{x}_2$ with marks m_1 and m_2, respectively:

$$\mathrm{d}p = \varrho_2^{\mathcal{S},\mathcal{M}}\left((\mathbf{x}_1, m_1), (\mathbf{x}_2, m_2)\right) \mathrm{d}V_1 \mathrm{d}V_2 \mathrm{d}m_1 \mathrm{d}m_2 \quad . \tag{4.1.8}$$

[3]Note, however, that there is a subtlety regarding the definition of the point process: so far, we did not specify whether the point process generates data within the whole space or only a part of it. In the first case, the assumption of intrinsic mark correlations does not seem to be useful, since other realizations of the point process are not accessible. On the other hand, one may understand different parts of space as different realizations of one point process. In this case the assumption of no intrinsic mark correlation is too strong, since it may be the case that, e.g. the Galactic south shows higher luminosities than the Galactic north. In other words, a large–scale inhomogeneity within the marks could generate intrinsic mark correlation, if we model two regions of space as independent realizations of one marked point process.

[4]Note, however, that in special cases, where we have, e.g., different cluster observations which are centered on the center of mass for each cluster and which are thought of as independent realizations of a marked point process, the assumption of mark–fairness may be problematic, e.g., when some of the galaxies which determine the center of mass are neglected later on.

The normalization of this two–point density is

$$\int_{\mathcal{D}}\int_{\mathcal{D}}\int_{\mathbb{M}}\int_{\mathbb{M}} \mathrm{d}V_1\mathrm{d}V_2\mathrm{d}m_1\mathrm{d}m_2\varrho_2^{\mathcal{S},\mathcal{M}}\left((\mathbf{x}_1,m_1),(\mathbf{x}_2,m_2)\right) = \mathbb{E}(N(N-1)) \equiv \mathcal{N}_2(\mathcal{D}) \quad , \tag{4.1.9}$$

where $\mathbb{E}$ denotes the expectation value and N the counting measure[5] for the window $\mathcal{D}$.
If we integrate over mark space, the pure spatial two–point density is regained:

$$\varrho_2^{\mathcal{S}}(\mathbf{x}_1,\mathbf{x}_2) = \int_{\mathbb{M}}\int_{\mathbb{M}} \varrho_2^{\mathcal{S},\mathcal{M}}\left((\mathbf{x}_1,m_1),(\mathbf{x}_2,m_2)\right)\mathrm{d}m_1\mathrm{d}m_2 \quad . \tag{4.1.10}$$

If the spatial part of the marked point process is homogeneous and isotropic, then $\varrho_2^{\mathcal{S}}(\mathbf{x}_1,\mathbf{x}_2)$ is only a function of the distance $r = |\mathbf{x}_2 - \mathbf{x}_1|$. – Equally, if we integrate twice over our sampling window $\mathcal{D}$, we get (up to a constant) the probability density of finding two marks m_1 and m_2 at two points within our sample:

$$\mathcal{N}_2(\mathcal{D})\varrho_{2,\mathcal{D}}^{\mathcal{M}}(m_1,m_2) = \int_{\mathcal{D}}\int_{\mathcal{D}} \varrho_2^{\mathcal{S},\mathcal{M}}\left((\mathbf{x}_1,m_1),(\mathbf{x}_2,m_2)\right)\mathrm{d}V_1\mathrm{d}V_2 \quad . \tag{4.1.11}$$

$\varrho_{2,\mathcal{D}}^{\mathcal{M}}(m_1,m_2)$ in principle depends on the sample; for $|\mathcal{D}| \to \infty$ it is supposed to converge to $\varrho_1^{\mathcal{M}}(m_1)\varrho_1^{\mathcal{M}}(m_2)$. We call a window $\mathcal{D}$ "mark–fair at the two–point level", if

$$\varrho_{2,\mathcal{D}}^{\mathcal{M}}(m_1,m_2) = \mathcal{N}_2(\mathcal{D})\varrho_1^{\mathcal{M}}(m_1)\varrho_1^{\mathcal{M}}(m_2) \quad . \tag{4.1.12}$$

Intuitively, this means, that the sample is large enough to contain typical pairs with marks m_1 and m_2 for the whole mark range.
For our purposes it is now useful to introduce *conditional mark probability densities*. We define

$$\mathcal{M}_2(m_1,m_2|\mathbf{x}_1,\mathbf{x}_2) \equiv \begin{cases} \frac{\varrho_2^{\mathcal{S},\mathcal{M}}((\mathbf{x}_1,m_1),(\mathbf{x}_2,m_2))}{\varrho_2^{\mathcal{S}}(\mathbf{x}_1,\mathbf{x}_2)} & \text{if } \varrho_2^{\mathcal{S}}(\mathbf{x}_1,\mathbf{x}_2) \neq 0 \quad , \\ 0 & \text{otherwise.} \end{cases} \tag{4.1.13}$$

$\mathcal{M}_2(m_1,m_2|\mathbf{x}_1,\mathbf{x}_2)\mathrm{d}m_1\mathrm{d}m_2$ gives the probability to find marks m_1 and m_2 at galaxies sitting at $\mathbf{x}_1$ and $\mathbf{x}_2$, respectively, under the condition that there are galaxies located at these positions[6].
For a *homogeneous and isotropic marked point process* (at the two–point level) we require that $\varrho_2^{\mathcal{S},\mathcal{M}}\left((\mathbf{x}_1,m_1),(\mathbf{x}_2,m_2)\right)$ and thus also $\mathcal{M}_2(m_1,m_2|\mathbf{x}_1,\mathbf{x}_2)$ are functions

[5]The counting measure counts the number of points within a fixed part of space (Daley & Vere-Jones 1988).

[6]Note, that the notation is somehow imprecise: since we require that m_1 is associated to the galaxy at $\mathbf{x}_1$ and correspondingly m_2 to the galaxy at $\mathbf{x}_2$, we should write: $\mathcal{M}_2(m_1|_{\mathbf{x}_1},m_2|_{\mathbf{x}_2}|\mathbf{x}_1,\mathbf{x}_2)$. For simplicity, however, we drop the subscript. The probability of finding a pair of galaxies with marks m_1 and m_2 located at $\mathbf{x}_1$ and $\mathbf{x}_2$, given that there is such a pair, is thus $2\mathcal{M}_2(m_1|_{\mathbf{x}_1},m_2|_{\mathbf{x}_2}|\mathbf{x}_1,\mathbf{x}_2)$ for $m_1 \neq m_2$.

of the galaxy separation $r = |\mathbf{x}_2 - \mathbf{x}_1|$, only. For our data analysis, we assume homogeneity and isotropy at the two–point level[7].
Now we can turn around this line of argument and ask for the opposite probability density of finding two galaxies at $\mathbf{x}_1$ and $\mathbf{x}_2$ within our sample given that these galaxies have the marks m_1 and m_2, respectively; it is given by

$$\mathcal{S}_2(\mathbf{x}_1, \mathbf{x}_2|m_1, m_2) \equiv \begin{cases} \frac{\varrho_2^{\mathcal{S},\mathcal{M}}((\mathbf{x}_1,m_1),(\mathbf{x}_2,m_2))}{\varrho_1^{\mathcal{M}}(m_1)\varrho_1^{\mathcal{M}}(m_2)} & \text{if } \varrho_1^{\mathcal{M}}(m_1)\varrho_1^{\mathcal{M}}(m_2) \neq 0 \\ 0 & \text{otherwise.} \end{cases} , \tag{4.1.14}$$

$\mathcal{S}_2(\mathbf{x}_1, \mathbf{x}_2|m_1, m_2)$ and $\mathcal{M}(m_1, m_2|\mathbf{x}_1, \mathbf{x}_2)$ are connected via Bayes' theorem:

$$\mathcal{S}_2(\mathbf{x}_1, \mathbf{x}_2|m_1, m_2)\varrho_1^{\mathcal{M}}(m_1)\varrho_1^{\mathcal{M}}(m_2) = \mathcal{M}(m_1, m_2|\mathbf{x}_1, \mathbf{x}_2)\varrho_2^{\mathcal{S}}(\mathbf{x}_1, \mathbf{x}_2) \quad . \tag{4.1.15}$$

Higher–order properties The n–point joint probability densities $\varrho_n^{\mathcal{S},\mathcal{M}}((\mathbf{x}_1, m_1), (\mathbf{x}_2, m_2), .., (\mathbf{x}_n, m_n))$ can be introduced as above. Again it is useful to factorize them into a conditional part and the pure spatial n–point density.

4.2 Mark segregation

Using these tools we can define mark segregation. The intuition behind all forthcoming definitions is that the spatial clustering depends on the marks, or vice versa. Mark segregation at the one–point level is simply the opposite of mark–fairness. It thus states that

$$\varrho_1^{\mathcal{S},\mathcal{M}}((\mathbf{x}_1, m_1)) \neq \varrho_1^{\mathcal{S}}(\mathbf{x}_1)\varrho_1^{\mathcal{M}}(m_1) \quad . \tag{4.2.16}$$

As discussed above, the assumption of no mark–fairness is not appropriate from a physical point of view. Thus mark–segregation at the one–point level is not to be expected and we adopt assumption (4.1.6) rather than (4.2.16). Note, that even work that compares the density distributions of different morphological classes such as (Santiago & Strauss 1992) does not test mark–segregation at the one–point level, since the local density is always estimated using more than one point.
However, at the two–point level mark–segregation is highly relevant. We speak of *mark–independent clustering* at the two–point level, if the factorization

$$\mathcal{N}_2(\mathcal{D})\varrho_2^{\mathcal{S},\mathcal{M}}((\mathbf{x}_1, m_1), (\mathbf{x}_2, m_2)) = \varrho_2^{\mathcal{M}}(m_1, m_2)\varrho_2^{\mathcal{S}}(\mathbf{x}_1, \mathbf{x}_2) \tag{4.2.17}$$

is valid; since we always adopt assumption (4.1.4), we can write

$$\mathcal{N}_2(\mathcal{D})\varrho_2^{\mathcal{S},\mathcal{M}}((\mathbf{x}_1, m_1), (\mathbf{x}_2, m_2)) = \varrho_1^{\mathcal{M}}(m_1)\varrho_1^{\mathcal{M}}(m_2)\varrho_2^{\mathcal{S}}(\mathbf{x}_1, \mathbf{x}_2) \quad , \tag{4.2.18}$$

[7]More precisely, we assume that $\mathcal{M}_2(m_1, m_2|\mathbf{x}_1, \mathbf{x}_2)$ is a function of m_1, m_2, and $r = |\mathbf{x}_2 - \mathbf{x}_1|$, only. We do not need any further assumptions. Therefore, our assumptions are weaker than the presumptions behind the standard analysis, where the mean density enters via the estimation of the two–point correlation function ξ, defined via $\varrho^{\mathcal{S}}(\mathbf{x}_1, \mathbf{x}_2) = \overline{\varrho}^2(1 + \xi(r))$.

too. If, on the contrary, $\varrho_2^{\mathcal{S},\mathcal{M}}((\mathbf{x}_1, m_1), (\mathbf{x}_2, m_2))$ does not factorize, we speak of mark segregation. In this case, the typical marks on pairs vary with the characteristics of the pair such as the pair separation. Note, that mark segregation at the two–point level is more than the opposite of mark fairness. Mark fairness refers to the whole sample, whereas mark segregation requires local information, e.g., on pairs with a given separation.
Mark segregation can also be characterized using the conditional mark probability density. If $\mathcal{M}_2(m_1, m_2|r)$ is a function of both marks m_1 and m_2, merely, we have mark–independent clustering. If, on the other hand, it is varying with r, we have mark segregation. Mark segregation is also visible in $\mathcal{S}_2(\mathbf{x}_1, \mathbf{x}_2|m_1, m_2)$: if it is varying with the marks, then mark segregation exists, otherwise it is simply $\varrho_2^{\mathcal{S}}(\mathbf{x}_1, \mathbf{x}_2)$, independent of the marks. For our purposes, however, it turns out that $\mathcal{M}_2(m_1, m_2|\mathbf{x}_1\mathbf{x}_2)$ is the most useful quantity.

Higher–order mark–segregation. The issue of mark segregation can be rediscussed at every statistical order. Note that it is possible that mark segregation does not appear until the nth order. Therefore, mark–independent clustering at the two–point level does not rule out mark segregation at higher orders. But of course it is appropriate to start from the second order, if we test empirical datasets on mark correlations.

Chapter 5

Statistical test quantities

The quantities employed for the definition of mark segregation are functions of several variables. For tests on mark segregation they are thus not appropriate. In this chapter we introduce a number of test quantities which are easy to handle and interpret (Sections 5.1 and 5.2). We illustrate their properties in Section 5.3 with an analytical example where the marks are constructed from a Poisson point process using the spatial distribution of the points.

5.1 Two–point quantities

The general idea to construct comprehensive test quantities is to integrate the conditional mark probability density $\mathcal{M}_2\left(m_1, m_2|\mathbf{x}_1, \mathbf{x}_2\right)$ over mark space weighting with functions of the marks. The results are *mark–weighted correlation functions*. We define a conditional mark average via

$$\langle f(m_1, m_2)\rangle_{\mathbb{M}^2}(r) \equiv \int_{\mathbb{M}}\int_{\mathbb{M}} \mathrm{d}m_1\mathrm{d}m_2 f(m_1, m_2)\mathcal{M}_2\left(m_1, m_2|r\right) \quad , \tag{5.1.1}$$

where $f(m_1, m_2)$ stands for any function of two marks. An analogous definition is possible at any statistical order.
The following weight functions are useful at the two–point level.

1. The mean mark:
$$k_m(r) \equiv \frac{1}{\overline{m}}\left\langle \frac{1}{2}\left(m_1 + m_2\right)\right\rangle_{\mathbb{M}^2} \quad . \tag{5.1.2}$$
If this function is varying with r, mark segregation is present. E.g., if $k_m(r) > 1$ at certain scales, galaxies with relative high marks tend to cluster at this scale.

2. The mark product can be introduced via:
$$k_{mm}(r) \equiv \frac{1}{\overline{m}^2}\left\langle m_1 m_2\right\rangle_{\mathbb{M}^2} \quad . \tag{5.1.3}$$

Again if k_{mm} varies with the pair separation r, mark segregation is present. Empirically, it is found that the behavior of k_m and k_{mm} is qualitatively similar.

3. The mark variogram is defined via:

$$\gamma(r) \equiv \frac{1}{\mathbb{V}(m)} \left\langle \frac{1}{2}(m_1 - m_2)^2 \right\rangle_{\mathbb{M}^2} \quad . \tag{5.1.4}$$

It is discussed, e.g., by Wälder & Stoyan (1997). A variogram $\gamma(r)$ which is not equal to one at a scale r indicates mark segregation.

4. Another useful statistics is the mark covariance:

$$\mathrm{cov}(r) \equiv \frac{1}{\mathbb{V}(m)} \left(\langle m_1 m_2 \rangle_{\mathbb{M}^2} - \langle m_1 \rangle^2_{\mathbb{M}^2} \right) \quad . \tag{5.1.5}$$

Deviations from zero supply evidence for mark segregation. The sign of the covariance tells us whether galaxies with high marks cluster exceptionally strongly with high–mark galaxies ($\mathrm{cov}(r) > 0$) or with low–mark galaxies ($\mathrm{cov}(r) < 0$).

5. The second–order weightings of the marks discussed so far mixed the properties of both marks; sometimes, however, it is useful to look at merely one mark. In this line of thought

$$\mathrm{var}(r) \equiv \frac{1}{\mathbb{V}(m)} \left\langle (m_1 - \langle m_1 \rangle_{\mathbb{M}^2})^2 \right\rangle_{\mathbb{M}^2} \quad . \tag{5.1.6}$$

quantifies the fluctuations of the marks of galaxies which are members of a pair with separation r in relation to the variance of the marks within the whole sample. We have, that

$$\mathrm{var}(r) = \gamma(r) + \mathrm{cov}(r) \quad . \tag{5.1.7}$$

6. Even higher–order statistics in mark space may be useful. The next two weighted correlation functions are the mark skewness and the mark kurtosis:

$$\mathrm{skew}(r) \equiv \frac{2 \langle m_1 \rangle^3_{\mathbb{M}^2} - 3 \langle m_1 \rangle_{\mathbb{M}^2} \langle m_1^2 \rangle_{\mathbb{M}^2} + \langle m_1^3 \rangle_{\mathbb{M}^2}}{S_3 \left(\mathbb{V}(m) \mathrm{var}(r) \right)^{\frac{3}{2}}} \quad , \tag{5.1.8}$$

where S_3 is the skewness of the whole mark distribution and

$$\mathrm{kurt}(r) \equiv \frac{-3 \langle m_1 \rangle^4_{\mathbb{M}^2} + 6 \langle m_1 \rangle^2_{\mathbb{M}^2} \langle m_1^2 \rangle_{\mathbb{M}^2} - 4 \langle m_1 \rangle_{\mathbb{M}^2} \langle m_1^3 \rangle_{\mathbb{M}^2} + \langle m_1^4 \rangle_{\mathbb{M}^2}}{S_4 \left(\mathbb{V}(m) \mathrm{var}(r) \right)^2} \quad , \tag{5.1.9}$$

where S_4 is the (Pearson) kurtosis of the whole sample. Mark segregation is present when these functions are varying with r.

7. Another statistics is Isham's correlation coefficient (Isham 1985)

$$\mathrm{cor}(r) \equiv \frac{\mathrm{cov}(r)}{\mathrm{var}(r)} \quad . \tag{5.1.10}$$

So far we focused on continuous marks; for most discrete marks similar definitions apply. However, for discrete marks which can not be mapped onto numbers such as morphological types we use conditional cross correlation functions. For the definition let $\{t_\alpha\}_{\alpha=1}^{A}$ denote the discrete labels or types. The conditional cross correlation functions are defined as

$$C_{\alpha\beta}(r) \equiv \langle f_{\alpha\beta}(m_1, m_2)\rangle_{\mathbb{M}^2} \tag{5.1.11}$$

with $\alpha, \beta \in \{1, .., A\}$ and the symmetric weight functions

$$f_{\alpha\beta}(r) \equiv \delta_{m_1 t_\alpha}\delta_{m_2 t_\beta} + (1-\delta_{\alpha\beta})\delta_{m_2 t_\alpha}\delta_{m_1 t_\beta} \quad , \tag{5.1.12}$$

where δ_{ij} denotes the Kronecker delta. Clearly,

$$\sum_{\alpha=1}^{A}\sum_{\beta=\alpha}^{A} C_{\alpha\beta}(r) = 1 \quad . \tag{5.1.13}$$

If mark segregation is present, these functions vary with r. For $\mathcal{M}_2(m_1, m_2|r) = \varrho_1^{\mathcal{M}}(m_1)\varrho_1^{\mathcal{M}}(m_2)$ the conditional mark correlation functions simply become $(1 - \delta_{\alpha\beta})q_\alpha q_\beta$, where q_α denotes the averaged fraction of galaxies with mark α.
It is also possible to construct discrete types from continuous marks through a binning. Such methods are related to common techniques where a sample is divided into several subsamples defined by mark ranges. Note, however, that even in this case, our method has advantages: First, we directly estimate the ratio of two correlation functions; usually one estimates two correlation functions and divides them; from a technical point of view, our approach is better. Secondly, we even look at cross correlations.
The division of the sample according to mark properties can be useful in many cases. However, the division of a sample often is ad hoc and not physically justified. It makes the sample and thus also the statistical significance of certain claims smaller; and, furthermore, even if mark segregation is present, it may not be the case, that significant mark segregation can be detected due to the artificial division of the sample. Thus, we suggest first to use our mark–weighted correlation functions. After mark segregation has been detected, a closer analysis with conditional cross–correlation functions with the binned marks may be useful.

Estimating mark–weighted correlation functions. Estimators for the mark–weighted correlation functions should both be unbiased and have a small variance. Different from the case of pure correlation functions, the mark–weighted correlation

functions can be estimated without boundary corrections without introducing a significant bias. The reason is mainly that mark–weighted correlation functions contain only *conditional* probability densities. The issue of how to estimate such two–point mark correlation functions is discussed in Beisbart & Kerscher 2000. Here we use the following estimators. For the mark mean, k_{mm} and the conditional cross correlation functions we take

$$\widehat{\langle f \rangle_{\mathbb{M}^2}}(r) = \frac{\sum_{i=1}^{N}\sum_{i\neq j=1}^{N} \mathbb{1}_{(\,-\Delta r/2, r-\Delta r/2]}(|\mathbf{X}_i - \mathbf{X}_j|) f(m_1, m_2)}{\sum_{i=1}^{N}\sum_{i\neq j=1}^{N} \mathbb{1}_{(\,-\Delta r/2, r-\Delta r/2]}} \quad . \tag{5.1.14}$$

as an estimator. For the variance and covariance, the denominator is reduced by one as usual. The mark skewness and kurtosis are estimated in a similar fashion using the k–statistics.
To quantify the statistical uncertainties we randomly reshuffle the marks of the points. This generates the realization of a marked point process with the same spatial clustering, but with no mark segregation. We repeat this procedure several times and compare the original mark correlation functions with the averaged results for the reshuffled marks. We plot the one–sigma region for the reshuffled marks and the real estimate of the mark correlation functions in a single diagram to assess the statistical significance of our claims. Possible physical errors are discussed below.

5.2 Higher–order quantities

Since it may be the case that mark segregation does not show up until the nth statistical order, it is useful also to have higher–order test quantities. Although we do not use the following functions in this work, we introduce here a number of higher–order test quantities.

nth order. First, one can focus on one statistical order and ask for possible mark correlations. For this we need weighting functions f_n which are in general functions of n marks, and an average over the mark space at the n–point level defined by:

$$\langle f_n(m_1, .., m_n)\rangle_{\mathbb{M}^n} \equiv \int_{\mathbb{M}} \mathrm{d}m_1 \cdots \int_{\mathbb{M}} \mathrm{d}m_n f(m_1, .., m_n)\mathcal{M}_n(m_1, .., m_n|\mathbf{x}_1, .., \mathbf{x}_n) \quad , \tag{5.2.15}$$

where for the case of homogeneity $\mathcal{M}_n(m_1, .., m_n|\mathbf{x}_1, .., \mathbf{x}_n)$ only depends on the distances between the points. The following functions are useful generalizations of the functions discussed above.

1. The mean mark:

$$k_m^n(r) \equiv \frac{1}{\overline{m}} \left\langle \frac{1}{n} \left(\sum_{i=1}^{n} m_i \right) \right\rangle_{\mathbb{M}^n} \quad . \tag{5.2.16}$$

2. The mark product:
$$k_{mm}^{n}(r) \equiv \frac{1}{\overline{m}^{n}} \left\langle \Pi_{i=1}^{n} m_i \right\rangle_{\mathbb{M}^n} \quad . \tag{5.2.17}$$

3. Using the well–known clustering–expansion, one can also generalize the mark covariance.

4. The mark variance
$$\mathrm{var}(r) \equiv \frac{1}{\mathbb{V}(m)} \left\langle (m_1 - \langle m_1 \rangle_{\mathbb{M}^n})^2 \right\rangle_{\mathbb{M}^n} \quad . \tag{5.2.18}$$
quantifies the fluctuations of the marks. Analogously, a mark skewness and a mark kurtosis can be introduced at the nth order.

Mixing all statistical orders. A mark–weighted J–function (van Lieshout & Baddeley 1996; van Lieshout & Baddeley 2000; Kerscher et al. 1998) can be defined. Within the Boolean grain method it is also possible to choose the radius of the Boolean grain according to inner properties of the objects represented by the points. The application of the Minkowski valuations results in mark–weighted Minkowski valuations.

5.3 Mark–weighted correlations for geometrical marks

In this section we illustrate the performance of the mark correlation functions using an analytical model. The base of this model is a Poisson point process; the marks for the points are constructed using the spatial clustering of the points in the following way: for each point, the number of neighbors $N(R)$ within a sphere with radius R around the point serves as the mark. Clearly, in this model mark segregation is built in by definition. The behavior of the mark variogram and k_{mm} was discussed by Wälder & Stoyan (1997), who calculated analytically the expectation values for these quantities.
In Figures 5.1 and 5.2 we show results of a simulation together with some analytical expectation values for the two–point quantities proposed in Section 5.1. We considered a Poisson process within a box $[-R, 1+R]^d$, where d is the spatial dimension, marks were assigned to the points using the number of neighbors as indicated above. To avoid a bias in the mark distribution due to the boundaries, we only consider the points within the unit box for our further investigations. The mark correlation functions were calculated using the estimator without boundary corrections. We consider the case of three dimensions and average over 5000 realizations to get the one–sigma fluctuations.
The results in Figure 5.1 show a strong signal for mark segregation in most of our

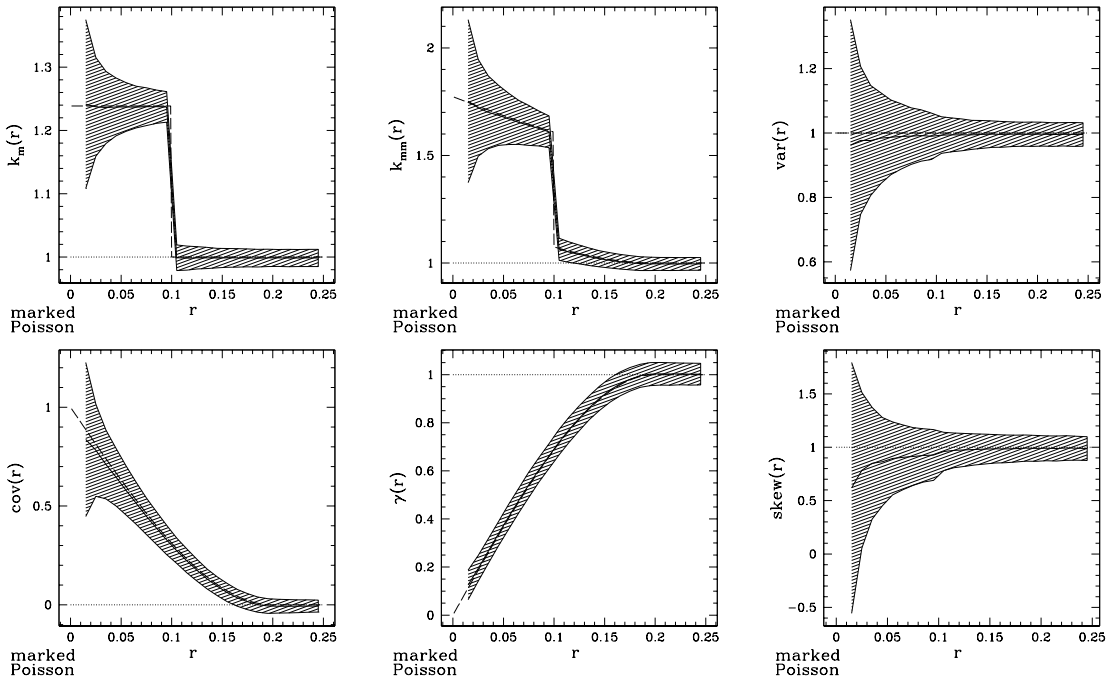

Figure 5.1: The mark–weighted correlation functions for a marked Poisson point process. The mark of a point at $\mathbf{x}_i$ is the number $N(R)$ of neighbors within a sphere of radius R around $\mathbf{x}_i$. Apart from the mark variance all mark–weighted correlation functions show mark segregation. The solid lines represent the results from a simulation in the unit box with a density of 1000 points and a radius of $R = 0.1$. The shaded areas are the 1σ ranges from these simulations. For the cases where analytical expectation values could be derived we show them with a long–dashed line. The dotted lines show the case of no mark segregation. We do not show the mark kurtosis, since its fluctuations are too large to allow definite claims.

test quantities. In more detail, the mean mark k_m is enhanced for points sitting on pairs with separations smaller than R. One can prove that

$$k_m(r) = \begin{cases} \frac{1+\overline{m}}{\overline{m}} & \text{for } r \leq R \quad , \\ 1 & \text{for } r > R \quad . \end{cases} \tag{5.3.19}$$

The result for k_{mm} is qualitatively very similar to k_m (this is valid also for higher moments like m^3).
However, the mark variance does not show mark segregation. Indeed, one can prove, that var equals strictly one for $r > 0$. This is an artifact of a Poisson process, where the presence of a pair does not enhance the probability of finding further points around them. The covariance shows a clear signal for mark segregation. Its positive sign tells us that, at small scales, points with higher marks cluster more strongly than the other points. This is clear since points with a high mark have by definition more neighbors than expected by the mean density: thus they cluster more strongly. A similar explanation is valid for the mark variogram γ: Points which are close together have at least a few of their neighbors with a distance smaller than R in common, thus these points tend to have similar values of the marks. The mark skewness shows a signal for mark segregation, too, which, however, has not yet been predicted theoretically. Note, that for radii $r > 2R$ no mark segregation is present any more for all of the test quantities. It is an advantage of our analysis that it unfolds the mark clustering in a scale–dependent way.
The conditional cross–correlation functions show a clear signal of mark segregation, too. They confirm our explanation that the points with higher marks cluster more strongly for scales smaller than $r < 2R$.

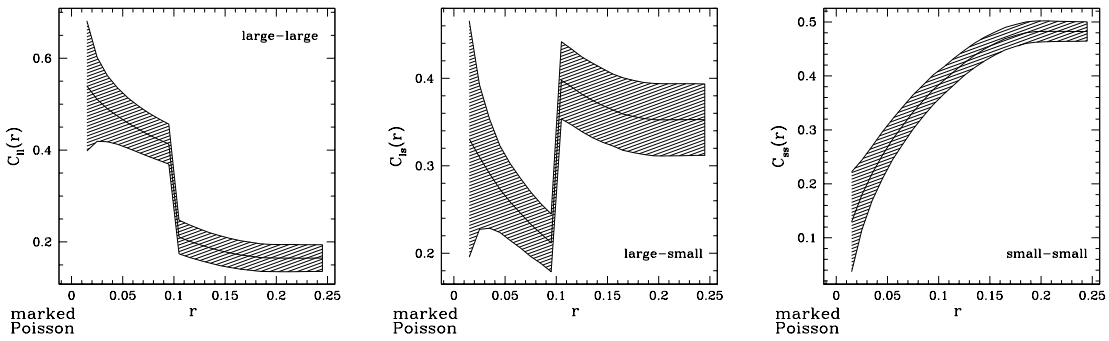

Figure 5.2: The conditional cross correlation functions for the marked Poisson process. For each realization of the marked point process, the sample was divided according to the values of the marks with respect to the median. C_{ll} are the correlations among points with the larger marks, C_{sl} cross correlations between points with large and the small marks, and accordingly C_{ss} the correlations among the points with small marks.

Chapter 6

Luminosity and morphology segregation in the SSRS 2 galaxy catalogue

The test quantities illustrated so far are now applied to real data, the Southern Sky Redshift Survey 2 (SSRS 2, for short, see da Costa et al. 1998). We address luminosity segregation in Section 6.1 and morphology segregation in Section 6.2 and interpret the observed signals in the light of two models, the random field model and the two–species model (Section 6.3).
The SSRS 2 galaxy catalogue contains more than 5000 galaxies in the southern part of the celestial hemisphere. It covers more than 1.7 sr of the sky and includes, apart from angular positions and redshifts, also morphological classifications and magnitudes within the B–band. The completeness is more than 99% for magnitudes < 15.5mag. We show the galaxies within a volume–limited subsample of the catalogue[1] together with their morphologies and luminosities in Figure 6.1. The visual impression tells us that the early–type galaxies are more clustered than the late–type galaxies. But is there really significant morphology or luminosity segregation within the SSRS 2 catalogue?

6.1 Luminosity segregation

We start with a volume–limited sample of $100h^{-1}$Mpc depth with 1179 galaxies. The redshifts were converted into real distances r_i, first simply applying Hubble's law. The luminosities L_i are estimated using the distance r_i of the galaxy and its magnitude mag_i via $L_i = r_i^2 10^{-0.4\mathrm{mag}_i}$. Note that an absolute calibration of the luminosities is not necessary in our case.
Results for the mark–weighted two–point correlation functions are shown in Fig-

[1]The volume–limited subsamples were constructed by M. Kerscher. He also did the K–corrections and the conversion into luminosity distances used later on.

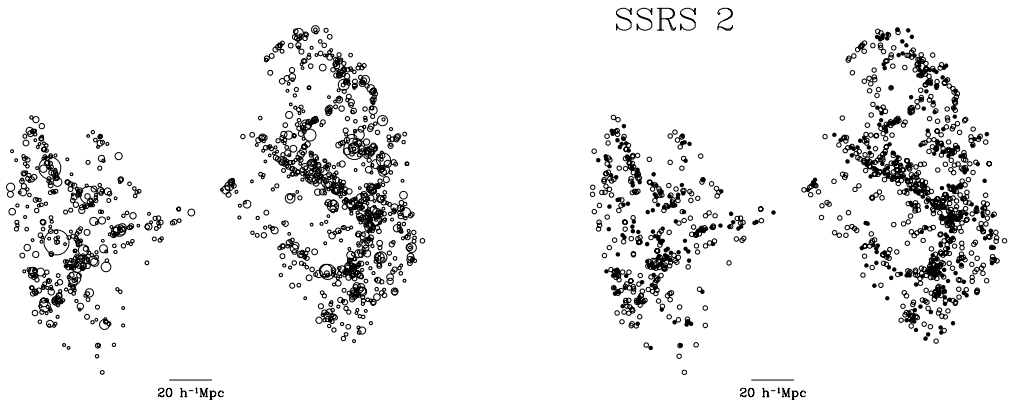

Figure 6.1: The SSRS 2 galaxy catalogue. We show a volume–limited sample of $100h^{-1}$Mpc depth. For the left panel, the radius of a circle representing a galaxy is proportional to its luminosity. In the left panel, filled circles indicate early–type galaxies, the empty circles late–type galaxies. The magnitudes are K–corrected, the distance is the luminosity distance for an Einstein–de Sitter universe.

ure 6.2. A clear signal for luminosity segregation is evident in all of the test quantities. Our scale–dependent analysis shows that the luminosity segregation extends to scales up to $\sim 15h^{-1}$Mpc. Furthermore our claims are statistically significant as can be seen from the 1σ bars for the randomized marks.
In more detail, k_m (not shown) and k_{mm} are positive for distances up to $\sim 10h^{-1}$Mpc. This tells us that the luminous galaxies tend to cluster more strongly than the dim ones. This confirms earlier results (Park et al. 1994; Benoist et al. 1996), but now in a statistically significant way. The signal of var and the very weak signal of the covariance escaped previous analysis, since these quantities rely on higher–order statistics of the marks. The signal of var means that the luminosity variations are enhanced on small scales, too; galaxies which are sitting on a pair have on average more fluctuating luminosities than isolated galaxies. In part, this effect may be due to galaxy clusters, where galaxies of different sizes and therefore luminosities are close together. But note, that the signal extends to scales of $\sim 14h^{-1}$Mpc, thus, it cannot be simply caused by clusters of galaxies. Unfortunately, the skewness and the kurtosis (not shown) do not yield significant indications for luminosity segregation. The reason is that higher–order quantities have higher variances. – We tested also different binnings, and found that the results are stable.
To strengthen our results and to probe the effect of the K–corrections(Benoist et al. 1996), we also investigate a volume–limited sample of again $100h^{-1}$Mpc, where the distances were estimated using the luminosity distance for the case of an Einstein–de Sitter universe (now we have 1320 galaxies). Results are shown in Figure 6.3. They

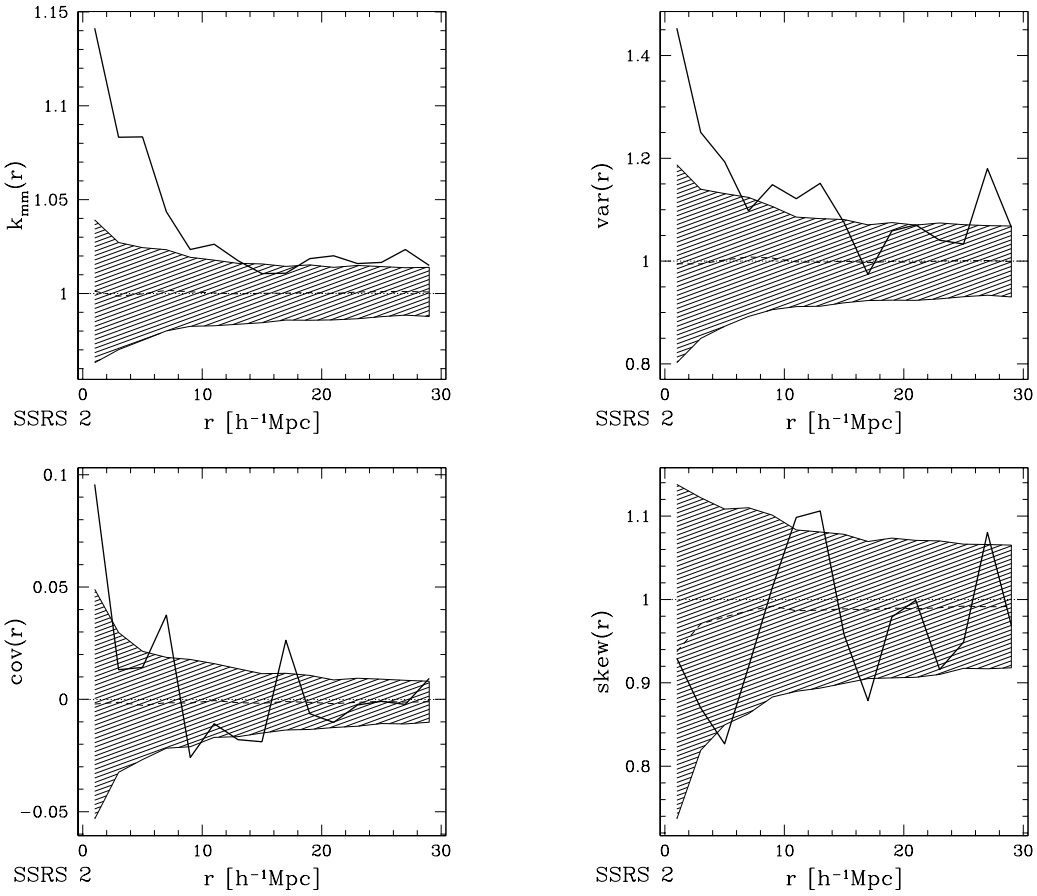

Figure 6.2: Some of the mark–weighted correlation functions for the SSRS 2 catalogue. The solid lines are the results for the mark correlation functions, the dashed lines and the shaded areas indicate the expectation values and the 1σ fluctuations for the same data, but with randomized marks. The dotted lines marks the case of no mark segregation

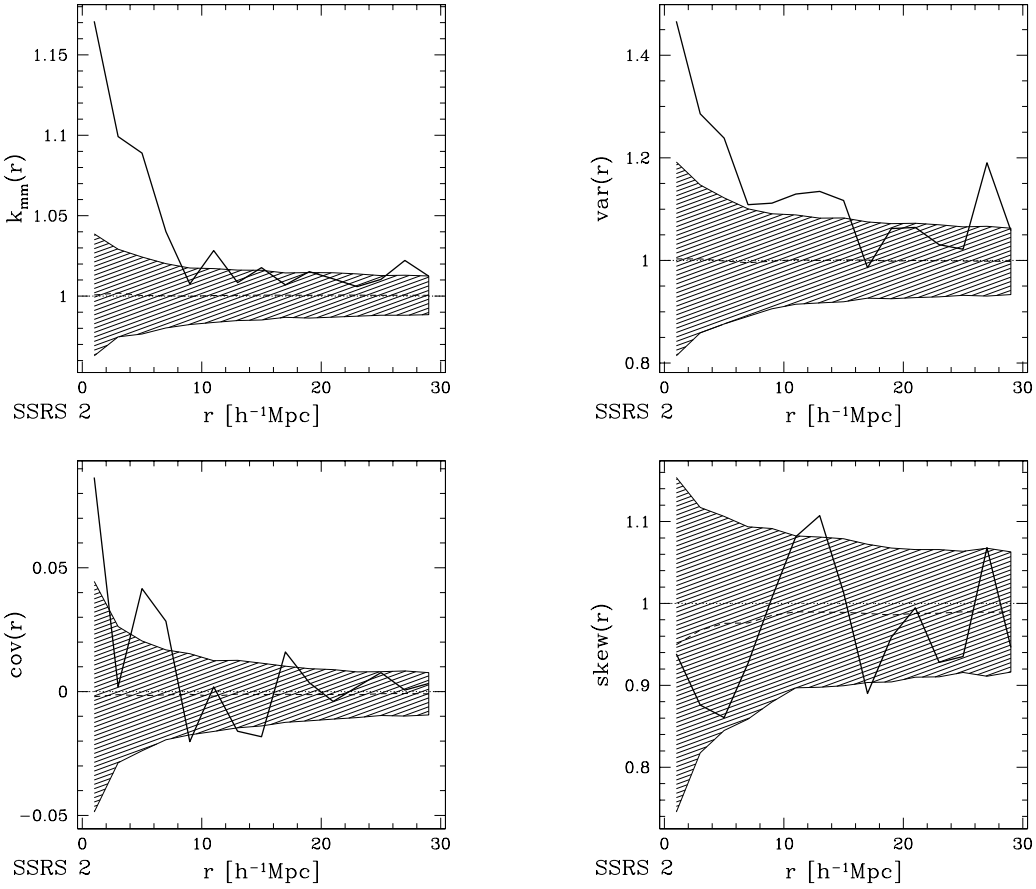

Figure 6.3: Some of the mark–weighted correlation functions for the SSRS 2 catalogue (here we use K–corrected magnitudes and luminosity distances). The solid l

confirm in general the clear signal for luminosity segregation, although the signal is going down at larger scales.
To investigate more closely which galaxies are responsible for the luminosity segregation present in the SSRS 2 catalogue we divide our sample (with the K–corrected luminosities) further. First, we estimate the conditional cross–correlation functions. We divide our sample into three subsamples according to luminosity. The cuts are chosen in such a way that the subsamples are (roughly) equally large. The results in Figure 6.4 confirm the significant luminosity segregation and show that the bright galaxies cluster more strongly than the dim ones.
So far, we only discussed the statistical errors, but there are further uncertainties to be expected. In particular the peculiar velocities of the galaxies do not only affect the redshifts of the galaxies, but also the estimate of the luminosity. Uncertainties within the measurement of the redshift may have the same effect, but are much smaller.

In Beisbart & Kerscher 2000, however, it is shown that such errors do not affect our results. Random peculiar velocities are given to the points in accordance with the pairwise velocity dispersion observed in the SSRS 2 galaxy catalogue (Marzke et al. 1995). On average, the results for our test quantities do not change. Even if the statistical errors and the physical uncertainties are added up, a significant signal for luminosity segregation is still recognizable.

6.2 Morphology segregation

We test for morphology segregation using the $100h^{-1}$Mpc volume–limited sample with the corrected luminosities. Since the determinations of the morphological types are affected by uncertainties, it is useful to have large morphological classes, only. From the T–types we construct early– and late–type galaxies (T–type ≤ 0 and T–type ≥ 1), where the early–type galaxies comprise mainly elliptical galaxies, whereas late–type galaxies are spirals and SOs. Galaxies without classification are discarded[2].

Results are shown in Figure 6.5. There is a significant signal for morphology segregation. The early–type galaxies are more strongly clustered than the other galaxies on average at the expense of the late–type galaxies. The cross correlations show a significant signal, too.

6.3 Understanding mark segregation

After having shown that there is a significant luminosity and morphology segregation within the SSRS 2 galaxy catalogue, we want to understand the physical meaning of the signal. We do so by comparing to analytical models. The first one, the random field model, is inspired by mathematical theory, the second one extends the well–known morphology density relation found by Dressler (1980) to larger scales ("two–species model").

6.3.1 The random field model

The random field model is not simply a particular model, but covers a large class of models. Within this class, the marks on the points trace a random field independent of the points. More precisely, we have a purely spatial point process and a random field f independent of the point process. For each realization of the point process $\{\mathbf{x}_i\}_{i=1}^N$, the marks m_i are assigned to the points according to

$$m_i = f(\mathbf{x}_i) \quad , \tag{6.3.1}$$

[2]In our case, only one galaxy lacks classification.

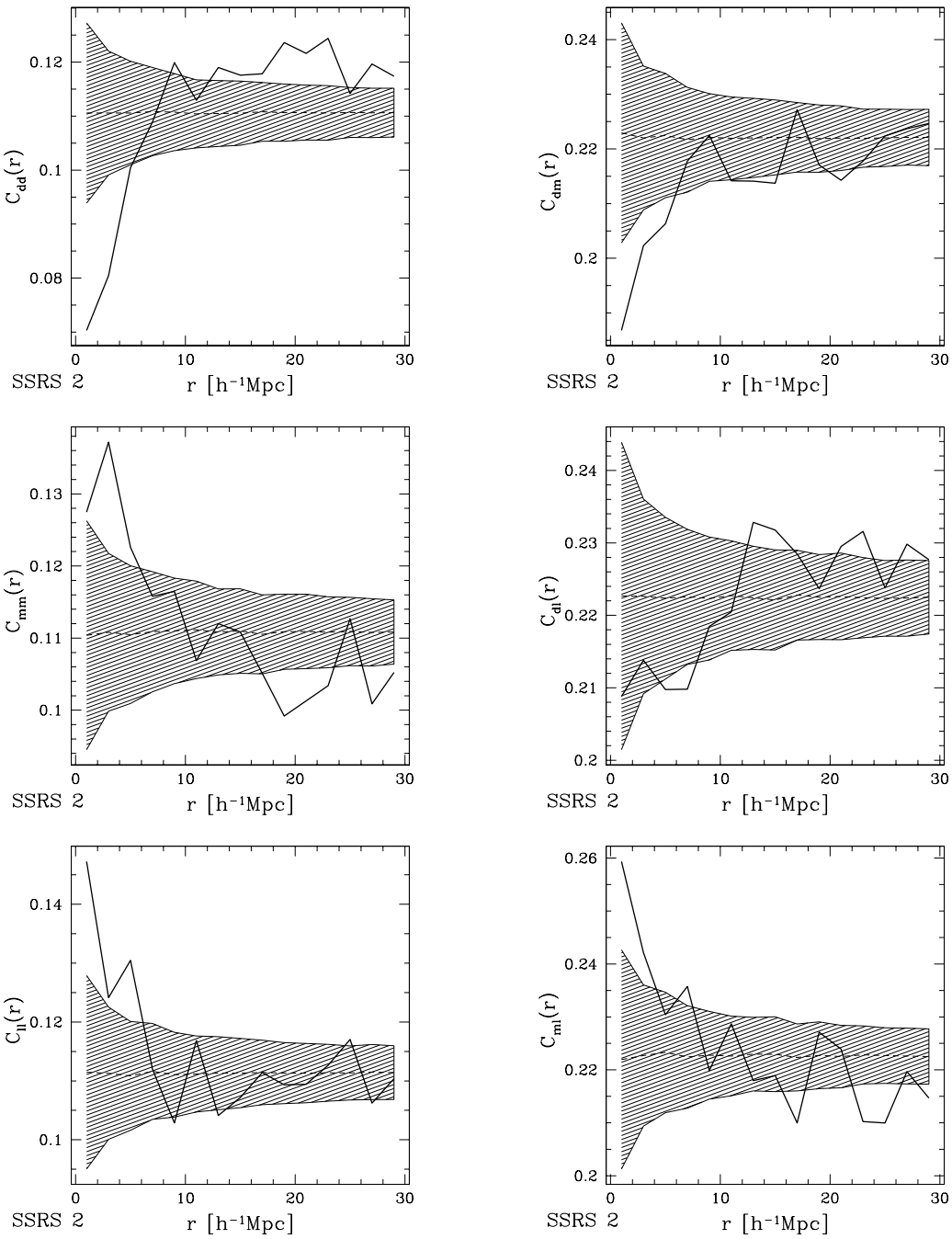

Figure 6.4: The conditional cross correlation functions for the SSRS 2 catalogue according to luminosity.

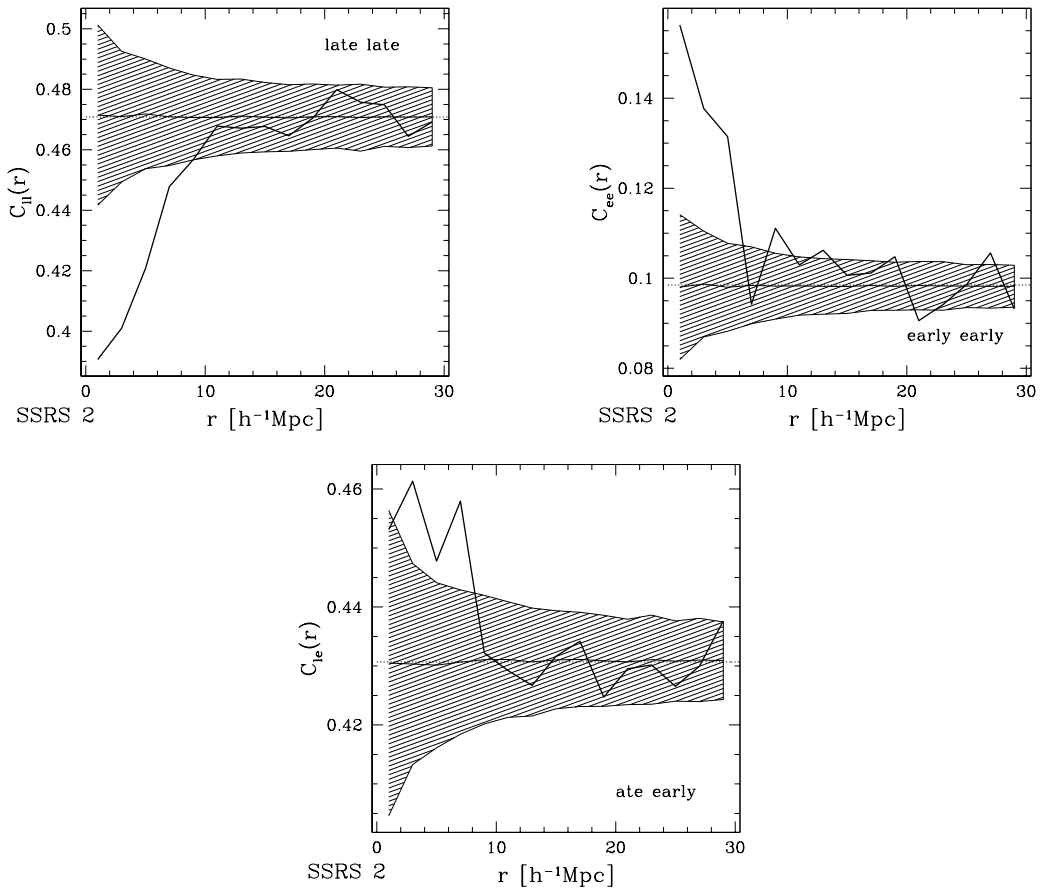

Figure 6.5: The conditional cross correlation functions for the SSRS 2 catalogue according to morphology.

where f is a realization of the random field. If f has autocorrelations, then mark segregation will be found. To put it in other words, if the random field model is valid, we can sample a luminosity field by the galaxies in an unbiased way (see Chapter 2.1). If the random field model is not applicable, our sampling does not trace the true luminosity field. In this context, the random field model is applied in geostatistics (Cressie 1991).
Wälder & Stoyan (1996) derived a constraint equation for the mark variogram γ for the case of the random field model. They assume homogeneity and isotropy. In this case the mean mark and the mark variance are given by

$$\overline{m} = \mathbb{E}\left(f(\mathbf{0})\right) \quad \text{and} \quad \mathbb{V}(m) = \mathbb{E}\left(f(\mathbf{0})f(\mathbf{0})\right) - \mathbb{E}\left(f(\mathbf{0})\right)^2 \quad , \tag{6.3.2}$$

respectively, where $\mathbb{E}$ indicates the ensemble average for the random field. Furthermore, the mark variogram and k_{mm} can be calculated via

$$\mathbb{V}(m)\gamma(r) = \frac{1}{2}\mathbb{E}\left(\left(f(\mathbf{0}) - f(\mathbf{r})\right)^2\right) = \mathbb{E}\left(f(\mathbf{0})^2 - f(\mathbf{0})f(\mathbf{r})\right) \quad \text{and} \tag{6.3.3}$$

$$k_{mm}(r) = \frac{1}{\overline{m}^2}\mathbb{E}\left(f(\mathbf{0})f(\mathbf{r})\right) \quad , \tag{6.3.4}$$

respectively. Here, $\mathbf{r}$ denotes any point at a distance r from the origin. Obviously, there is an analytical connection between the mark variogram and k_{mm} for this model:

$$\mathbb{V}(m)\gamma(r) = \mathbb{V}(m) + \overline{m}^2 - \overline{m}^2 k_{mm}(r) \quad . \tag{6.3.5}$$

In Figure 6.6 we test this constraint equation empirically for the SSRS 2 data in comparing the right hand side of Equation 6.3.5 to its left hand side. As one can see, the random field model is completely out of discussion. The galaxies in the SSRS 2 catalogue thus do not simply trace an independent luminosity field, but rather interact with the spatial clustering of the points. This is also physically expected and has consequences for the modeling of the bias.

6.3.2 The two–species model

Since both luminosity and morphology segregation are present in the SSRS 2 galaxy catalogue, we can ask whether both kinds of segregation are connected with each other. For instance, one could try to explain the luminosity segregation in terms of the morphology segregation in the following way: The elliptical galaxies are more clustered than the spiral ones; since the luminosity is differently distributed for both morphological types, this causes a luminosity–dependent clustering.
We generalize this idea in terms of a two–species model – a homogeneous and isotropic marked point process with mean spatial density $\overline{\varrho}$. Within this model there exist two subpopulations or species (labelled e and l) of galaxies. Their relative fractions are q_i, their mean marks are $\overline{m}_i$ for $i \in \{e, l\}$. Within each subpopulation we have spatial two–point densities $\overline{\varrho}^2 q_i^2 g_i(r)$; the cross correlations (more precisely the probability

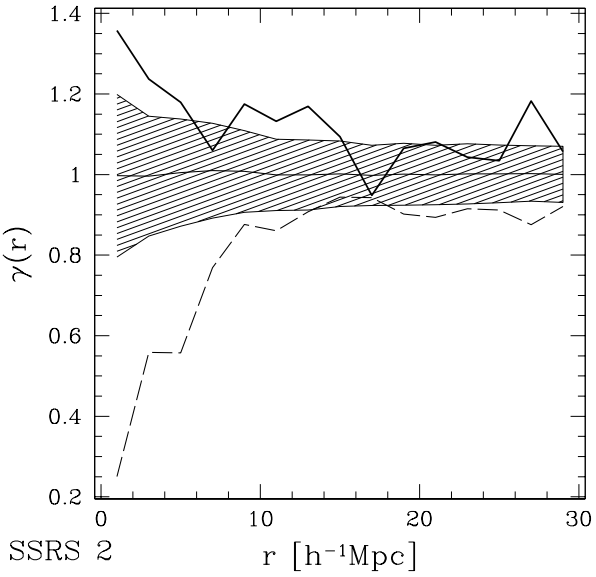

Figure 6.6: A comparison between γ for the SSRS 2 catalogue (solid line) and the prediction of the random field model (dashed line). We used the sample without the K–corrections.

density of finding one galaxy of type e at $\mathbf{x}_1$ and another galaxy of type l at $\mathbf{x}_2$, where $r = |\mathbf{x}_1 - \mathbf{x}_2|$) are denoted by $\overline{\varrho}^2 q_e q_l g_{el}(r)$. No intrinsic mark correlations exist for each subpopulation. Thus, the two–species model is a simple model, where mark correlations are generated by the interplay of two subpopulations which themselves show no mark segregation.
Using this model, we can easily calculate k_{mm} and the other test quantities used so far. For instance, we get for k_{mm}:

$$k_{mm}(r) = \frac{1}{g(r)} \left(\overline{m}_e^2 q_e^2 g_e(r) + 2\overline{m}_e \overline{m}_l q_e q_l g_{el}(r) + \overline{m}_l^2 q_l^2 g_l(r) \right) \quad , \tag{6.3.6}$$

where

$$g(r) = q_e^2 g_e(r) + 2 q_e q_l g_{el}(r) + q_l^2 g_l(r) \quad . \tag{6.3.7}$$

Now we can take $\overline{m}_i$, q_i and the functions $g.$ as fitting parameters and try to reproduce our test quantities using this model. This procedure may be appropriate if we do not know the species generating the luminosity segregation exactly. In our case, however, where the morphological types are known, it is more intelligent to *estimate* the $\overline{m}_i$, q_i and the functions $g.$ from the data and to compare with the observed test quantities.
This is done in Figure 6.8, where we compare the k_m and var for the two-species

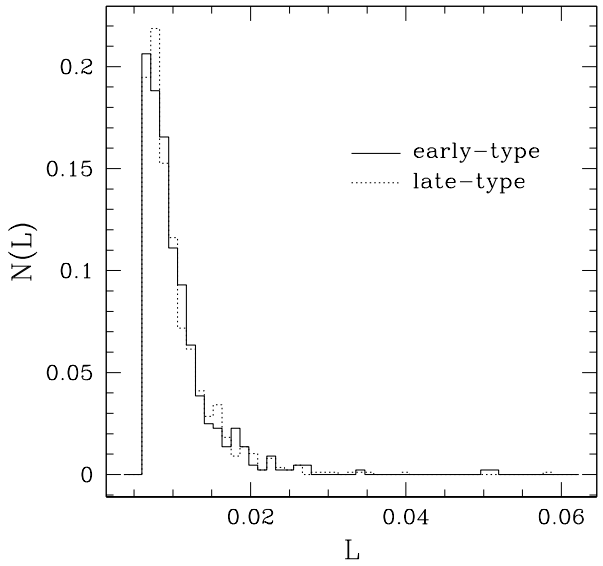

Figure 6.7: The distribution of the luminosities (in arbitrary units) for the early–type galaxies (solid line) and the late–type galaxies (dotted line).

model and the real data[3]. Since the luminosity distributions are very similar for both the early type and the late type galaxies (see Figure 6.7), the theoretical prediction of the two–species model is very close to one. The real observed luminosity segregation thus can not be explained in terms of the two–species model. This means in particular that the luminosity segregation observed within the data is more than an effect of the morphology–density relation (Dressler 1980).
We can strengthen this conclusion by looking at the early–type and the late–type galaxies separately. For each type of galaxy we calculate the mark correlation functions. Some results are compared in Figure 6.9. One can see that for both subclasses there is still significant luminosity segregation. This again falsifies the two–species model, since within this model, no mark correlations are expected if one restricts oneself to one galaxy type.

The other way round? Although the luminosity segregation is not generated by morphology segregation in the sense of the two–species model, it may be the case that luminosity segregation causes morphology segregation. Although this hypothesis seems rather unlikely since the luminosities seem to be similar for both morphological types (see Figure 6.7), we test this hypothesis by comparing subsamples of our catalogue defined by luminosity and divide the SSRS 2 according to the

[3]The g. were calculated by M. Kerscher using the Ohser estimator (Kerscher 1999).

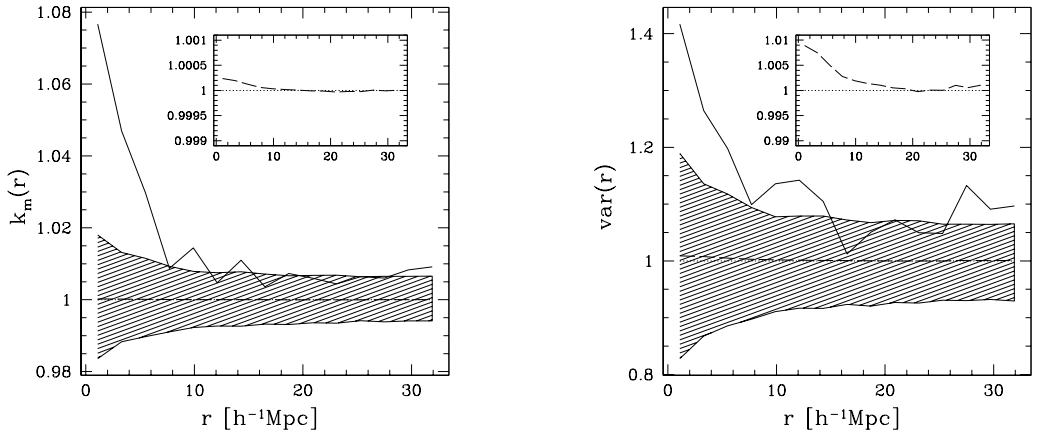

Figure 6.8: The predictions of the two–species model for the luminosity segregation (dashed line) together with the real observations (solid line). Since the predictions of the two–species model are very close to one, we show them in the inset. As above, the shaded area is the 1σ–region from randomized marks; the dotted line indicates the case of no mark segregation.

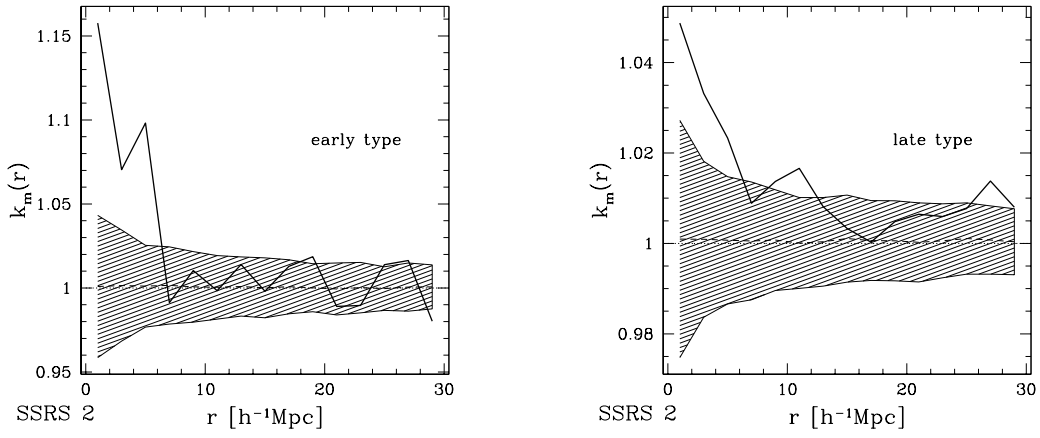

Figure 6.9: The luminosity correlation function $k_m(r)$, but now only for the early–type galaxies (left panel) and the late–type galaxies (right panel).

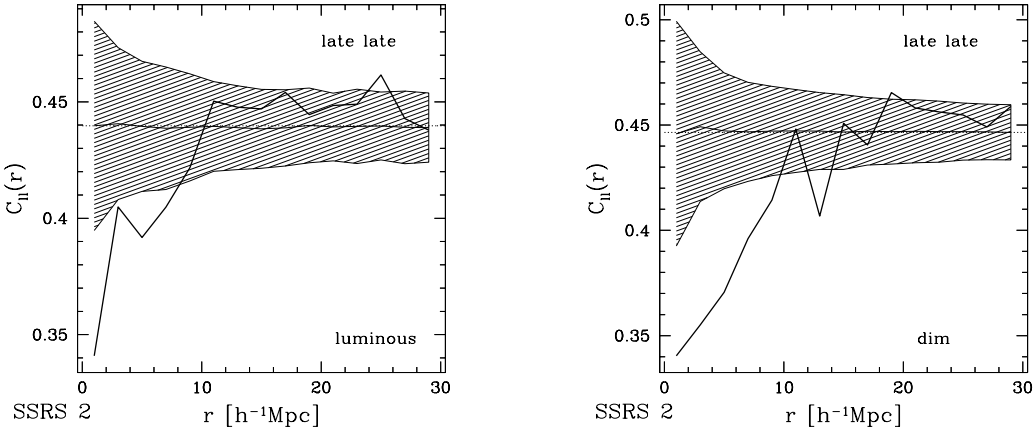

Figure 6.10: The conditional cross correlation function $C_{ll}(r)$ (late–type late–type), but now only for the luminous galaxies (left panel) and the dim galaxies (right panel).

luminosity median[4]. Both subsamples are investigated using the conditional cross correlation functions. Results can be seen from Figure 6.10; in both subsamples a significant signal for morphology segregation can be seen. We thus conclude that both types of marks (the luminosity and the morphology) are *irreducible* to each other: Neither of them can be explained with the aid of the other one in the spirit of the two–species model.

[4]Note, however, that this division is somehow arbitrary and may obscure a possible physical division of the sample.

Chapter 7

A framework for the bias description

Marked point processes provide a useful framework for modeling and describing the bias. We exemplify this by showing to what extent volume– and flux–limited samples trace the true physical correlations (Section 7.1). We summarize our results and give further prospects in Section 7.2.

7.1 Volume– and flux–limited samples

For the following it is useful to consider a number of marks for each galaxy. Formally we construct a compound mark m consisting of the line–of–sight peculiar velocity u and the luminosity L of a galaxy: $m = (u, L)$. For simplicity, we constrain ourselves to the case of an Euclidian geometry; generalizations to curved spaces are possible. We focus on one– and two–point properties.
Let $\varrho_1^{\mathcal{S},\mathcal{M}}(\mathbf{x}, u, L)$ denote the one–point probability density for finding a galaxy with luminosity L and line–of–sight peculiar velocity u at proper position $\mathbf{x}$ with distance $r = |\mathbf{x}|$. It is useful to parameterize the positions by two angular coordinates, e.g. right ascension α and declination δ, and distance r. What is happening if we observe the window $\mathcal{D}$ in a magnitude–limited way or if we construct volume–limited samples?
At this point it is useful to introduce *secondary* or *apparent* qualities, which do not merely reflect intrinsic properties of the objects under consideration, but rather are generated by the interplay of the observational limitations and the true physical properties. In this line of thought we move to redshift space and introduce the estimated distance r' and the estimated luminosity L'. Formally, we have a mapping

between the true and the apparent qualities:

$$\chi : \begin{pmatrix} r \\ \alpha \\ \delta \\ L \\ u \end{pmatrix} \mapsto \begin{pmatrix} r' \\ \alpha' \\ \delta' \\ L' \\ u' \end{pmatrix} = \begin{pmatrix} \left(H_0 r + u\right)/H_0' \\ \alpha \\ \delta \\ \frac{\left(r+\frac{u}{H_0'}\right)^2}{(r)^2} L \\ u \end{pmatrix} \tag{7.1.1}$$

where H_0 is the value of the present–day Hubble constant[1], and H_0' the assumed Hubble constant. The secondary qualities are assumed to be a realization of a second point process. We have a mapping between both point processes which maps each realization of the original point process to the secondary one. Mostly, no estimate of the peculiar velocity is accessible. Thus we have to integrate over the peculiar velocity. This generates a degeneracy. Since the values of the angles α and δ are not affected by the transformation to redshift space, we do not consider them from now on. For the joint one–point densities we have that

$$p(r, L, u)\mathrm{d}r r^2 \mathrm{d}L \mathrm{d}u = p(r', L', u')\mathrm{d}r'(r')^2 \mathrm{d}L' \mathrm{d}u' \quad . \tag{7.1.2}$$

– Within a flux–limited sample with flux limit ϕ_l, one observes all galaxies i with $L_i > 4\pi\phi_l r_i^2$. The observed joint one–point probability density is thus

$$\varrho_1^{\mathcal{S},\mathcal{M},\prime}(r', L')\mathrm{d}r'(r')^2\mathrm{d}L' = \int_{\mathbb{R}} \mathrm{d}u' p(r', L', u')\mathrm{d}r'(r')^2\mathrm{d}L' = \int_{\mathbb{R}} \mathrm{d}u p(r, L, u)\theta(L - \phi_l 4\pi r^2)\mathrm{d}r r^2 \mathrm{d}L \quad , \tag{7.1.3}$$

where $(r, L, u) = \chi^{-1}(r', L', u')$. Although $u = u'$, the transformation depends on the value of u. – To avoid inhomogeneous selection criteria, one usually moves to volume–limited subsamples: one chooses a luminosity L_l' and a limiting depth r_l' in such a way that $\phi_l < L_l'/(r_l')^2$. Only galaxies with $r' < r_l'$ and $L' > L_l'$ are admitted to the sample. For the one–point densities this means:

$$\varrho_{L_l', r_l', 1}^{\mathcal{S},\mathcal{M},\prime}(\mathbf{x}', L') = \theta(r_l' - r')\theta(L_l' - L')\varrho_1^{\mathcal{S},\mathcal{M},\prime}(r', L') \quad . \tag{7.1.4}$$

Equations (7.1.3) and (7.1.4) show, that even if the original point process is mark–fair, i.e. the one–point joint probability factorizes, this does not need to be the case for the derived point process. For usual geometries of large–scale structure surveys, for each shell more galaxies are scattered into the shell from larger radii than from smaller ones. On average, these galaxies must have larger luminosities to be observed

[1]Relativistic distance–redshift relations as well light–cone effects can easily be included within this formalism.

within the flux–limited sample. Since we underestimate their luminosities via their apparent distances, this can result in a bias.
Similar considerations apply to higher–order quantities. To simplify the following formulae, we assume as an idealization that the peculiar velocities are not relevant, i.e. the probability density for the peculiar velocity factorizes out and is simply $\delta^D(u)$, where δ^D denotes the Dirac delta. In this case, $r = r'$ and $L = L'$, we have only to handle the bias due to the flux limit. For a homogeneous and isotropic point process, the spatial two–point quantities estimated are then simply:

$$\int \varrho^{\mathcal{S}}_{L_l,r_l,2}(\mathbf{x}_1,\mathbf{x}_2) = \int \mathrm{d}L_1 \int \mathrm{d}L_2 \varrho_2^{\mathcal{S},\mathcal{M}}((m_1,\mathbf{x}_1),(\mathbf{x}_2,m_2)) \quad . \tag{7.1.5}$$

In general, $\varrho^{\mathcal{S}}_{L_l,r_l,2}$ equals the true two–point density only if no mark segregation is present. Having a model for the mark–segregation, we can show, how volume–limited subsamples are biased. Similarly, one can try to predict how mark segregation influences estimates of the angular correlation function (Gardini et al. 1999). – Mappings between point processes are thus a useful framework to handle the bias in large–scale structure surveys.

7.2 Summary and outlook

Marked point processes are a useful framework to handle mark segregation and the bias problem. This framework allowed us to clarify the notion of mark segregation at any statistical order and to introduce test quantities, with the aid of which we can test whether mark correlations are to be found within empirical data sets. The mathematical theory is a solid foundation for further constructions. In particular, we can define estimators and ask the question of their (ratio–)unbiasedness. Moreover, we can assess the statistical significance of claims regarding mark segregation. Even from a technical point of view, our method has many advantages: All measures can be applied to one sample, it is no longer necessary to construct subsamples via the marks. Our analysis is scale–dependent and furthermore in principle also applicable to inhomogeneous point sets.
Applying these measures to the SSRS 2 galaxy catalogue, we showed that there are both significant luminosity and morphology segregation. The theoretical framework allowed us to ask a further question: what is the observed mark segregation like? The random field model is completely unable to fit the data, even a two–species model that explains the luminosity segregation in terms of a morphology–dependent clustering, is not compatible with the data.
This shows that a number of things remain to be done. A main line of thought may be the search for realistic models. A first step could be to calculate our test quantities for the Gaussian peak formalism (Bardeen et al. 1986). Also the application to semianalytical models would be interesting. Mark correlation functions could also be a tool to uncover the structure of microwave background maps, compare Heavens

& Sheth 1999. It seems also fruitful to model the bias in terms of mark correlations, since mark correlations put an intermediate step in between the pure clustering of points and a realization of a random field (the density).
From a more observational point, the physical picture of luminosity segregation has to be complemented. So far, various tools have been used to look for mark segregation, but the variety of tools obscured the view on the physical things going on. An application of the mark correlation functions showed, that in the PSCz survey no significant luminosity segregation can be detected (Beisbart & Kerscher 2000; Szapudi et al. 2000). Further samples have to be investigated to get a complete picture of how the clustering varies with the inner properties of the galaxies. Such a complete picture could deepen our understanding on the processes enlightening the galaxies.

Appendix

Appendix A

Some more words on Minkowski valuations

The general transformation rules for the second–rank tensors under translations (represented by a translation vector $\mathbf{t}$) are:

$$\begin{aligned} M^2(\mathbf{t}+A) &= M^2(A) + 2\mathbf{t}M^1(A) + \mathbf{t}\mathbf{t}M^0(A) \quad , \\ M_{i,j,0,2}(\mathbf{t}+A) &= M_{i,j,0,2}(\mathbf{t}+A) + 2\mathbf{t}M_{i,j,0,1}(A) + \mathbf{t}\mathbf{t}M_{i,j,0,0}(A) \quad , \\ M_{i,j,1,1}(\mathbf{t}+A) &= M_{i,j,1,1}(A) \quad , \\ M_{i,j,2,0}(\mathbf{t}+A) &= M_{i,j,2,0}(A) \end{aligned} \tag{A.1}$$

for $i \in \mathbb{N}$ and $j = 0, .., (d-1)$.

A.1 The Crofton formulae and the computation on a grid

A.1.1 The Crofton formulae

The characterization theorem is the core of integral geometry and allows us to get a number of integral geometric formulae. The recipe for deriving such formulae is very simple: write down a motion–equivariant, continuous and additive functional and expand it in one of the bases for the Minkowski valuations.
One set of such formulae are the Crofton formulae. If we intersect a pattern with an i–dimensional hyperplane $\mathcal{E}_i$ and sum up the Minkowski valuations M of all such intersections, we get again a Minkowski valuation:

$$\int \mathrm{d}\mathcal{E}_i M(A \cap \mathcal{E}_i) \quad . \tag{A.2}$$

To write down and to prove the Crofton formulae it is convenient to change the basis of the Minkowski valuations. We define:

$$\begin{aligned} W^{q,r} &\equiv W^{q,r} \quad , \\ W_{i,j,k,l} &\equiv \frac{1}{(j+1)\binom{d}{j+1}} M_{i,j,k,l} \quad . \end{aligned} \tag{A.3}$$

For the scalar Minkowski functionals, the Crofton formulae read (see, e.g., Hadwiger 1957):

$$\int \mathrm{d}\mathcal{E}_i W_k(A \cap \mathcal{E}_i) = d_{dki} W_{i+k-d}(A) \tag{A.4}$$

for $d - k \geq i \geq 0$, where W_k denotes the i–dimensional Minkowski functional; the coefficients d_{dki} are given by

$$d_{dki} = a_{id} \frac{k! i! \omega_k \omega_i \omega_{2d-i-k}}{(k+i-d)! d! \omega_{d-k} \omega_{d-i} \omega_{k+i-d}} \tag{A.5}$$

with

$$a_{id} = \binom{d}{i} \frac{\omega_{d-1} ... \omega_{d-i}}{\omega_1 ... \omega_i} \quad \text{for} \quad i = 1, ..., d-1; \quad a_{0d} = 1, \quad a_{dd} = \frac{1}{\omega_d} \quad , \tag{A.6}$$

and ω_ν denoting the volume of the ν–dimensional unit ball. For $i < d - k$, the integral vanishes. A similar formula holds for the vectors, too (Hadwiger & Schneider 1971). Formulae of the Crofton type for tensors have not been investigated so far. To calculate the coefficients within these formulae, it is a convenient strategy to consider $A + \mathbf{t}$, where $\mathbf{t}$ is a translation, and to use the transformation rules for the tensors. This connects them with the coefficients $d_{d,k,i}$ arising in the original Crofton formulae. Here we list some of Crofton's formulae for the two–dimensional case:

Crofton formulae for second–rank tensors in 2 dimensions.

$$\begin{aligned} \int \mathrm{d}\mathcal{E}_1 W^2(A \cap \mathcal{E}_1) &= \pi W^2(A) \\ \int \mathrm{d}\mathcal{E}_1 W_{0,0,2,0}(A \cap \mathcal{E}_1) &= 2\pi W_{0,1,2,0}(A) \end{aligned} \tag{A.7}$$

A.1.2 A grid formalism

Now we discuss how one can develop a grid formalism for higher–order Minkowski valuations (see Schmalzing & Buchert 1997 for the scalar Minkowski functionals). It allows us to estimate the Minkowski valuations of excursion sets very effectively[1]

[1]The software was developed on the basis of programs by J. Schmalzing.

Combining Crofton's formulae and an estimator for the Euler characteristic (Adler 1981; Schmalzing & Buchert 1997), we get for the scalar Minkowski functionals

$$W_\nu(A) = \sum_{j=0}^{\nu} (-1)^j a^{d-\nu} \frac{\omega_d}{\omega_{d-\nu}} \frac{\nu!(d-\nu)!}{d!} \sum_{E^\nu \in \mathcal{L}_d^\nu} N_j(A \cap E^\nu) \quad , \tag{A.8}$$

where $N_j(A \cap E^\nu)$ is the number of j–dimensional lattice cells within $A \cap E^\nu$. The integration over all planes has been replaced by a summation over planes related to the lattice. Now there are two possibilities: Either we take hyperplanes from the dual or the real lattice. In each case one can perform the sum over the hyperplanes analytically by leading back the $N_j(A \cap E^\nu)$ to numbers of lattice cells etc. within A: $N_i(A)$.

In the first case, where we sum up over dual hyperplanes, $A \cap E^\nu$ in general does not consist of lattice cells of the original grid, but of shifted cells. However, we can perform the summation. An i–dimensional lattice cell I (of the original lattice) contains all points $\mathbf{x}$ which can be written as $\mathbf{x} = \mathbf{r}^I + \sum_{k=1}^{i} \alpha_k \mathbf{e}_k^I$, where $\mathbf{r}$ is an appropriately chosen lattice point, $\{\mathbf{e}_k^I\}_{k=1}^i$ is a collection of i different vectors spanning the lattice and $\alpha_k \in [0, a)$. On the other side, a dual ν–dimensional lattice plane E can be described as the set of points $\mathbf{y}$ for which $\mathbf{y} = \mathbf{r}^E + \sum_{k=1}^{\nu} \beta_k \mathbf{e}_k^E + 0.5 \sum_{k=1}^{d-\nu} \tilde{\mathbf{e}}_k^E$, where again $\mathbf{r}^E$ constitutes a lattice point, and the $\{\mathbf{e}_k^E, \tilde{\mathbf{e}}_k^E\}$ are a partition of the lattice vectors. The α_k^E run from $-\infty$ to ∞. To get an intersection of a lattice cell and a dual hyperplane, obviously, $(d-\nu)$ of the α_k^I have to be fixed at 0.5. This means, in particular, that intersections are only possible, if $i \geq d - \nu$. The dimension of the intersection is then $i - (d - \nu)$. That means, that j–dimensional intersections arise whenever a $(d - \nu + j)$–dimensional grid cell and a ν–dimensional hyperplane intersect. But how often does a given $(d - \nu + j)$–dimensional grid cell I generate a j–dimensional intersection, whenever it intersects with ν–dimensional hyperplanes? Well, as we saw, $(d - \nu)$ of the $i = (d - \nu + j)$ α_k^I have to be fixed at 0.5. We have $\binom{d-\nu+j}{d-\nu}$ possibilities to fix the α_k^I, thus, altogether, each $(d - \nu + j)$–dimensional grid cell I generates $\binom{d-\nu+j}{d-\nu} = \binom{d-\nu+j}{j}$ j–dimensional formations by intersections with ν–dimensional planes. Thus, we have as a result:

$$\sum_{E^\nu \in \mathcal{L}_d^\nu} N_j(A \cap E^\nu) = \binom{d-\nu+j}{j} N_{d-\nu+j}(A) \quad . \tag{A.9}$$

If we cut with real lattice planes, the counting argument is simpler and goes as follows: Each j–dimensional lattice cell of $A \cap E^\nu$ is also a j–dimensional cell within A. It occurs as an intersection only if $j \leq \nu$; for a fixed j–dimensional lattice cell I within A there are $\binom{d-j}{\nu-j}$ ν–dimensional planes intersecting with I. Thus, we have:

$$\sum_{E^\nu \in \mathcal{L}_d^\nu} N_j(A \cap E^\nu) = \binom{d-j}{\nu-j} N_j(A) \quad . \tag{A.10}$$

For the higher–order Minkowski valuations, we have to carry along the positions of the cells arising within Crofton's formula. Thus, instead of the pure numbers of cells, we have to insert the sums of their positions. The precise weighting scheme is always based on an estimator of the Euler characteristic and the corresponding higher–order valuations for lower–dimensional lattice cells within $A \cap E_\nu$. In the case of the dual lattice planes, one can show that the centers of the j–dimensional cells, $\mathbf{x}_a^{(j)}$, equal the centers of the $(d-j+\nu)$–dimensional cells within A, $\mathbf{x}_a^{(d-j+\nu)}$, which generate the former cells by intersection with a ν–dimensional hyperplane, are the same. For the case of the real planes, obviously, we have to replace the $N_j(A)$ by the sum over the centers of all j–dimensional cells. Therefore, the relevant formulae are:

$$\sum_{E^\nu \in \mathcal{L}_d^\nu} \sum_{a=1}^{N_j} \mathbf{x}_a^{(j)}(A \cap E^\nu) = \binom{d-\nu+j}{j} \sum_{a=1}^{N_{d-\nu+j}} \mathbf{x}_a^{(d-\nu+j)}(A) \quad . \tag{A.11}$$

and

$$\sum_{E^\nu \in \mathcal{L}_d^\nu} \sum_{a=1}^{N_j} \mathbf{x}_a^{(j)}(A \cap E^\nu) = \binom{d-j}{\nu-j} \sum_{a=1}^{N_j} \mathbf{x}_a^{(j)}(A) \quad . \tag{A.12}$$

For tensors one has to be more cautious. It turns out, that there is no appropriate estimator for the tensor $\int \mathrm{d}S \kappa \mathbf{x}\mathbf{x}$ for two–dimensional patterns. For bonds part of $A \cap E^1$ the correct weighting is $\frac{1}{2}(\mathbf{x}_1\mathbf{x}_1 + \mathbf{x}_2\mathbf{x}_2)$, where $\mathbf{x}_1$ and $\mathbf{x}_2$ mark the endpoints of the bond. Points part of $A \cap E^0$ are weighted by their squared position, of course. Note, that this reasoning refers to cells within $A \cap E_\nu$, to link it back to cells within A one has to average over all possible E_ν which hit a fixed cell of A.

A.2 Computational details for the Minkowski functionals

Here, we summarize some details on how to compute the Minkowski functionals. We focus on patterns arising when the Boolean grain method is applied to point sets, and on cellular complexes in two dimensions[2].

Two dimensions The basic elements which allow us to compute the tensors both for a Boolean grain model and for a cellular complex are straight lines, part of circles and corners. In the following these elements are thought of to be part of a convex body K and treated separately. We have $\Theta_1(\mathcal{B}) = \frac{\mathrm{d}}{\mathrm{d}\epsilon}\mu(\mathrm{nor}_K(\mathcal{B},\epsilon)) \mid_{\epsilon=0}$ and $\Theta_0(\mathcal{B}) = \frac{\mathrm{d}^2}{\mathrm{d}\epsilon^2}\mu(\mathrm{nor}_K(\mathcal{B},\epsilon)) \mid_{\epsilon=0}$. As Borel sets $\mathcal{B}$, we consider sets of the form $\mathrm{d}S \times \omega$, where $\mathrm{d}S$ is part of the surface part of K under consideration and $\mathrm{d}\omega \subset \mathcal{S}^1$.

[2]The software for the Boolean grain method was developed on the basis of programs by J. Schmalzing and M. Kerscher.

1. Consider a straight part of a surface ∂K linking $\mathbf{x}$ and $\mathbf{y}$. Let l be $l = |\mathbf{y} - \mathbf{x}|$ and $\mathbf{n}$ the normal of ∂K pointing towards ω_0. Then $\mu(\mathrm{nor}_K(\mathcal{B}, \epsilon)) = \epsilon \mathrm{d}l$, if $(\mathbf{x}, \omega_0) \in \mathcal{B}$, and using Equation (1.3.20) we get:

$$\Theta_1 = \mathrm{d}l\mathrm{d}\omega\delta(\omega - \omega_0) \quad , \tag{A.13a}$$
$$\Theta_0 = 0 \quad . \tag{A.13b}$$

   Thus, we get for a straight line part of ∂K connecting $\mathbf{x}$ and $\mathbf{y}$ (see the sketch in Figure A.1) the contributions listed in Table A.1.

2. Now we are interested in a piece of a circle of radius R centered on $\mathbf{x}$, linking two points $\mathbf{x}_1$ and $\mathbf{x}_2$. It is convenient to introduce a local coordinate system with polar coordinates centered at $\mathbf{x}$ with the local basis vectors $\mathbf{e}_r$ and $\mathbf{e}_\varphi$. $\mathbf{x}_1$ and $\mathbf{x}_2$ can then be written as $\mathbf{x}+R\mathbf{e}_r(1)$ and $\mathbf{x}+R\mathbf{e}_r(2)$, respectively; the local normals coincide with $\mathbf{e}_r$ in this coordinate system. We need furthermore the $\mathbf{e}_\varphi$ (see Figure A.1) and the opening angle $\Delta\varphi$. We parameterize the surface by the angle φ, for a small piece of the surface we get

$$\mu(\mathrm{nor}_K(\mathcal{B}, \epsilon)) = \frac{1}{2}(R + \epsilon)^2 \int_{P_2(\mathcal{B})} \mathrm{d}\omega \mathbb{1}_{\mathrm{d}\varphi}(\omega) \quad , \tag{A.14}$$

   where again $P_2(\mathcal{B})$ is the projection of $\mathcal{B}$ onto $\mathcal{S}^1$. Therefore, we get for the generalized curvature measures:

$$\Theta_1 = R\mathrm{d}\varphi\mathrm{d}\omega\delta(\omega - \varphi) \quad , \tag{A.15a}$$
$$\Theta_0 = \mathrm{d}\varphi\mathrm{d}\omega\delta(\omega - \varphi) \quad . \tag{A.15b}$$

   If we integrate these contributions over the relevant part of the circle, we get the terms listed in Table A.2.

3. Now we consider a corner of a convex body. Let $\mathbf{x}$ denote the position vector of the corner, $\mathbf{e}_r(1)$ and $\mathbf{e}_r(2)$ the normal vectors of the adjacent surfaces. Again, it is convenient to introduce polar coordinates centered at the corner. The generalized normal bundle is the sector of a circle; when we look at an infinitesimal piece of the surface $\mathrm{d}\varphi$, we get

$$\mu(\mathrm{nor}_K(\mathcal{B}, \epsilon)) = \frac{1}{2}\epsilon^2 \int_{P_2(\mathcal{B})} \mathrm{d}\omega \mathbb{1}_{\mathrm{d}\varphi}(\omega) \tag{A.16}$$

   The application of the differential operators yields that

$$\Theta_1 = 0 \quad , \tag{A.17a}$$
$$\Theta_0 = \mathrm{d}\mathbf{r}\delta(\mathbf{x} - \mathbf{r})\mathrm{d}\omega\theta(\varphi_2 - \omega)\theta(\omega - \varphi_1) \quad . \tag{A.17b}$$

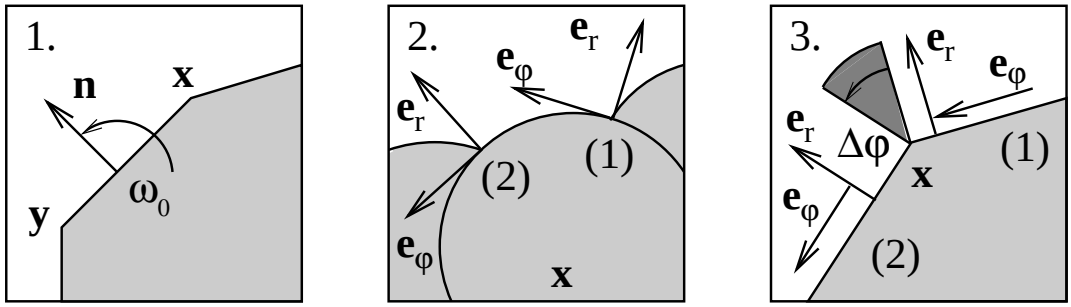

Figure A.1: Here we show the 2d–geometry of straight lines, circles and corners $\subset \partial K$ and introduce the notations used in Tables A.1, A.2 and A.3. $\Delta\varphi$ is always the angle between the normals $\mathbf{e}_r(1)$ and $\mathbf{e}_r(2)$.

Here, θ denotes the step function[3]. The contributions of a whole corner are specified in Table A.3.

These formulae apply to parts of a body where its surface is convex. For intersections, one has to subtract contributions from the intersection point. Only intersection points at the surface of the pattern contribute (Mecke 1994). For an estimate of the Minkowski valuations in two dimensions, only intersections of two bodies are taken into account.

[3]The step function is defined as

$$\theta(x) \equiv \begin{cases} 0 & \text{if } x < 0, \\ 1 & \text{if } x \geq 0 \end{cases} . \tag{A.18}$$

1.	straight line
$M_{0,1,0,0}$	$\lvert\mathbf{x}-\mathbf{y}\rvert$
$M_{0,1,1,0}$	$\lvert\mathbf{x}-\mathbf{y}\rvert\frac{1}{2}(\mathbf{x}+\mathbf{y})$
$M_{0,1,2,0}$	$\lvert\mathbf{x}-\mathbf{y}\rvert\frac{1}{3}(\mathbf{xx}+\mathbf{yy}+\mathbf{xy})$
$M_{0,1,1,1}$	$\lvert\mathbf{x}-\mathbf{y}\rvert\frac{1}{2}(\mathbf{n}(\mathbf{x}+\mathbf{y}))$
$M_{0,1,0,2}$	$\lvert\mathbf{x}-\mathbf{y}\rvert\mathbf{nn}$
$M_{0,0,k,l}$	0

Table A.1: Contributions to the Quermaß tensors from a straight line. The notations are explained in Figure A.1.

2.	part of a circle
$M_{0,1,0,0}$	$\Delta\varphi R$
$M_{0,1,1,0}$	$\mathbf{x}R\Delta\varphi + R^2(\mathbf{e}_\varphi(1)-\mathbf{e}_\varphi(2))$
$M_{0,1,2,0}$	$R\Delta\varphi\mathbf{xx} + 2R^2\mathbf{x}(\mathbf{e}_\varphi(1)-\mathbf{e}_\varphi(2)) + R^3\frac{1}{2}(\mathbf{e}_\varphi(1)\mathbf{e}_r(1)-\mathbf{e}_\varphi(2)\mathbf{e}_r(2)+\Delta\varphi E_2)$
$M_{0,1,1,1}$	$R\mathbf{x}(\mathbf{e}_\varphi(1)-\mathbf{e}_\varphi(2)) + \frac{1}{2}R^2(\mathbf{e}_\varphi(1)\mathbf{e}_r(1)-\mathbf{e}_\varphi(2)\mathbf{e}_r(2)+\Delta\varphi E_2)$
$M_{0,1,0,2}$	$\frac{R}{2}(\mathbf{e}_r(1)\mathbf{e}_\varphi(1)-\mathbf{e}_\varphi(2)\mathbf{e}_r(2)+\Delta\varphi E_2)$
$M_{0,0,k,l}$	$\frac{1}{R}M_{0,0,i,j}$

Table A.2: Contributions to the Quermaß tensors. The notations are explained in Figure A.1.

3.	corner
$M_{0,1,i,j}$	0
$M_{0,0,0,0}$	$\Delta\varphi$
$M_{0,0,1,0}$	$\Delta\varphi\mathbf{x}$
$M_{0,0,2,0}$	$\Delta\varphi\mathbf{xx}$
$M_{0,0,1,1}$	$\mathbf{x}(\mathbf{e}_\varphi(1)-\mathbf{e}_\varphi(2))$
$M_{0,0,0,2}$	$\frac{1}{2}(\mathbf{e}_\varphi(1)\mathbf{e}_r(1)-\mathbf{e}_\varphi(2)\mathbf{e}_r(2)+\Delta\varphi E_2)$

Table A.3: Contributions of a corner to the Quermaß tensors. The notations are explained in Figure A.1.

References

Abdelsalam, H. M., Saha, P., & Williams, L. L. R., Mon. Not. R. Astron. Soc. **294** (1998), 734.

Abell, G. O., Ap. J. Suppl. **3** (1958), 211.

Adami, C., Biviano, A., & Mazure, A., Astron. Astrophys. **331** (1998), 439.

Adami, C., Mazure, A., Biviano, A., Katgert, P., & Rhee, G., Astron. Astrophys. **331** (1998), 493.

Adler, R. J., *The geometry of random fields*, John Wiley & Sons, Chichester, 1981.

Alesker, S., Ann. of Math. **149 (3)** (1999), 977.

Alesker, S., Geom. Dedicata **74** (1999), 241.

Alexandrov, A. D., Matem. Sb. SSSR **2** (1937), 1205–1238, in Russian, summary in German.

Alimi, J.-M., Valls-Gabaud, D., & Blanchard, A., Astron. Astrophys. **206** (1988), L11.

Andreon, S., Astron. Astrophys. **284** (1994), 801.

Andreon, S., Astron. Astrophys. **314** (1996), 763.

Annis, J., in: *American Astronomical Society Meeting*, Vol. 185, December 1994, p. 7405.

Ashman, K. M., Bird, C. M., & Zepf, S. E., A. J. **108** (1994), 2348.

Bahcall, N. A., astro-ph 9611148, 1996.

Balian, R. & Schaeffer, R., Astron. Astrophys. **220** (1989), 1.

Bardeen, J. M., Bond, J. R., Kaiser, N., & Szalay, A. S., Ap. J. **304** (1986), 15–61.

Bartelmann, M. & Schneider, P., Physics Reports (1999), submitted, astro-ph/9912508.

Bartelmann, M., Ehlers, J., & Schneider, P., Astron. Astrophys. **280** (1993), 351.

Bartelmann, M., Huss, A., Colberg, J. M., Jenkins, A., & Pearce, F. R., Astron. Astrophys. **330** (1998), 1–9.

Bartelmann, M., in: *Evolution of Large-Scale Structure: From Recombination to Garching*, 1998, p. 213.

Beisbart, C. & Kerscher, M., ApJ accepted.

Beisbart, C., Buchert, T., & Wagner, H., Physica A in press.

Beisbart, C., Diplomarbeit, Ludwig–Maximilians–Universität München, 1997, in German.

Belloni, P. & Röser, H.-J., Ap. J. Suppl. **118** (1996), 65.

Bender, R., Burstein, D., & Faber, S., Ap. J. **399** (1992), 462.

Benoist, C., Maurogordato, S., da Costa, L. N., Cappi, A., & Schaeffer, R., Ap. J. **472** (1996), 452.

Benoist, C., Cappi, A., da Costa, L. N., Maurogordato, S., Bouchet, F. R., & Schaeffer, R., Ap. J. **514** (1999), 563.

Binggeli, B., Tarenghi, M., & Sandage, A., Astron. Astrophys. **228** (1990), 42.

Boggs, P. T., Byrd, R. H., & Schnabel, R. B., SIAM J.Sci. Stat. Comput. **8 (6)** (1987), 1052.

Boggs, P. T., Byrd, R. H., Donaldson, J. R., & Schnabel, R. B., ACM Trans. Math. Sortware **15 (4)** (1989), 348.

Böhringer, H., Voges, W., Huchra, J. P., McLean, B., Giacconi, R., Rosati, P., Burg, R., Mader, J., Schuecker, P., Simic, D., Komossa, S., Reiprich, T. H., Retzlaff, J., & Trümper, J., Ap. J. Suppl. **129** (2000), 435.

Börner, G., Mo, H., & Zhou, Y., Astron. Astrophys. **221** (1989), 191–196.

Buchert, T. & Ehlers, J., Astron. Astrophys. **320** (1997), 1–7.

Buote, D. A. & Tsai, J. C., Ap. J. **452** (1995), 522–537.

Buote, D. A. & Tsai, J. C., Ap. J. **458** (1996), 27.

Caon, N. & Einasto, M., Mon. Not. R. Astron. Soc. **273** (1995), 913.

Capelato, H. V., Gerbal, D., Salvador-Sole, E., Mathez, G., Mazure, A., & Sol, H., Ap. J. **241** (1980), 521.

Cen, R., Ap. J. **485** (1997), 39.

Chandrasekhar, S. & Lee, E. P., Mon. Not. R. Astron. Soc. **139** (1968), 135.

Coles, P. & Lucchin, F., *Cosmology: The origin and evolution of cosmic structure*, John Wiley & Sons, Chichester, 1994.

Couchman, H. M. P., Thomas, P. A., & Pearce, F. R., Ap. J. **452** (1995), 797.

Cressie, N., *Statistics for spatial data*, John Wiley & Sons, Chichester, 1991.

da Costa, L. N., Willmer, C. N. A., Pellegrini, P. S., Chaves, O. L., Rité, C., Maia, M. A. G., Geller, M. J., Latham, D. W., Kurtz, M. J., Huchra, J. P., Ramella, M., Fairall, A. P., Smith, C., & Lípari, S., A. J. **116** (1998), 1.

Daley, D. J. & Vere-Jones, D., *An introduction to the theory of point processes*, Springer Verlag, Berlin, 1988.

Davis, M., Meiksin, A., Strauss, M. A., da Costa, L. N., & Yahil, A., Ap. J. **333** (1988), L9.

Diaferio, A., Kauffmann, G., Colberg, J. r. ., & White, S. D. M., Mon. Not. R. Astron. Soc. **307** (1999), 537.

Domínguez-Tenreiro, R. & Martínez, V. J., Ap. J. **339** (1989), L9–L11.

Domínguez-Tenreiro, R., Campos, A., Gomez-Flechoso, M. A., & Yepes, G., Ap. J. **424** (1994), L73.

Dressler, A. & Shectman, S. A., A. J. **95** (1988), 985.

Dressler, A., Ap. J. **236** (1980), 351–365.

Einasto, M., Mon. Not. R. Astron. Soc. **250** (1991), 802.

Einasto, M., Mon. Not. R. Astron. Soc. **252** (1991), 261.

Ellis, J., Phys. Skripta **T 85** (2000), 221.

Evrard, A. E., Mohr, J. J., Fabricant, D. G., & Geller, M. J., Ap. J. Lett. **419** (1993), 9.

Fenchel, D., C.R. Acad. Sci. Paris **203** (1936), 647, in French.

Fitchett, M., Mon. Not. R. Astron. Soc. **230** (1988), 161.

Fritsch, C. & Buchert, T., Astron. Astrophys. **344** (1999), 749.

Fritsch, C., Ph.D. thesis, Ludwig–Maximilians–Universität München, 1996.

Fujita, Y. & Takahara, F., Ap. J. **519** (1999), L51.

Gaite, J. ., Domínguez, A., & Pérez-Mercader, J., Ap. J. **522** (1999), L5.

Gambera, M., Pagliaro, A., Antonuccio-Delogu, V., & Becciani, U., Ap. J. **488** (1997),

136.
Gardini, A., Bonometto, S. A., & Maccio, A., New Astronomy **4** (1999), 557.
Giovanelli, R., Haynes, M. P., & Chincarini, G. L., Ap. J. **300** (1986), 77.
Giuricin, G., Mardirossian, F., Mezzetti, M., Pisani, A., & Ramella, M., Astron. Astrophys. **192** (1988), 95.
Goenner, H., *Einführung in die Kosmologie*, Spektrum Akademischer Verlag, Heidelberg, 1994.
Götz, M., Huchra, J. P., & Brandenberger, R. H., ApJ submitted, astro–ph/9811393, 1998.
Grebenev, S. A., Forman, W., Jones, C., & Murray, S., Ap. J. **445** (1995), 607.
Groemer, H., Pacific J. Math. **75** (1978), 397.
Hadwiger, H. & Meier, C., Math. Nachr. **56** (1974), 361.
Hadwiger, H. & Schneider, R., Elemente der Mathematik **26** (1971), 49.
Hadwiger, H., *Vorlesungen über Inhalt, Oberfläche und Isoperimetrie*, Springer Verlag, Berlin, 1957.
Hamilton, A. J. S., Ap. J. **331** (1988), L59.
Heavens, A. F. & Sheth, R. K., Mon. Not. R. Astron. Soc. **310** (1999), 1062.
Henriksen, M. J. & Merrill, W. E., in: *American Astronomical Society Meeting*, Vol. 183, December 1993, p. 5304.
Hermit, S., Santiago, B. X., Lahav, O., Strauss, M. A., Davis, M., Dressler, A., & Huchra, J. P., Mon. Not. R. Astron. Soc. **283** (1996), 709.
Hernquist, L. & Katz, N., Ap. J. Suppl. **70** (1989), 419.
Irwin, J. A. & Bregman, J. N., Ap. J. **538** (2000), 543.
Irwin, J. A., Bregman, J. N., & Evrard, A. E., Ap. J. **519** (1999), 518.
Isham, V., in: *Spatial Processes and Spatial Time Series Analysis* (Bruxelles) (Droesbeke, F., ed.), Publications des Facultés universitaires Sain-Louis, 1985, p. 63.
Kauffmann, G., Colberg, J. M., Diaferio, A., & White, S. D. M., Mon. Not. R. Astron. Soc. **303** (1999), 188–206.
Kendall, M. G., Biometrica **30** (1938), 81.
Kerscher, M., Schmalzing, J., Buchert, T., & Wagner, H., Astron. Astrophys. **333** (1998), 1–12.
Kerscher, M., Buchert, T., & Futamase, T., ApJL submitted, astro–ph/0007284, 2000.
Kerscher, M., Ph.D. thesis, Ludwig–Maximilians–Universität München, 1998.
Kerscher, M., Astron. Astrophys. **343** (1999), 333.
Lee, K. L., J. Am. Statist. Ass. **74** (1979), No. 367, 708.
Magtesyan, A. P. & Movsesyan, V. G., Astronomy Letters **21** (1995), 429.
Marzke, R., Geller, M., da Costa, L., & Huchra, J., A. J. **110** (1995), 477.
Maurogordato, S. & Lachièze–Rey, M., Ap. J. **320** (1987), 13.
McMillian, S. L. W., Kowalski, M. P., & Ulmer, M. P., Ap. J. Suppl. **70** (1989), 723.
McMullen, P., Rend. Circ. Mat. Palermo (2) **50** (1997), 259–271.
Mecke, K. & Wagner, H., J. Stat. Phys. **64** (1991), 843.
Mecke, K., *Integralgeometrie in der Statistischen Physik: Perkolation, komplexe Flüssigkeiten und die Struktur des Universums*, Harri Deutsch, Thun, Frankfurt/Main, 1994.
Minkowski, H., Mathematische Annalen **57** (1903), 447.

Mo, H. J., Einasto, M., Xia, X. Y., & Deng, Z. G., Mon. Not. R. Astron. Soc. **255** (1992), 382.
Mohr, J. J., Fabricant, D. G., & Geller, M. J., Ap. J. **413** (1993), 492.
Mohr, J. J., Evrard, A. E., Fabricant, D. G., & Geller, M. J., Ap. J. **447** (1995), 8.
Mohr, J. J., Evrard, A. E., Fabricant, D. E., & Geller, M. J., Ap. J. **447** (1995), 8.
Müller, H. R., Rend. Circ. Mat. Palermo (2) **2** (1953), 1.
Navarro, J. F., Frenk, C. S., & White, S. D. M., Mon. Not. R. Astron. Soc. **275** (1995), 720–740.
Park, C., Vogeley, M. S., Geller, M. J., & Huchra, J. P., Ap. J. **431** (1994), 569–585.
Pearce, F. R. & Couchman, H. M. P., New Astronomy **2/5** (1997), 411.
Peebles, P. J. E., *The large scale structure of the Universe*, Princeton University Press, Princeton, New Jersey, 1980.
Peebles, P. J. E., *Principles of physical cosmology*, Princeton University Press, Princeton, New Jersey, 1993.
Perlmutter, S., Aldering, G., Goldhaber, G., Knop, R. A., Nugent, P., Castro, P. G., Deustua, S., Fabbro, S., Goobar, A., Groom, D. E., Hook, I. M., Kim, A. G., Kim, M. Y., Lee, J. C., Nunes, N. J., Pain, R., Pennypacker, C. R., Quimby, R., Lidman, C., Ellis, R. S., Irwin, M., McMahon, R. G., Ruiz-Lapuente, P., Walton, N., Schaefer, B., Boyle, B. J., Filippenko, A. V., Matheson, T., Fruchter, A. S., Panagia, N., Newberg, H. J. M., Couch, W. J., & The Supernova Cosmology Project, , Ap. J. **517** (1999), 565.
Pinkney, J., Roettiger, K., Burns, J. O., & Bird, C., Ap. J. Suppl. **104** (1996), 1.
Postman, M. & Geller, M. J., Ap. J. **281** (1984), 95.
Postman, M., in: *Evolution of Large-Scale Structure: From Recombination to Garching*, 1998, p. 270.
Press, W. H., Flannery, B. P., Teukolsky, S. A., & Vetterling, W. T., *Numerical recipes in C*, Cambridge University Press, Cambridge, 1987.
Reiprich, T., Diplomarbeit, Ludwig–Maximilians–Universität München, 1998.
Rhee, G. F. R. N. & Latour, H. J., Astron. Astrophys. **243** (1991), 38.
Richstone, D., Loeb, A., & Turner, E. L., Ap. J. **393** (1992), 477.
Sahni, V., Sathyaprakash, B. S., & Shandarin, S. F., Ap. J. Lett. **459** (1998), 5.
Santiago, B. X. & Strauss, M. A., Ap. J. **387** (1992), 9–20.
Sarazin, C. W., Rev. Mod. Phys. **58** (1986), 1.
Schaeffer, R., Maurogordato, S., Cappi, A., & Bernardeau, F., Mon. Not. R. Astron. Soc. **263** (1993), L21.
Schindler, S., Astron. Astrophys. **349** (1999), 435.
Schmalzing, J. & Buchert, T., Ap. J. Lett. **482** (1997), L1.
Schmalzing, J., Buchert, T., Melott, A. L., Sahni, V., Sathyaprakash, B. S., & Shandarin, S. F., Ap. J. **526** (1999), 568.
Schmalzing, J., Gottlöber, S., Klypin, A. A., & Kravtsov, A. V., Mon. Not. R. Astron. Soc. **309** (1999), 1007.
Schmalzing, J., Diplomarbeit, Ludwig–Maximilians–Universität München, 1996, in German, English excerpts available.
Schneider, P., King, L., & Erben, T., Astron. Astrophys. **353** (2000), 41.
Schneider, R., Israel J. Math. **9** (1971), 241.

Schneider, R., Abh. Math. Sem. Univ. Hamburg **37** (1972), 112.
Schneider, R., Abh. Math. Sem. Univ. Hamburg **37** (1972), 202.
Schneider, R., *Convex bodies: the Brunn–Minkowski theory*, Cambridge University Press, Cambridge, 1993.
Schneider, R., Mathematical preprint Freiburg, 22/99, 1999.
Slezak, E., Durret, F., & Gerbal, D., Mon. Not. R. Astron. Soc. **108** (1994), 1996.
Stoyan, D. & Stoyan, H., *Fractals, random shapes and point fields*, John Wiley & Sons, Chichester, 1994.
Stoyan, D., Math. Nachr. **116** (1984), 197.
Sylos Labini, F., Montuori, M., & Pietronero, L., Physics Rep. **293** (1998), 61.
Szapudi, I., Branchini, E., Frank, C., Maddox, S., & Saunders, W., MNRAS accepted, 2000.
Tsai, J. C. & Buote, D. A., Mon. Not. R. Astron. Soc. **282** (1996), 77–93.
Tully, R. B., A. J. **96** (1988), 73.
Valdarnini, R., Ghizzardi, S., & Bonometto, S., New Astronomy **4** (1999), 71.
van Lieshout, M. N. M. & Baddeley, A. J., Statistica Neerlandica **50** (1996), 344–361.
van Lieshout, M. N. M. & Baddeley, A. J., Scandinavian Journal of Statistics **26** (2000), 511.
Wälder, O. & Stoyan, D., Biom. J. **38** (1996), 895.
Wälder, O. & Stoyan, D., Statistics **29** (1997), 179.
White, S. D. M., Tully, R. B., & Davis, M., Ap. J. **333** (1988), L45.
White, S. D. M., Efstathiou, G., & Frenk, C. S., Mon. Not. R. Astron. Soc. **262** (1993), 1023–1028.
White, S. D. M., Mon. Not. R. Astron. Soc. **186** (1979), 145.
Wolf, M., Astron. Nachr. **170** (1906), 211.
Zel'dovich, Y. B., Astron. Astrophys. **5** (1970), 84.
Zwicky, F., Helvetica Physica Acta **6** (1933), 110.

Danksagung

An erster Stelle möchte ich meinem Betreuer Priv.–Doz. Dr. Thomas Buchert danken. In der Diskussion mit ihm sind viele neue Ideen entstanden, und er hat sich immer sehr persönlich um den Fortgang meiner Arbeit gekümmert. Herzlich danken möchte ich auch Prof. Dr. Herbert Wagner. Seine Anregungen haben mich stimuliert, und ich habe mit ihm immer gerne zusammengearbeitet.
Weiterhin gilt mein Dank allen anderen Mitgliedern der Kosmologie–Arbeitsgruppe hier im Hause, das sind Dr. Martin Kerscher, Dr. Jens Schmalzing, Dr. Alvaro Domínguez, Robert Dahlke und Christian Sicka. Vor allem Martin Kerscher und Jens Schmalzing haben viele Anregungen zu meiner Arbeit beigesteuert, ich habe von ihren Computer–Codes profitiert, und sie haben mir viele gute Tips gegeben.
Allen, die hier mit der Systemadministration beauftragt waren, nämlich Hans Aschauer, Ullrich Martini, Dr. Jens Schmalzing und Dr. Sigmund Stintzing danke ich für ihre Hilfestellungen.
Teile der Arbeit beruhen auf internationalen Kooperationen. Deshalb danke ich Priv.–Doz. Dr. Matthias Bartelmann, Dr. Jörg Colberg, Dr. Antonaldo Diaferio und Dr. Riccardo Valdarnini für die gute Zusammenarbeit: insbesondere molto grazie nach Italien.
Meine Arbeit wurde im Rahmen des SFB 375 "Astroteilchenphysik" der Deutschen Forschungsgemeinschaft gefördert. Die SFB–Tagungen in Ringberg haben mich stets motiviert. Insbesondere von den Mitgliedern der Universitäts–Sternwarte kamen dabei interessante Anregungen. Stellvertretend nenne ich Prof. Dr. Ralf Bender, der freundlicherweise auch das Zweitgutachten meiner Dissertation übernimmt.
Für Anregungen und Korrekturen zum Manuskript bin ich Dr. Jens Schmalzing, Dr. Martin Kerscher und vor allem Dr. Alvaro Domínguez und Robert Dahlke sehr dankbar.
Susanne Adler–Aschauer, mit der ich lange das Zimmer teilte, danke ich für die guten Gespräche über Physik und Nicht–Physik.
Allen Lehrstuhlangehörigen am Lehrstuhl Wagner danke ich für die gute Atmosphäre, die hoffentlich bald wieder durch den geplanten "Theoretiker–Sozialraum" in fröhlichen Teerunden Ausdruck findet.
Allen, welche mich während meiner Promotion unterstützt haben, bin ich dankbar verbunden. Beispielhaft seien hier nur meine Eltern erwähnt.